Springer Theses
Recognizing Outstanding Ph.D. Research

Shuang Zhou

Lyotropic Chromonic Liquid Crystals

From Viscoelastic Properties to Living Liquid Crystals

Springer

Springer Theses

Recognizing Outstanding Ph.D. Research

Aims and Scope

The series "Springer Theses" brings together a selection of the very best Ph.D. theses from around the world and across the physical sciences. Nominated and endorsed by two recognized specialists, each published volume has been selected for its scientific excellence and the high impact of its contents for the pertinent field of research. For greater accessibility to non-specialists, the published versions include an extended introduction, as well as a foreword by the student's supervisor explaining the special relevance of the work for the field. As a whole, the series will provide a valuable resource both for newcomers to the research fields described, and for other scientists seeking detailed background information on special questions. Finally, it provides an accredited documentation of the valuable contributions made by today's younger generation of scientists.

Theses are accepted into the series by invited nomination only and must fulfill all of the following criteria

- They must be written in good English.
- The topic should fall within the confines of Chemistry, Physics, Earth Sciences, Engineering and related interdisciplinary fields such as Materials, Nanoscience, Chemical Engineering, Complex Systems and Biophysics.
- The work reported in the thesis must represent a significant scientific advance.
- If the thesis includes previously published material, permission to reproduce this must be gained from the respective copyright holder.
- They must have been examined and passed during the 12 months prior to nomination.
- Each thesis should include a foreword by the supervisor outlining the significance of its content.
- The theses should have a clearly defined structure including an introduction accessible to scientists not expert in that particular field.

More information about this series at http://www.springer.com/series/8790

Shuang Zhou

Lyotropic Chromonic Liquid Crystals

From Viscoelastic Properties to Living Liquid Crystals

Doctoral Thesis accepted by
Kent State University, Kent, OH, USA

Springer

Author
Dr. Shuang Zhou
Chemical Physics Interdisciplinary Program,
Liquid Crystal Institute
Kent State University
Kent, OH
USA

Supervisor
Prof. Oleg D. Lavrentovich
Chemical Physics Interdisciplinary Program,
Liquid Crystal Institute
Kent State University
Kent, OH
USA

ISSN 2190-5053 ISSN 2190-5061 (electronic)
Springer Theses
ISBN 978-3-319-52805-2 ISBN 978-3-319-52806-9 (eBook)
DOI 10.1007/978-3-319-52806-9

Library of Congress Control Number: 2016963643

© Springer International Publishing AG 2017
This work is subject to copyright. All rights are reserved by the Publisher, whether the whole or part of the material is concerned, specifically the rights of translation, reprinting, reuse of illustrations, recitation, broadcasting, reproduction on microfilms or in any other physical way, and transmission or information storage and retrieval, electronic adaptation, computer software, or by similar or dissimilar methodology now known or hereafter developed.
The use of general descriptive names, registered names, trademarks, service marks, etc. in this publication does not imply, even in the absence of a specific statement, that such names are exempt from the relevant protective laws and regulations and therefore free for general use.
The publisher, the authors and the editors are safe to assume that the advice and information in this book are believed to be true and accurate at the date of publication. Neither the publisher nor the authors or the editors give a warranty, express or implied, with respect to the material contained herein or for any errors or omissions that may have been made. The publisher remains neutral with regard to jurisdictional claims in published maps and institutional affiliations.

Printed on acid-free paper

This Springer imprint is published by Springer Nature
The registered company is Springer International Publishing AG
The registered company address is: Gewerbestrasse 11, 6330 Cham, Switzerland

To my parents.
献给我的父母

Supervisor's Foreword

Liquid crystals (LCs) are anisotropic fluids with a long-range orientational order and a partial or complete loss of positional order. The most known are the so-called thermotropic LCs formed by rod-shaped low molecular weight organic molecules. These materials show the LC state in a certain temperature range, between the melting point of a crystal and the so-called clearing point of a transition into the isotropic liquid. Thermotropic LCs made a revolution in the way we present information nowadays, enabling the modern industry of informational displays. There is another important class of LCs, called lyotropic LCs, with potentially even broader uses as responsive soft matters. Lyotropics are formed by dissolving organic molecules in a solvent, typically water. If the molecules are amphiphilic, they are arranged in micelles or bilayers, the shape of which depends on the concentration but little on the temperature. There is a distinct subgroup of lyotropics, the so-called chromonic lyotropic liquid crystals (LCLCs), that embraces many dyes and drugs, proteins, and even nucleotides. Chromonic molecules are typically plank-like with a polyaromatic rigid flat core and polar groups at the periphery. When in water, the molecules are attracted face to face to each other and self-assembled into elongated open-end aggregates. Dissociation of polar peripheral groups leads to the formation of electric double layers around the aggregates. The structure of chromonic aggregates is strikingly similar to the assemblies of nucleic pair bases in double-stranded DNA. The association energy of two neighboring molecules within an aggregate is small, about (5–15) k_BT. As a result, the aggregate's length changes strongly with temperature, concentration, ionic content of the solution, presence of additives, etc. At sufficiently higher concentrations, these aggregates align parallel to each other, forming a LC. However, the chromonic version of a LC is very different from all other types of LCs since the building units are polydisperse aggregates with a length that is very sensitive to both the temperature and the concentration. As a result, both these parameters control the liquid crystalline behavior of chromonics; this dual character of LCLCs is sometimes expressed by an abbreviation $(LC)^2$.

The weak non-covalent self-assembly of chromonics resembles super-molecular assemblies in biological systems. The first fundamental question explored by Shuang Zhou was how the weak forces responsible for the self-assembly of aggregates shape up viscoelastic properties of the LC. Because of the long-range orientational order, LCs are elastic media, with a resistance to spatial changes in the direction of orientation. Furthermore, their viscous response to shear is anisotropic, i.e., it depends on the orientation and the direction of shear. Shuang was the first researcher to present a detailed picture of viscoelasticity of LCLCs. He measured elastic moduli of splay, bend, and twist, as well as the corresponding viscosities using two different techniques: a magnetic field realignment and dynamic light scattering. The latter was performed in collaboration with Dr. Samuel Sprunt and his group at the Department of Physics, Kent State University. The viscoelastic parameters turned out to be strikingly different from those in regular LCs. In particular the twist elastic constant was 10 times smaller than the bend and splay elastic constants, while the splay and bend moduli varied strongly with the temperature and concentration. Among the three viscosity coefficients, the bend viscosity was four orders of magnitude smaller than the twist and splay viscosities. Shuang explained all these features by the changes in contour and persistence lengths of the chromonic aggregates, caused by temperature, concentration, and the presence of ionic additives. In particular the splay elastic constant was determined mostly by the contour length of aggregates, while the bend constant depended primarily on their persistence length.

Although chromonic molecules are water soluble, their structure is different from regular amphiphiles such as soap and detergents. In particular the chromonic molecules are deprived of flexible hydrocarbon chains. This difference makes the chromonics non-toxic and allows one to interface them with biological matter. Shuang took advantage of this feature, by introducing a new experimental example of active matter, the so-called "living liquid crystal", representing a dispersion of motile rod-like bacteria in an LCLC. The unique advantage of the living liquid crystals, explored in collaboration with Drs. Igor Aranson and Andrei Sokolov at Argonne National Lab, is that the two defining features, namely bacterial activity and orientational order, can be tuned independently of each other. Activity is controlled by the amount of oxygen/nitrogen available to the bacteria, and the orientational order is controlled by the temperature and concentration of the chromonic component. Shuang demonstrated that the bacterial behavior and orientational order are influencing each other in non-trivial ways. At low activity levels, the LCLC controls trajectories of the bacteria, forcing them to swim along the direction of LC alignment. Birefringent nature of LCLCs allows one to see under a regular optical microscope the wave of rotating flagella that propels the bacteria. By increasing the activity of bacteria, Shuang demonstrated a two-step scenario of a transition from an equilibrium uniformly aligned LCLC to an out-of-equilibrium "topological turbulence": First, the swimming bacteria cause a periodic bending instability, which is followed by nucleation and chaotic dynamics of topological defects–disclinations. Shuang's experiments thus revealed quintessential features of the interplay of hydrodynamics and topology in the

out-of-equilibrium active matter. For this work, Shuang received the Glenn H. Brown scholarship for the biology-related exploration of liquid crystals on the occasion of the 50th anniversary of the Liquid Crystal Institute. He also received the first prize for a poster presentation at the Spring School on Active Matter in Beijing, China, in 2015.

Shuang's results on viscoelastic properties of LCLCs are already helping many other researchers who explore this fascinating type of self-assembled LCs. His work on living liquid crystals has received more than 60 citations within the first 18 months since publication; it is labelled as "Highly cited paper" by the Thomson Reuters Web of Science. Further developments of the research pioneered by Shuang might help to use the chromonic LCs as an instrument to control bacterial behavior and even encourage them to perform useful mechanical work at the microscale.

Kent, OH, USA
October 2016

Prof. Oleg D. Lavrentovich

Acknowledgements

There are many people to whom I am indebted during my graduate study.

It won't be successful and so enjoyable without the mentoring and support from my advisor Dr. Oleg D. Lavrentovich. From him, I not only learnt how to solve scientific problems, but also how to be a scientist. There is an old saying in China, "the greatest gratitude is beyond words." Exactly.

I am thankful to the laboratory members and to my collaborators for constant help, inspiration, encouragement, and more importantly, healthy criticisms: Dr. Sergij V. Shiyanovskii, Dr. Yuriy A. Nastishin, Dr. Young-Ki Kim, Dr. Heung-Shik Park, Dr. Luana Tortora, Dr. Samuel N. Sprunt, Dr. Igor Aranson and Dr. Andrey Sokolov. Also to Jie Xiang, Dr. Volodymyr Borshch, Dr. Israel Lazo, Dr. Bohdan Senyuk, Chenhui Peng, Greta Cukrov, Bingxiang Li, Taras Turiv for fruitful discussions and fun memories.

Looking back to where it all started, I feel very fortunate to be enrolled in the Chemical Physics Interdisciplinary Program. Faculties, technical and administrative staffs, and fellow graduate students of the Liquid Crystal Institute constructed such a friendly and supportive family. I am especially thankful to Dr. Peter Palffy-Muhoray, who led me into the graduate study as a curricular advisor and remains a timeless inspiring friend in and beyond physics.

I am deeply grateful to my parents who installed in me curiosity and the ability to work hard. Last but not least, I am thankful to my friends who always stand by my side.

November 2016 Shuang Zhou
Cambridge, MA, USA

Contents

1 Introduction 1
1.1 Lyotropic Chromonic Liquid Crystals 1
1.2 Active Colloids and Collective Behavior 4
1.3 Scope and Objectives of the Dissertation 7
References 9

2 Elasticity of Lyotropic Chromonic Liquid Crystals Probed by Director Reorientation in Magnetic Field 13
2.1 Introduction 13
2.2 Samples and Experimental Set-Up 14
2.3 Results 16
2.3.1 Homeotropic Cells, Bend Constant K_3 16
2.3.2 Planar Cells, Splay Constant K_1 16
2.3.3 Planar Cells, Twist Constant K_2 17
2.4 Discussion and Conclusion 18
2.5 Supplemental Information 21
2.5.1 Estimation of Average Aggregation Length 21
2.5.2 Measurement of Diamagnetic Anisotropy $\Delta\chi$ 22
2.5.3 Measurements of Density ρ and Volume Fraction ϕ 24
2.5.4 Optical Response in Bend Frederiks Transition 25
2.5.5 Optical Simulation to Determine Splay Constant K_1 26
2.5.6 Planar Cells, Twist Constant K_2 28
References 30

3 Ionic-Content Dependence of Viscoelasticity of the Lyotropic Chromonic Liquid Crystal Sunset Yellow 33
3.1 Introduction 33
3.2 Materials and Methods 34
3.2.1 LCLC SSY with Ionic Additives 35
3.2.2 Viscoelastic Constants Measurement 35

3.3 Results and Discussions 36
3.3.1 Splay Constant K_1 36
3.3.2 Bend Constant K_3 38
3.3.3 Twist Constant K_2 39
3.3.4 Rotation Viscosity γ_1 40
3.4 Conclusion 41
3.5 Supplemental Information 42
3.5.1 Estimation of E_e 42
3.5.2 Volume Fraction ϕ 42
3.5.3 Diamagnetic Anisotropy $\Delta\chi$ 43
3.5.4 Birefringence Δn and Scalar Order Parameter S 45
3.5.5 Measurement of Rotation Viscosity γ_1 45
References 47

4 Elasticity, Viscosity, and Orientational Fluctuations of a Lyotropic Chromonic Nematic Liquid Crystal Disodium Cromoglycate 51
4.1 Introduction 51
4.2 Experimental Details 52
4.2.1 Materials 52
4.2.2 Experimental Set-Up 53
4.3 Elastic Constants 56
4.4 Viscosities 63
4.5 An Additional Mode in Bend Geometry 66
4.6 Conclusions 70
4.7 Supplemental Information: Verification of K_1 and the Diamagnetic Anisotropy $\Delta\chi$ of DSCG 70
4.8 A Summary of the Viscoelastic Properties of LCLCs 71
References 73

5 Living Liquid Crystals 77
5.1 Introduction 77
5.2 Materials and Methods 78
5.2.1 Bacteria 78
5.2.2 LLC Preparation 78
5.2.3 Videomicroscopy 79
5.2.4 PolScope Microscopy 79
5.3 Results and Discussions 80
5.3.1 Single Bacteria Motion 80
5.3.2 Collective Behavior 83
5.4 Conclusions 87

5.5 Supplemental Information 87
5.5.1 Optics of Director Patterns in the Wake of a Moving Bacterium 87
5.5.2 Optics of Director Patterns Distorted by Flows Produced by Individual Bacterium 88
References 91

6 Summary 93

List of Figures

Figure 1.1 Molecular structures of some lyotropic chromonic liquid crystal materials 2

Figure 1.2 Molecular structure and schematic of a SSY-water LCLC. **a** Molecular structure and schematic of the disassociation of sodium ions from a single molecule in water. **b** Schematic of SSY assembly in water (represented by the *blue background*) to form nematic LCLC; aromatic centers stack on top of each other while the sodium ions are disassociated, leaving the aggregates negatively charged 3

Figure 1.3 "Pusher" versus "puller" swimmers. **a** shows a pusher swimmer, best represented by rod-shaped bacteria such as *E-coli* or *Bacillus subtilis* [51]. The forces (shown with *red arrows*) that drive the flow are pointing outwards along the swimming direction **v**. **b** shows a puller swimmer, best represented by green algae *Chlamydomonas reinhardtii* [52]. *Black arrows* on bacteria bodies show direction of motion of bacteria parts. *Grey curved arrows* show schematic flow field 5

Figure 1.4 Collective motion at different scales and in different media. **a** High density suspension of *Bacillus subtilis* powers unidirectional rotation of asymmetric gears (with reprint permission of Fig. 2 of "Swimming bacteria power microscopic gears." Proceedings of the National Academy of Sciences 107(3):969–974 by Sokolov A., Apodaca M. M, Grzybowski B. A., & Aranson I. S. (2010)). **b** School of fish. (http://www.coralreefphotos.com/big-school-of-fish-schooling-fish-school-of-bogas/) **c** Flock of birds. (http://www.howitworksdaily.com/why-do-birds-flock-together/) **d** Herd of migration animals in South Sudan, Africa. (http://www.reuters.com/article/us-sudan-wildlife-idUSN1225815120070612) 6

Figure 2.1 Schematic of experiment setup. Sample is held in a hot stage for temperature control (not shown here). Both laser 1 and 2 are He–Ne lasers ($\lambda = 633$ nm) 15
Figure 2.2 Temperature and concentration dependences of **a** K_1, K_3 and **b** K_2. The *vertical dash lines* mark the nematic-biphasic transition temperature ($T_{N\to N+I}$) upon heating (same for other plots) for each concentration: 26.6 ± 0.6 °C, 34.4 ± 0.4 °C, 44.1 ± 0.5 °C for $c = 29$, 30.0 and 31.5% respectively 17
Figure 2.3 Temperature and concentration dependences of **a** $\frac{K_2}{-\Delta\chi S}$, **b** $\frac{K_{1,3}}{-\Delta\chi S}$, **c** $\frac{K_{1,3}}{K_2}$, and **d** $\frac{K_1}{K_3}$ 19
Figure 2.4 Temperature and concentration dependences of Δn (at 633 nm) and scalar order parameter $\mathfrak{S}$ 19
Figure 2.5 Temperature and concentration dependences of **a** $\Delta\chi$ and **b** $\Delta\chi/S$ of SSY. Note that $\Delta\chi/S$ remains practically constant when temperature is more than $2-3$ °C below $T_{N\to N+I}$ for each concentration. In the vicinity of $T_{N\to N+I}$, $\Delta\chi$ deviates from $\Delta\chi \propto S$ behavior, likely due to pretransitional effects [34]. We estimate the accuracy of $\Delta\chi$ measurements to be $\pm 10\%$ 23
Figure 2.6 Mass density measurements and calculated volume fraction 24
Figure 2.7 Intensity versus $\mathfrak{B}$ for bend deformation. *Inset* equation is the fitting from linear part (black triangles) of the curve 25
Figure 2.8 Experimental measurement and numerical simulation of $R(B)$ which result in $\frac{K_1}{-\Delta\chi} = 13.2\,\mu$N for a cell of 31.5% SSY with $\Delta n = -0.0768$ for λ = 633 nm at 25 °C 27
Figure 2.9 Periodic pattern in a planar SSY cell induced after abruptly applying a magnetic field of 0.4 T at $\alpha = 90°$ 28
Figure 2.10 Numerically simulated dependencies $\theta(d/2)$ and $\varphi(d/2)$ versus B representing maximum deformations in the mid-plane of cell, for a cell with $d = 23.8\,\mu$m, $\frac{K_2}{-\Delta\chi} = 1.22\,\mu N$, $\frac{K_1}{-\Delta\chi} = \frac{K_3}{-\Delta\chi} = 9.8\,\mu N$ 29
Figure 3.1 Molecular structure (**a**), schematic of nematic LCLC phase (**b**), and phase diagram (**c**) of SSY aqueous solution with ionic additives. **a** The prevailing NH Hydroazone tautomer form is shown. **b** *Red dotes* on aggregates surface represent sulfonate groups, while isolated circles represent disassociated Na^+ ions. **c** *Dash line* marks the nematic to nematic-isotropic phase transition temperature $T_{N\to N+I} = 316.5$ K of the original SSY LCLC 34

Figure 3.2 Temperature and ionic content dependence of **a** splay constant K_1, **b** bend constant K_3 and **c** twist constant K_2 of SSY LCLC, c_{SSY} = 0.98 mol/kg with ionic additives. *Insets* illustrate the corresponding director deformation, where **a** splay creates vacancies that require free ends to fill in, **b** bend can be accommodated by bending the aggregates and **c** twist can be realized by stacking "pseudolayers" of uniformly aligned aggregates within the layers; director rotates only when moving across layers 37

Figure 3.3 **a** K_3 as a function of $\Delta T = T - T_{N\rightarrow N+I}$ for different ionic contents; *insets* show schematically that enhanced Debye screening increases the flexibility of aggregates. **b** For values measured at different ΔT, K_3 show linear relations with λ_D^2, which decreases as c_{NaCl} increases. 39

Figure 3.4 Temperature and ionic content dependence of rotation viscosity γ_1 of SSY LCLC, c_{SSY} = 0.98 mol/kg with ionic additives. *Insets* show the linear relation, $\gamma_1 \propto K_1^2$ for all measurements 41

Figure 3.5 Temperature and ionic content dependences of volume fraction ϕ of SSY 43

Figure 3.6 Temperature dependence of diamagnetic anisotropy $\Delta\chi$ for SSY at fixed concentration c_{SSY} = 0.98 mol/kg, with various amount of additional ionic additives: **a**, **b** $MgSO_4$, **c** NaCl and **d** NaOH 44

Figure 3.7 Temperature dependence of birefringence Δn and scalar order parameter S for SSY at fixed c_{SSY} = 0.98 mol/kg with various concentration of ionic additives: Δn of SSY with additional **a** $MgSO_4$ and **b** NaCl; S of SSY with additional **c** $MgSO_4$ and **d** NaCl 45

Figure 3.8 Measurement of rotational viscosity γ_1 from the relaxation of magnetic field induced twist. **a** Intensity increase in response to suddenly applied magnetic fields $B > B_{th}$; B_{th} is the threshold field of twist Frederiks transition. **b** Intensity decay in response to suddenly reduced magnetic field. **c** Numerical simulation shows that intensity increases quadratically with the mid-plane twisting angle φ_0. **d** Linear fit of $1/\tau_0$ versus B^2, where the rotation viscosity γ_1 can be extracted from the slope 47

Figure 4.1 **a** Structure of the DSCG molecule and generic representation of LCLC aggregates formed in aqueous solution. (Each disk in the aggregate stack may represent single or paired DSCG molecules.) **b**, **c** Schematic of experimental light scattering geometries used in our measurements: **b** "1&2", splay + twist (*pure splay shown*)

geometry and **c** "3" bend-twist (*pure bend shown*) geometry. The *green arrows* indicate the incident ($\mathbf{k_i}$) and scattered ($\mathbf{k_s}$) light, with the polarization of light is in the plane of the *arrows* 53

Figure 4.2 Correlation functions (open *circles*) collected at T = 294 K for $q_{\parallel} = 1.64 \times 10^6$ m^{-1} in a bend (*left*) and for $q_{\perp} = 1.00 \times 10^7$ m^{-1} in splay + twist geometries (*right*) for the nematic LCLC formed by 14 wt% DSCG in water. Solid lines represent fits of the correlation functions (double exponential in the splay + twist geometry, stretched double exponential in bend geometry) to obtain relative normalized amplitudes I_α and relaxation rates Γ_α ($\alpha = 1 - 3$), of the fluctuation modes. In the bend geometry, the analysis reveals an additional, weak mode Γ_4. In this case, the best single-exponential fit (the *dashed line*) clearly misses the data in the ($10^{-4} - 10^{-3}$) s region (*left inset*). The *right inset* shows the relaxation time spectrum obtained by the regularization method [26] for the bend geometry correlation function; the small secondary peak confirms the presence of the additional mode 55

Figure 4.3 Temperature and concentration dependences of elastic constants of **a** splay K_1, **b** bend K_3 and **c** twist K_2 in nematic phase. *Dashed vertical lines* on the horizontal axes indicate the transition temperature from nematic to nematic-isotropic coexistence phase. The *inset* shows K_1 has an exponential dependence of temperature T. K_3 and K_2 fit well with linear functions of temperature T 57

Figure 4.4 Temperature and concentration dependences of the ratios between elastic constants. **a** K_1/K_3, **b** K_1/K_2 both increase as T decreases or ϕ increases; **c** K_3/K_2 remains practically constant for a wide range of T, but decreases at $T \approx 294$ K for 18 wt% 58

Figure 4.5 Mechanism of elastic deformation in LCLC, following Meyer et al. [15]. **a** Flexible rods accommodate bend deformation by deforming the rods. **b** Splay deformation tends to create vacancies that require free ends (marked by *dashed lines*) to fill in. **c** Twist deformation causes minimum inter-aggregates interference by arranging aggregates in layers 59

Figure 4.6 Temperature and concentration dependences of viscosities and their ratios: **a** η_{splay}, **b** η_{twist}, **c** η_{bend} and **d** $\eta_{splay}/\eta_{twist}$ over the nematic range. *Dashed lines* in the horizontal axis indicate T_{ni} 64

Figure 4.7 An aggregate of LCLC rotates in a transverse shear flow, as one can find in a twist deformation, following Meyer et al. [15] 65
Figure 4.8 "C"- (*left*) and "Y"-type (*right*) stacking defects in chromonic aggregates 67
Figure 4.9 Verification of K_1 value using the technique of director reorientation in a magnetic field (**a**) and the diamagnetic anisotropy $\Delta\chi$ of DSCG at various concentration and temperature (**b**). Note that $\Delta\chi$ is dimensionless in SI unit 71
Figure 5.1 Distortion of the nematic director detected by optical microscopy. **a** Snapshot of swimming bacteria observed under a microscope with slightly de-crossed polarizer (P) and analyzer (A). The bacterium shown in *green box* swims from the *right* to *left*. **b** Optical retardance pattern around a swimming bacterium, see also Figs. 5.4, 5.5 and 5.6. **c** Time evolution of the director waves created by rotating flagella in the co-moving reference frame. **d** Space-time diagram for director waves extracted for the bacterium shown in panel **c**. A total of 240 cross-sections were extracted from 2.4 s video. *Dashed green line* depicts phase velocity of the flagella wave. *Dots* mark an immobilized dust particle. **e** The trajectory of a single bacterium around a tactoid. **f** Trace of isotropic tactoids left by a bacterium at temperature about 0.5 °C below the nematic-biphasic transition point. Observations are made under a microscope with slightly de-crossed polarizer (P) and analyzer (A). Scale bar 5 μm (**a**, **b**), 2 μm (**c**), 10 μm (**e**), 20 μm (**f**). 81
Figure 5.2 Emergence of a characteristic length scale in LLCs. **a**, **b** LLC with inactive bacteria is at its equilibrium state with the director and bacteria (*highlighted by ellipses*) aligned uniformly along the rubbing direction; **c**, **d** active bacteria produce periodically distorted director. **e** Proliferation of *stripe pattern* in the sample of thickness $h = 20$ μm and for low concentration of bacteria, $c \approx 0.9 \times 10^9$ cells/cm^3. Oxygen permeates from the left hand side. **f** LLC patterns in thicker sample ($h = 50$ μm) and for higher concentration of bacteria, $c \approx 1.6 \times 10^9$ cells/cm^3. *White arrow* points toward a higher concentration of oxygen. **g** Zoomed area in panel **f** shows nucleating disclinations of strength +1/2 (*semi-circles*) and −1/2 (*triangles*). *Bright dashes* visualize bacterial orientation. **h** Dependence of characteristic period ξ on c and h; *dashed lines* depict fit to theoretical prediction $\xi = \sqrt{\frac{Kh}{c\alpha_0 l U_0}}$. *Inset* illustrates collapse of the data into a universal behavior that follows from the theoretical model. **i** Director realignment

(shown as a *rod*) caused by the bacterium-generated flow (shown by *dashed lines with arrows*). Scale bar 50 μm (**a**–**d**), 100 μm (**e**–**g**). Error bars are ± 10% SEM (standard error of the mean), except for ± 30% SEM at $c/c_0 = 5.05$ 84

Figure 5.3 LLC in sessile drop. **a** Texture with multiple disclination pairs, *green rectangle* indicates the region shown in (**b**, **c**, **d**). Bacteria are aligned along the local nematic director, as revealed by the fine stripes. Scale bar 30 μm. No polarizers. (**b**, **c**, **d**) LLC texture with −1/2 and 1/2 disclinations and the pattern of local flow velocity (*blue arrows*) determined by particle-image velocimetry. The flow typically encircles the close pair of defects. 85

Figure 5.4 Light intensity pattern for a linearly polarized light passing through the twisted director configuration as described in the Sect. 5.5.1. **a**, **b** polarizing microscopy textures of oblique *black and white regions* in the wake area of swimming bacteria. **c**, **d**, **e** Optical simulation of director textures deformed by the helicoidal flagella viewed between two linear polarizers making a different angle $\delta_{AP} = 80°$ (**c**), 90° (**d**) and 100° (**e**). Scale bar 5 μm 88

Figure 5.5 Director distortions around an immobile bacterium. **a** Optical polarizing microscopy texture with de-crossed polarizers shows a "*butterfly*" pattern. **b** PolScope texture maps director pattern (*yellow lines*) resembling an "X" letter; color scale is proportional to the angle that the local director makes with the long axis of the image. **c** A schematic representation showing how the director (*red bar*) deviates from $\hat{\mathbf{n}}_0 = (1, 0, 0)$ (*blue dashed lines*) due to the flow (*blue arcs with arrows*) induced by non-swimming two-tail bacterium. **d**, **e**, **f** Optical simulation of the director pattern in part **b** shows the *butterfly* pattern in the intensity map when the two polarizers are crossed at different angles (**a**, **b**). Scale bar 5 μm (**a**), 10 μm (**b**) 89

Figure 5.6 Chiral symmetry breaking of the LLC director pattern caused by a rotating bacterium. **a**, **b** Schematics of the flows generated by the rotating bacterium. **c** Scheme of the director twist along the vertical z-axis 90

List of Table

Table 4.1 Viscoelastic parameters of different liquid crystals 58

Chapter 1
Introduction

1.1 Lyotropic Chromonic Liquid Crystals

Lyotropic liquid crystals (LCs) represent an extended family of dispersed systems that possesses a long-range orientational order (the prefix lyo- means "to loosen, dissolve" in Greek) [1, 2]. The basic building units of such systems are usually super-molecular assemblies of high aspect ratio dispersed in solvent (usually water). Examples include: amphiphiles that form wormlike micelles, double-strain DNA (ds-DNA) molecules, tobacco mosaic viruses (TMV) representing rigid protein polymer rods, and cylindrical stacks of disk-like molecules in water solution. Molecules in the last category are usually drugs or dyes molecules that have a polyaromatic center and ionizable groups at the periphery. The liquid crystal phases formed by such molecules in water solution are called lyotropic chromonic liquid crystals, or LCLCs [3–7]. Classical examples include antiasthma drug disodium cromoglycate (DSCG), food and textile dyes Sunset Yellow (SSY), Allura red, Tartrazine, Blue 27, Violet 20, Fig. 1.1, and many more. An extended family of chromonics also includes ds-DNA assemblies [4, 8] which share many structural features with the classical LCLCs such as SSY and DSCG, including: repeating distance of molecules along the aggregate's axis being 0.34 nm, diameter of aggregates being 1–2 nm, persistence length being on the order of tens of nanometers, and so on.

In lyotropic LC, the underlying mechanism for a dispersion of elongated objects to achieve an orientationally ordered state is very different from that of thermotropic LCs. In thermotropic LCs, the basic building units are molecules of *covalently fixed shape*. The ordered phases (nematic, smectic, etc.) occur at a lower temperature when the molecular interactions favoring parallel arrangement of neighboring molecules win over entropy. In lyotropic LCs, the orientational order occurs when the building units sacrifice orientational freedom and align with neighbors to gain translational entropy. For example, in an Onsager-type system [9] composed of *identical rigid rods*, the isotropic-to-nematic phase transition occurs only if the

© Springer International Publishing AG 2017

S. Zhou, *Lyotropic Chromonic Liquid Crystals*, Springer Theses,
DOI 10.1007/978-3-319-52806-9_1

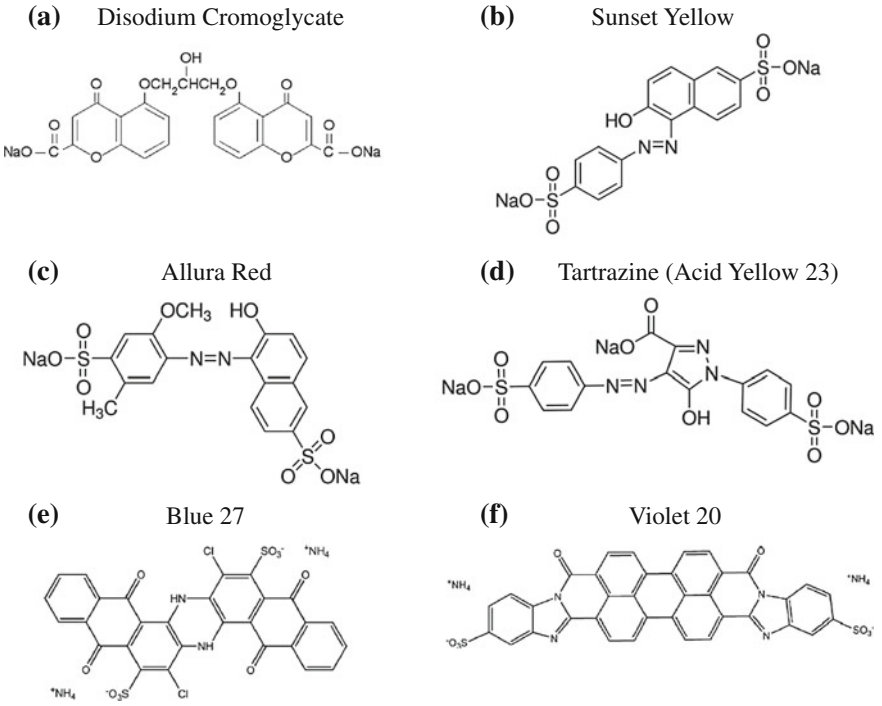

Fig. 1.1 Molecular structures of some lyotropic chromonic liquid crystal materials

volume fraction of the rods in the system is larger than a threshold value, $\phi > \phi_{\text{nem}} = 4.5D/L$, where L and D are the length and diameter of the rods, respectively. Temperature does not play a role here, leaving the volume fraction ϕ, or equivalently, the mass concentration c, being the only tuning parameter. In comparison, the phase behavior of lyotropic chromonic liquid crystals can be controlled by both concentration and temperature, due to the very different underlying mechanism of how the basic building unites of the LCLCs, the cylindrical aggregates, are formed. When LCLC molecules are dissolved in water, the hydrophobic aromatic centers stack on top of each other. At the same time, positive ions at the periphery of the molecules are disassociated, leaving behind negative charged aggregates, with a maximum charge density $\tau^{\max} e = 6e/\text{nm}$, Fig. 1.2. The effective interaction, counting both the attraction of the aromatic centers (E_0) and electrostatic repulsions of the periphery (E_e) is characterized by the so-called scission energy $E = E_0 - E_e \approx 10 k_B T$, an energy needed to break one aggregate into two. The equilibrium average length of chromonic aggregates, as described more in detail later in this thesis, is determined by E, $\bar{L} \propto \exp\left(\frac{E}{2k_B T}\right)$ [3, 4, 10, 11]. At lower temperature, the length of the aggregates increases [12], thus an ordered phase is preferred over isotropic phase. Moreover, keeping c and T the same, but increasing the ionic concentration in the system screens the repulsion between

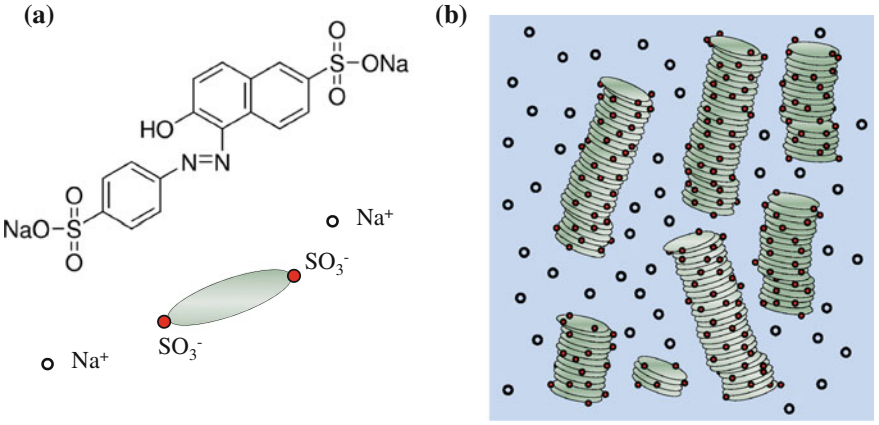

Fig. 1.2 Molecular structure and schematic of a SSY-water LCLC. **a** Molecular structure and schematic of the disassociation of sodium ions from a single molecule in water. **b** Schematic of SSY assembly in water (represented by the *blue background*) to form nematic LCLC; aromatic centers stack on top of each other while the sodium ions are disassociated, leaving the aggregates negatively charged

molecules in the aggregates, decreases E_e, thus increases $\bar{L}$, promoting a more ordered phase. On the contrary, adding NaOH enhances the disassociation of sodium ions, increases E_e, thus decreases $\bar{L}$, destabilizes the ordered phase. Phase dependence of LCLCs on c, T, c_{ion}, pH value, presence of crowding agents, etc. are experimentally studied in Ref. [12, 13], and also in Chaps. 2–4 in this thesis.

Another important difference between LCLCs and the Onsager-type lyotropic LCs composed of rigid rods (such as water suspension of TMV [14]) is that LCLC aggregates are flexible. The flexibility of LCLC aggregates is characterized by the persistence length λ_p, a length over which unit vectors tangential to the aggregates lose correlation. Since E is on the order of $10k_BT$, the aggregates may be bent easily by thermal fluctuations. In a similar system composed of ds-DNA molecules face-to-face assembled with a scission energy $E \approx (4-8)k_BT$, the persistence length is estimated to be 50 nm [8]. The flexibility of the aggregates can be influenced by ion concentration which controls the Debye screening length λ_D. Since the bend deformation brings negative surface charges closer and causes stronger electrostatic repulsion, a decreased λ_D at higher ionic concentration relieves the repulsion, and makes the aggregates more flexible. Similar effects of ionic contents on flexibility of biomolecules are of prime importance in biological processes such as DNA wrapping around nucleosomes, packing inside bacteriophage capsids, biding to proteins and so on [15, 16].

Despite the growing interests of the LCLCs, very little is known about their elastic and viscous properties. Knowledge of viscoelastic constants, such as the Frank elastic moduli in the nematic phase and the viscosities associated with different flow geometries, is of essential importance to understand both static and dynamic phenomena such as template assisted alignments [17–20], behavior of LCLCs in samples

with various thickness [21–23], LCLC-guided orientation of nanoparticles [24], shape of LCLC tactoids [25, 26], effect of spontaneously broken chiral symmetry [27, 28], and flow behavior of LCLC [29]. LCLCs also provide a model system to study how these macroscopic viscoelastic properties are connected with microscopic features such as the contour length L and the persistence length λ_p, which can help our understanding of the biological systems such as DNA assemblies, where very often direct measurements of microscopic properties are not easily available.

1.2 Active Colloids and Collective Behavior

If liquid crystals can be described as "passive" matters, there is another kind of systems, known as "*active matters*", composed of self-driven individuals that use stored or locally harvested energy to drive systematic movement [30]. A distinctive feature of active matter, as compared to non-equilibrium state of a passive system (e.g. LC director reorientation driven by external field), is that the energy input that drives the system out of equilibrium is local, often at the level of each particles, rather than at the boundaries of the system. A particular interesting subset of active matter is active colloids. Colloids are suspensions of particles whose sizes range from 10 nm to 100 μm, usually in fluid or gas. They are prevalent in our daily life (e.g., milk, ink, blood) and play critical roles in many industries (e.g., food, printing, medicine, nanotechnology) [31]. Interactions between colloids are governed by various forces, such as steric repulsion, electrostatic and magnetic forces, van der Waals forces, entropic forces, hydrodynamic forces, etc. [32]. Colloidal science has been a traditionally important field of research. A large body of work has been dedicated to the equilibrium self-assembled colloidal structures [33, 34], which have important potential in applications such as photonic band gap (PBG) structures [35–37]. Bringing activity into colloidal particles gives rises to new fascinating phenomena, including: activity induced crystallization at low density [38], self-organization of microtubules driven by molecular motor [39], spontaneous and constant creation, annihilation and self-propulsion of topological defects [40, 41], reduction of viscosity in active particle suspension [42, 43] and so on. Self-assembled active colloids also open new doors to produce materials with functions not available in equilibrium conditions, such as self-healing [44, 45], self-propulsion [46–48], formation of unusual shapes (reconfigurable snakes, asters, etc.) and transport of cargo [48, 49].

The simplest way to create an active colloid is to suspend microorganisms in water; examples include bacteria [50] such as *Escherichia coli (E-coli)* [51] and *Bacillus subtilis*, green algae such as *Chlamydomonas reinhardtii* [52] and sperm cells [53]. These self-motile microorganisms are also called microswimmers. Depending on the direction of flow field along the axis of swimming, they are classified as "puller" or "pusher" types [30, 54]. For example, bacteria such as *E-coli* and *Bacillus subtilis* are pushers, since they pump fluid away from them along the

direction of propulsion, by rotating helicoidal flagella, Fig. 1.3a. *Chlamydomonas reinhardtii* is a puller, as it pulls fluid towards its body along the direction of motion, by stoking two arm-like flagella, Fig. 1.3b. The pair of forces that drive the fluid motion are pointing inward (puller) or outward (pusher), corresponding to a positive or negative force dipole on the swimmer body, respectively [30]. Since the self-motile swimmers are not driven by an external field (electric, magnetic, flow field, etc.), the net force is zero. Inspired by the biological microswimmers, researchers developed synthetic microswimmers in a variety of forms [55–57], including bimetallic rods that use chemical reaction with hydrogen peroxide [58], water droplets that use Marangoni effect to drive themselves in oil [59], metallic-dielectric Janus spherical particles propelled by an electric field [60], high-speed bilayer microtubes [61], magnetic field [48, 49] or light driven [38] microspheres, silicon dioxide swimmers with nanostructured helical shape [62], and so on.

In this thesis, we deal with a typical "pusher" microswimmer, bacteria *Bacillus subtilis*. *Bacillus subtilis* is a rod-shaped bacterium 5–7 μm in body length and 0.7 μm in diameters. It has about 20 pieces of helicoidal 10-μm long flagella filaments attached to the bacterial body. In isotropic media, the bacteria swim in the so called "run-and-tumble" fashion [63, 64]. During an approximately 1 s "run" phase, the flagella form a bundle at one end of the bacterial body and rotate counter-clock wise (ccw, viewing behind a swimming-away bacterium along the body axis), thus powering unidirectional "head-forward" motion. In the following tumble phase of about 0.1 s, one or a few of the flagella reverse their rotation to

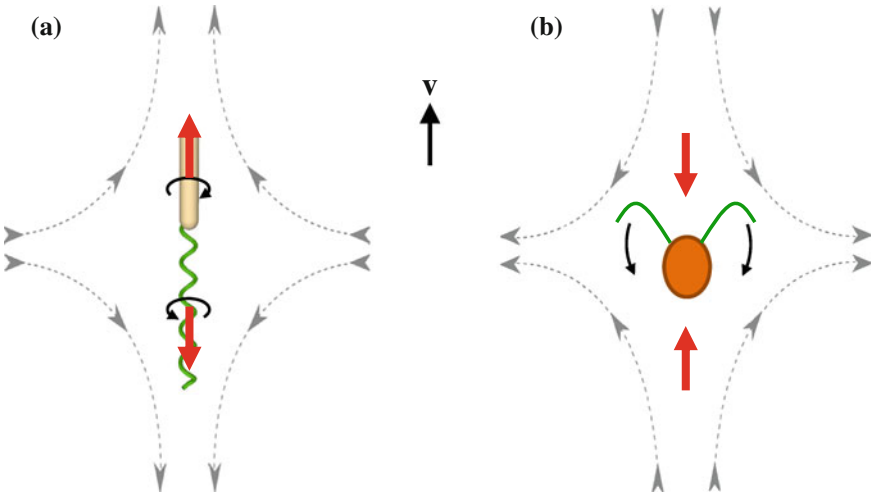

Fig. 1.3 "Pusher" versus "puller" swimmers. **a** shows a pusher swimmer, best represented by rod-shaped bacteria such as *E-coli* or *Bacillus subtilis* [51]. The forces (shown with *red arrows*) that drive the flow are pointing outwards along the swimming direction **v**. **b** shows a puller swimmer, best represented by green algae *Chlamydomonas reinhardtii* [52]. *Black arrows* on bacteria bodies show direction of motion of bacteria parts. *Grey curved arrows* show schematic flow field

clock wise (cw) and leave the bundle, causing bacterium to "tumble" and change its orientation randomly. Then flagella rotate ccw again, forming the bundle and power the forward motion in a new direction. The motility of this aerobic bacterium can be controlled by the amount of dissolved oxygen.

One spectacular phenomenon observed in an isotropic *Bacillus subtilis* suspension is the spontaneous collective motion [54, 64–66]: at high enough concentration ($\sim 2\%$ by volume), bacteria swarm together with their velocity field correlated over ~ 10 times body length and with a up to 4 fold increase in speed as compared to individual bacterium at a dilute concentration [67, 68]. In fact, collective motion can be found in many active matter systems [69–72] of different sizes, ranging from microscopic organisms such as bacteria swarms, to macroscopic creatures such as fish schools, birds flocks and herds of mammals, Fig. 1.4. In the collective motion mode, bacteria suspension exhibit unusual properties such as greatly reduced viscosity [42, 52] and increased diffusivity [73, 74]. A very interesting phenomenon is the unidirectional rotation of asymmetric millimeter size gears [75, 76] driven by the chaotic motion of swimming bacteria, Fig. 1.4a. By contrast, in an equilibrium system of suspension of passive particles, this rotation cannot be observed since it is against the second law of thermodynamics. However,

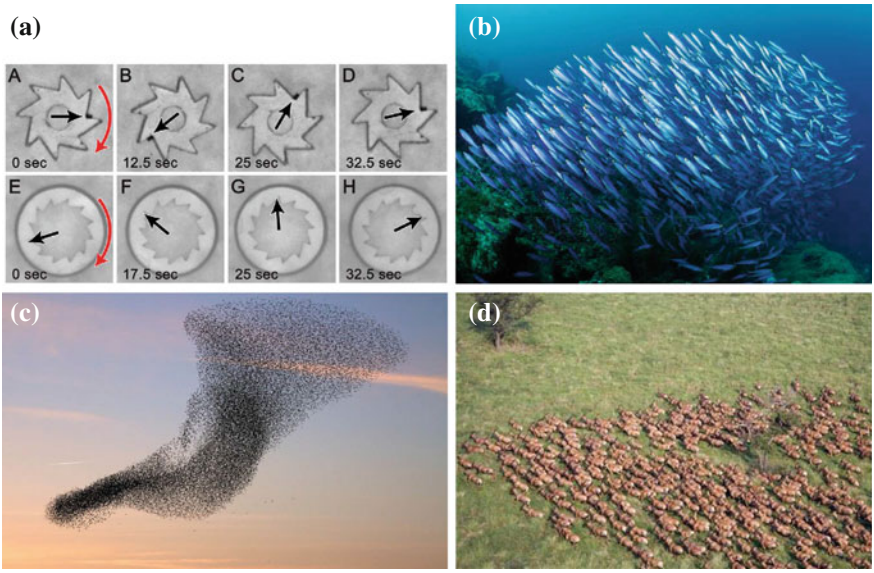

Fig. 1.4 Collective motion at different scales and in different media. **a** High density suspension of *Bacillus subtilis* powers unidirectional rotation of asymmetric gears (with reprint permission of Fig. 2 of "Swimming bacteria power microscopic gears." Proceedings of the National Academy of Sciences 107(3):969–974 by Sokolov A., Apodaca M. M, Grzybowski B. A., & Aranson I. S. (2010)). **b** School of fish. (http://www.coralreefphotos.com/big-school-of-fish-schooling-fish-school-of-bogas/) **c** Flock of birds. (http://www.howitworksdaily.com/why-do-birds-flock-together/) **d** Herd of migration animals in South Sudan, Africa. (http://www.reuters.com/article/us-sudan-wildlife-idUSN1225815120070612)

in condensed bacterial suspension, even though the motion of individual particles is still random and looks very much like Brownian motion of passive particles, one can still harvest energy, a signature that the system is not in the equilibrium states.

Collective motion in active matter systems results in ordered states with polar [77, 78] or nematic [79–82] symmetry. For example, in a system composed of microtubules, crowding agents and molecular motors, Dogic and his collaborators [40, 41] demonstrate that at high enough concentration, microtubules absorbed on flat oil-water interface undergo a transition to the nematic phase. When the activity is turned on with adenosine triphosphate (ATP) supply, one observes constant creation and annihilation of topological defects of charge 1/2 and −1/2, distinctive from the uniform alignment of director observed in the equilibrium nematic phase. However, in this system, the nematic order and activity are both tightly connected to the parallel aligned microtubules. As a result, one sees only one steady state, i.e., active nematic with topological defects. In this thesis, we take advantage of the non-toxic lyotropic chromonic liquid crystal disodium cromoglycate [83] and mix in active particles, the bacteria *Bacillus subtilis*. By varying the bacterial concentration and oxygen supply, we independently (and continuously) change the activity of the system from zero to high values. As a result, our system exhibits three major steady states: (i) equilibrium uniform nematic embedding small amount of active particles in their inactive form (non-swimming), (ii) active nematic with uniform bend modulation, and (iii) active nematic with topological defects. We also demonstrate that LCLCs have the ability to control the motion of active particles through the spatially varying director field, and to visualize the fluid motion induced by 24 nm thick bacterial flagella. The studies of this system that we call a living liquid crystal are presented in Chap. 5.

1.3 Scope and Objectives of the Dissertation

The scope of this dissertation is two-fold. First, we aim to understand the elastic and viscous properties of LCLCs, and how factors such as temperature, concentration and ionic contents influence them. Second, we study the interaction between self-propelled particles (bacteria *Bacillus subtilis*) and the long-range nematic order provided by DSCG LCLC. The studies involve various experimental techniques, such as magnetic field induced Frederiks transition, dynamic light scattering (DLS), polarizing optical microscopy, LC-PolScope and video-microscopy.

The objectives of the dissertation are to study experimentally: (i) the temperature and concentration dependence of Frank elastic moduli of Sunset Yellow LCLC, using magnetic Frederiks transition technique; (ii) the ionic-content dependences of elastic moduli and rotation viscosity of Sunset Yellow LCLC, using the same technique; (iii) elasticity, viscosity and orientational fluctuation of DSCG LCLC using dynamic light scattering technique; (iv) the interaction between active self-propelling bacteria and the nematic order in the living liquid crystal.

The dissertation is organized as follows.

Chapter 2 describes the experimental study of Frank elastic constants of SSY LCLC, probed by Frederiks transition in a magnetic field. In this study, we observed unusual anisotropy of elastic properties. Namely, the splay K_1 and bend K_3 constants are found to be 10 times larger than the twist constant K_2. K_1 has the strongest temperature dependence among all three. We explain our findings through the idea of semiflexible aggregates, whose length dramatically increases as temperature decreases or concentration increases.

Chapter 3 is an extension of the study in Chap. 2 in two aspects: (1) we aim to understand how ionic content in the system influences the properties of LCLC; (2) we measure rotation viscosity γ_1 by the relaxation of twist deformation in a magnetic field, in addition to the Frank elastic moduli. Here we fix the concentration of SSY but vary the type and concentration of ionic components and temperature. Using the same magnetic Frederiks transition technique, we find that the ionic content influences the elastic constants in dramatic and versatile ways. For example, the monovalent salt NaCl decreases K_3 and K_2, but increases γ_1, while pH agent NaOH decreases all of them.

Chapter 4 deals with LCLC material DSCG. DSCG is not only the earliest and most studied LCLC material, but also a bio-compatible one [83] with optical transparency in visible wavelength, an advantage for optical study and applications [84]. Dynamic light scattering technique allows one to extract both elastic moduli and viscosity coefficients at the same time. The results obtained are rather astonishing. In addition to anisotropy of elastic constants, $K_1 \approx K_3 \approx 10K_2$, which is similar to SSY LCLC, the viscosity of bend deformation $\eta_{bend} \approx \eta_{bend}^{5CB}$ can be up to 4 orders of magnitude smaller than η_{splay} and η_{twist}. The temperature dependences of K_1, η_{splay} and η_{twist} are exponential. Again, we explain our findings through the idea of semi-flexible aggregates whose lengths strongly depend on T. We also find an additional mode in the DLS experiments, which we attribute to the diffusion of stacking faults of the aggregates.

In Chap. 5, we combine two fundamentally different systems, the nematic DSCG LCLC and bacteria *Bacillus subtilis*, in order to create the living liquid crystal in which the activity and orientational order can be tuned independently. The coupling between the active particles and long-range nematic order results in intriguing dynamic phenomena, including (i) nonlinear trajectories of bacterial motion guided by a non-uniform director, (ii) local melting of the liquid crystal caused by the bacteria-produced shear flows, (iii) activity-triggered transition from a non-flowing equilibrium uniform state into a flowing out-of-equilibrium one-dimensional periodic pattern and its evolution into a turbulent array of topological defects, and (iv) birefringence enabled visualization of micro-flow generated by the nanometers thick bacterial flagella.

Chapter 6 summarizes the results in this dissertation.

The following publications cover the topics discussed in the dissertation:

[1]: Shuang Zhou, Yu. A. Nastishin, M.M. Omelchenko, L. Tortora, 1 V. G. Nazarenko, O. P. Boiko, T. Ostapenko, T. Hu, C. C. Almasan, S. N. Sprunt, J. T. Gleeson, and O. D. Lavrentovich, “Elasticity of Lyotropic Chromonic Liquid

Crystals Probed by Director Reorientation in a Magnetic Field", *Phys. Rev. Lett.,* **109**, 037801 (2012)

[2]: Shuang Zhou, Adam J. Cervenka, and Oleg D. Lavrentovich, "Ionic-content dependence of viscoelasticity of the lyotropic chromonic liquid crystal sunset yellow" *Phys. Rev. E,* **90**, 042505 (2014)

[3]: Shuang Zhou, Krishna Neupane, Yuriy A. Nastishin, Alan R. Baldwin, Sergij V. Shiyanovskii, Oleg D. Lavrentovich and Samuel Sprunt, "Elasticity, viscosity, and orientational fluctuations of a lyotropic chromonic nematic liquid crystal disodium cromoglycate", *Soft Matter*, **10**, 6571 (2014).

[4]: Shuang Zhou, Andrey Sokolov, Oleg D. Lavrentovich, and Igor S. Aranson, "Living liquid crystals", *Proc. Natl. Acad. Sci. U. S. A.*, **111**, 1265 (2014)

The research also results in the following publication:

[5]: Andrey Sokolov, Shuang Zhou, Oleg D. Lavrentovich, and Igor S. Aranson, "Individual behavior and pairwise interactions between microswimmers in anisotropic liquid", *Phys. Rev. E,* **91**, 013009 (2015)

and two more publications that are currently being prepared or submitted:

[6]: Shuang Zhou, Andrey Sokolov, Igor Aranson, Oleg D. Lavrentovich, "Controlling dynamic states of active bacterial suspensions through surface alignment of a nematic liquid crystal environment", submitted

[7]: Shuang Zhou, Sergij V. Shiyanovskii, Heung-Shik Park, Oleg D Lavrentovich, "Fine structure of the topological defect cores studied for disclinations in lyotropic chromonic liquid crystals", Nat Comm, accepted

References

1. de Gennes PG, Prost J (1993) The physics of liquid crystals, Clarendon Press, Oxford, p 598
2. Kleman M, Lavrentovich OD (2003) Soft matter physics: an introduction, Springer, New York, p 638
3. Collings PJ, Dickinson AJ, Smith EC (2010) Molecular aggregation and chromonic liquid crystals. Liq Cryst 37(6–7):701–710
4. Lydon J (2011) Chromonic liquid crystalline phases. Liq Cryst 38(11–12):1663–1681
5. Park HS, Lavrentovich OD (2012) Lyotropic chromonic liquid crystals: emerging applications, In: Li Q (ed) Liquid crystals beyond displays: chemistry, physics, and applications, Wiley, Hoboken, New Jersey, pp 449–484
6. Tam-Chang S-W, Huang L (2008) Chromonic liquid crystals: properties and applications as functional materials. Chem Commun 17:1957–1967
7. Vasilevskaya AS, Generalova EV, Anatolii SS (1989) Chromonic mesophases. Russ Chem Rev 58(9):904
8. Nakata M et al (2007) End-to-end stacking and liquid crystal condensation of 6-to 20-base pair DNA duplexes. Science 318(5854):1276–1279
9. Onsager L (1949) The effects of shape on the interaction of colloidal particles. Ann NY Acad Sci 51:627–649
10. Dickinson AJ, LaRacuente ND, McKitterick CB, Collings PJ (2009) Aggregate structure and free energy changes in chromonic liquid crystals. Mol Cryst Liq Cryst 509:751–762
11. Collings PJ et al (2015) The nature of the assembly process in chromonic liquid crystals. Liq Cryst Rev 3(1):1–27

12. Park HS et al (2008) Self-assembly of lyotropic chromonic liquid crystal sunset yellow and effects of ionic additives. J Phys Chem B 112(51):16307–16319
13. Park HS, Kang SW, Tortora L, Kumar S, Lavrentovich OD (2011) Condensation of self-assembled lyotropic chromonic liquid crystal sunset yellow in aqueous solutions crowded with polyethylene glycol and doped with salt. Langmuir 27(7):4164–4175
14. Dogic Z, Fraden S (2006) Ordered phases of filamentous viruses. Curr Opin Colloid Interface Sci 11(1):47–55
15. Baumann CG, Smith SB, Bloomfield VA, Bustamante C (1997) Ionic effects on the elasticity of single DNA molecules. Proc Natl Acad Sci USA 94:6185–6190
16. Smith SB, Cui Y, Bustamante C (1996) Overstretching B-DNA: the elastic response of individual double-stranded and single-stranded DNA molecules. Science 271(5250):795–799
17. Sousa ME et al (2005) Patterning lyotropic liquid crystals as precursors for carbon nanotube arrays. Appl Phys Lett 87(17):173115
18. Tam-Chang S-W, Helbley J, Carson TD, Seo W, Iverson IK (2006) Template-guided organization of chromonic liquid crystals into micropatterned anisotropic organic solids. Chem Commun 5:503–505
19. Yi Y, Clark NA (2013) Orientation of chromonic liquid crystals by topographic linear channels: multi-stable alignment and tactoid structure. Liq Cryst 40(12):1736–1747
20. Lohr MA et al (2014) Elasticity-dependent self-assembly of micro-templated chromonic liquid crystal films. Soft Matter 10(19):3477–3484
21. Schneider T, Lavrentovich OD (2000) Self-assembled monolayers and multilayered stacks of lyotropic chromonic liquid crystalline dyes with in-plane orientational order. Langmuir 16(12):5227–5230
22. Tone CM, De Santo MP, Buonomenna MG, Golemme G, Ciuchi F (2012) Dynamical homeotropic and planar alignments of chromonic liquid crystals. Soft Matter 8(32): 8478–8482
23. Nazarenko VG et al (2010) Surface alignment and anchoring transitions in nematic lyotropic chromonic liquid crystal. Phys Rev Lett 105(1):017801
24. Ould-Moussa N et al (2013) Dispersion and orientation of single-walled carbon nanotubes in a chromonic liquid crystal. Liq Cryst 40(12):1628–1635
25. Nastishin YA et al (2005) Optical characterization of the nematic lyotropic chromonic liquid crystals: Light absorption, birefringence, and scalar order parameter. Phys Rev E 72(4):041711
26. Kim Y-K, Shiyanovskii SV, Lavrentovich OD (2013) Morphogenesis of defects and tactoids during isotropic–nematic phase transition in self-assembled lyotropic chromonic liquid crystals. J Phys: Condens Matter 25(40):404202
27. Tortora L, Lavrentovich OD (2011) Chiral symmetry breaking by spatial confinement in tactoidal droplets of lyotropic chromonic liquid crystals. Proc Natl Acad Sci USA 108(13):5163–5168
28. Jeong J, Davidson ZS, Collings PJ, Lubensky TC, Yodh AG (2014) Chiral symmetry breaking and surface faceting in chromonic liquid crystal droplets with giant elastic anisotropy. Proc Natl Acad Sci USA 111(5):1742–1747
29. Yao X (2011) Studies on lyotropic chromonic liquid crystals in nematic and biphasic regions Doctor of Philosophy, Georgia Institute of Technology
30. Marchetti MC et al (2013) Hydrodynamics of soft active matter. Rev Mod Phys 85(3): 1143–1189
31. Hunter RJ, White LR (1987) Foundations of colloid science. Clarendon Press, Oxford
32. Israelachvili JN (2011) Intermolecular and surface forces. Academic Press, Burlington, MA
33. Li F, Josephson DP, Stein A (2011) Colloidal assembly: the road from particles to colloidal molecules and crystals. Angew Chem Int Ed 50(2):360–388
34. Grzybowski BA, Wilmer CE, Kim J, Browne KP, Bishop KJM (2009) Self-assembly: from crystals to cells. Soft Matter 5(6):1110–1128
35. Marlow F, Muldarisnur Sharifi P, Brinkmann R, Mendive C (2009) Opals: status and prospects. Angew Chem Int Ed 48(34):6212–6233

36. Galisteo-López JF et al (2011) Self-assembled photonic structures. Adv Mater 23(1):30–69
37. Kim S-H, Lee SY, Yang S-M, Yi G-R (2011) Self-assembled colloidal structures for photonics. NPG Asia Mater 3:25–33
38. Palacci J, Sacanna S, Steinberg AP, Pine DJ, Chaikin PM (2013) Living crystals of light-activated colloidal surfers. Science 339(6122):936–940
39. Ndlec FJ, Surrey T, Maggs AC, Leibler S (1997) Self-organization of microtubules and motors. Nature 389(6648):305–308
40. Sanchez T, Chen DTN, DeCamp SJ, Heymann M, Dogic Z (2012) Spontaneous motion in hierarchically assembled active matter. Nature 491(7424):431–434
41. Keber FC et al (2014) Topology and dynamics of active nematic vesicles. Science 345(6201):1135–1139
42. Sokolov A, Aranson IS (2009) Reduction of viscosity in suspension of swimming bacteria. Phys Rev Lett 103(14):148101
43. López HM, Gachelin J, Douarche C, Auradou H, Clément E (2015) Turning bacteria suspensions into superfluids. Phys Rev Lett 115(2):028301
44. Kumacheva E, Garstecki P, Wu H, Whitesides GM (2003) Two-dimensional colloid crystals obtained by coupling of flow and confinement. Phys Rev Lett 91(12):128301
45. Osterman N et al (2009) Field-induced self-assembly of suspended colloidal membranes. Phys Rev Lett 103(22):228301
46. Dreyfus R et al (2005) Microscopic artificial swimmers. Nature 437(7060):862–865
47. Tierno P, Golestanian R, Pagonabarraga I, Sagués F (2008) Magnetically actuated colloidal microswimmers. J Phys Chem B 112(51):16525–16528
48. Snezhko A, Belkin M, Aranson IS, Kwok WK (2009) Self-assembled magnetic surface swimmers. Phys Rev Lett 102(11):118103
49. Snezhko A, Aranson IS (2011) Magnetic manipulation of self-assembled colloidal asters. Nat Mater 10(9):698–703
50. Harshey RM (2003) Bacterial motility on a surface: many ways to a common goal. Annu Rev Microbiol 57(1):249–273
51. Schwarz-Linek J et al (2016) Escherichia coli as a model active colloid: a practical introduction. Colloids Surf, B 137:2–16
52. Rafaï S, Jibuti L, Peyla P (2010) Effective viscosity of microswimmer suspensions. Phys Rev Lett 104(9):098102
53. Alvarez L, Friedrich BM, Gompper G, Kaupp UB (2014) The computational sperm cell. Trends Cell Biol 24(3):198–207
54. Koch DL, Subramanian G (2011) Collective hydrodynamics of swimming microorganisms: living fluids. Annu Rev Fluid Mech 43(1):637–659
55. Ebbens SJ, Howse JR (2010) In pursuit of propulsion at the nanoscale. Soft Matter 6(4): 726–738
56. Sengupta S, Ibele ME, Sen A (2012) Fantastic voyage: designing self-powered nanorobots. Angew Chem Int Ed 51(34):8434–8445
57. Ozin GA, Manners I, Fournier-Bidoz S, Arsenault A (2005) Dream nanomachines. Adv Mater 17(24):3011–3018
58. Paxton WF et al (2006) Catalytically induced electrokinetics for motors and micropumps. J Am Chem Soc 128(46):14881–14888
59. Izri Z, van der Linden MN, Michelin S, Dauchot O (2014) Self-propulsion of pure water droplets by spontaneous marangoni-stress-driven motion. Phys Rev Lett 113(24):248302
60. Gangwal S, Cayre OJ, Bazant MZ, Velev OD (2008) Induced-charge electrophoresis of metallodielectric particles. Phys Rev Lett 100(5):058302
61. Gao W, Sattayasamitsathit S, Orozco J, Wang J (2011) Highly efficient catalytic microengines: template electrosynthesis of polyaniline/platinum microtubes. J Am Chem Soc 133(31):11862–11864
62. Ghosh A, Fischer P (2009) Controlled propulsion of artificial magnetic nanostructured propellers. Nano Lett 9(6):2243–2245

63. Darnton NC, Turner L, Rojevsky S, Berg HC (2007) On torque and tumbling in swimming escherichia coli. J Bacteriol 189(5):1756–1764
64. Elgeti J, Winkler RG, Gompper G (2015) Physics of microswimmers—single particle motion and collective behavior: a review. Rep Prog Phys 78(5):056601
65. Mendelson NH, Bourque A, Wilkening K, Anderson KR, Watkins JC (1999) Organized cell swimming motions in bacillus subtilis colonies: patterns of short-lived whirls and jets. J Bacteriol 181(2):600–609
66. Saintillan D, Shelley MJ (2012) Emergence of coherent structures and large-scale flows in motile suspensions. J R Soc Interface 9(68):571–585
67. Sokolov A, Aranson IS, Kessler JO, Goldstein RE (2007) Concentration dependence of the collective dynamics of swimming bacteria. Phys Rev Lett 98(15):158102
68. Sokolov A, Aranson IS (2012) Physical properties of collective motion in suspensions of bacteria. Phys Rev Lett 109(24):248109
69. Vicsek T, Czirók A, Ben-Jacob E, Cohen I, Shochet O (1995) Novel type of phase transition in a system of self-driven particles. Phys Rev Lett 75(6):1226–1229
70. Vicsek T, Zafeiris A (2012) Collective motion. Phys Rep 517(3–4):71–140
71. Toner J, Tu Y, Ramaswamy S (2005) Hydrodynamics and phases of flocks. Ann Phys 318(1):170–244
72. Ramaswamy S (2010) The mechanics and statistics of active matter. Ann Rev Condens Matter Phys 1(1):323–345
73. Wu X-L, Libchaber A (2000) Particle diffusion in a quasi-two-dimensional bacterial bath. Phys Rev Lett 84(13):3017–3020
74. Sokolov A, Goldstein RE, Feldchtein FI, Aranson IS (2009) Enhanced mixing and spatial instability in concentrated bacterial suspensions. Phys Rev E 80(3):031903
75. Sokolov A, Apodaca MM, Grzybowski BA, Aranson IS (2010) Swimming bacteria power microscopic gears. Proc Natl Acad Sci 107(3):969–974
76. Di Leonardo R et al (2010) Bacterial ratchet motors. Proc Natl Acad Sci 107(21):9541–9545
77. Schaller V, Weber C, Semmrich C, Frey E, Bausch AR (2010) Polar patterns of driven filaments. Nature 467(7311):73–77
78. Giomi L, Marchetti MC, Liverpool TB (2008) Complex spontaneous flows and concentration banding in active polar films. Phys Rev Lett 101(19):198101
79. Chaté H, Ginelli F, Montagne R (2006) Simple model for active nematics: quasi-long-range order and giant fluctuations. Phys Rev Lett 96(18):180602
80. Giomi L, Mahadevan L, Chakraborty B, Hagan MF (2011) Excitable patterns in active nematics. Phys Rev Lett 106(21):218101
81. Kemkemer R, Kling D, Kaufmann D, Gruler H (2000) Elastic properties of nematoid arrangements formed by amoeboid cells. Eur Phys J E 1(2):215–225
82. Narayan V, Ramaswamy S, Menon N (2007) Long-lived giant number fluctuations in a swarming granular nematic. Science 317(5834):105–108
83. Woolverton CJ, Gustely E, Li L, Lavrentovich OD (2005) Liquid crystal effects on bacterial viability. Liq Cryst 32(4):417–423
84. Shiyanovskii SV et al (2005) Lyotropic chromonic liquid crystals for biological sensing applications. Mol Cryst Liq Cryst 434:587–598

Chapter 2
Elasticity of Lyotropic Chromonic Liquid Crystals Probed by Director Reorientation in Magnetic Field

2.1 Introduction

Soft non-covalent attraction of organic molecules in solutions often results in elongated aggregates [1–4]. Examples include "living polymers", wormlike micelles of amphiphiles, stacks of disk-like dye and drug molecules [1, 2], and nucleic acids [4]. In a broad range of concentrations and temperatures, the self-assembled polydisperse aggregates of relatively rigid flat organic molecules form nematic and columnar liquid crystal (LC) phases, generally classified as lyotropic chromonic LCs (LCLCs) [1, 2]. Since the aggregates are bound by weak van der Waals forces, their length varies strongly with concentration, temperature or ionic content, making the LCLCs very different from thermotropic LCs with molecules of covalently fixed shape and from lyotropic LCs formed by objects such as tobacco mosaic viruses [5] or polymers of fixed molecular weight [6]. An intriguing question is how this fundamental structural feature of LCLCs reflects on their elastic properties.

Despite the growing interest in LCLCs, very little is known about their elasticity. Theory and numerical simulations have reached the level at which one can describe phase diagrams of LCLCs [7, 8], but not their elastic moduli. The main challenge is in accounting for the length distribution and flexibility of aggregates. The average length of aggregates $\bar{L}$ in the nematic LCLC can be estimated (see Sect. 2.5.1), following the work of van der Schoot and Cates [9] on wormlike surfactant micelles, as a function of stacking energy E, volume fraction ϕ of the chromonic molecules, persistence length λ_p of the LCLC aggregates of diameter D, and absolute temperature T:

$$\bar{L} = L_0 \phi^{5/6} \left(\frac{\lambda_p}{D}\right)^{1/3} \exp \frac{E + \kappa\phi}{2k_B T} \tag{2.1}$$

© Springer International Publishing AG 2017

S. Zhou, *Lyotropic Chromonic Liquid Crystals*, Springer Theses,
DOI 10.1007/978-3-319-52806-9_2

where $L_0 = 2\pi^{-2/3}\sqrt{a_z D}$ is a length characterizing the size of a monomer, a_z is the period of molecular stacking along the aggregate, κ is a constant describing the enhancement of aggregation by the excluded volume effects; in the second virial approximation, $\kappa \approx 4k_BT$ [9]. Experimental characterization of elastic parameters is also challenging as it requires two types of uniformly aligned samples, with the director $\hat{\mathbf{n}}$ (average orientation of aggregates) being in plane of the cell (planar alignment) and perpendicular to it (homeotropic alignment). The elastic properties can then be determined by applying a magnetic field $\mathbf{B}$ to realign $\hat{\mathbf{n}}$ (Frederiks effect). Only planar cells were used so far. In these cells, $\mathbf{B}$ causes twist or mixed twist-bend of $\hat{\mathbf{n}}$, depending on the rate of field increase [10, 11]. Golovanov et al. [12, 13] used this effect to extract the twist constant $K_2 = 0.36\,\text{pN}$ and the bend-twist ratio $K_3/K_2 = 12.2$ for disulphoindantrone-water LCLC.

In this chapter, we take advantage of the new techniques to align LCLC in both planar and homeotropic fashion, and determine all three bulk elastic constants, in geometries where the field-induced director gradients are small and correspond to equilibrium states. We study aqueous solutions of disodium salt of 6-hydroxy-5-[(4-sulfophenyl) azo]-2-naphthalenesulfonic acid, also known as Sunset Yellow (SSY). In this LCLC, the disk-like molecules reversibly aggregate face-to-face and form elongated stacks with one molecule per cross section [14–16]. We find that the dependences of K_1, K_2, K_3 on concentration c and temperature (t, in °C) are highly unusual as compared to other classes of LCs and explain the results by the varying contour length and persistence length of self-assembled flexible polydisperse aggregates.

2.2 Samples and Experimental Set-Up

SSY was purchased from Sigma Aldrich and purified as described in Ref. [14]. The study is performed for the nematic phase at c = 29.0, 30.0, and 31.5 wt% (ϕ = 0.18, 0.19 and 0.20, respectively, see Sect. 2.5.3). The diamagnetic susceptibility measured parallel to $\hat{\mathbf{n}}$ is smaller than its orthogonal counterpart, $\Delta\chi = \chi_{\parallel} - \chi_{\perp} < 0$. We used a magnetometer with a superconducting quantum interference device and determined $\Delta\chi$ following Ref. [17] as $\Delta\chi = 3(\chi_{av} - \chi_{\perp})$, where $\chi_{av} = \frac{1}{3}\left(\chi_{\parallel} + 2\chi_{\perp}\right)$ is the average volumetric magnetic susceptibility. The LC sample, flame-sealed in a glass tube and placed in the superconducting solenoid, was heated well above the nematic-to-isotropic transition and slowly cooled down to 25 °C in presence of a 5T field. $\chi_{av}(t)$ was measured in the isotropic phase and linearly extrapolated to the nematic phase region, following Ref. [17]. At 25 °C, the magnetization was monitored for over 10 h until its value saturated, indicating an equilibrium homogeneous nematic state with $\hat{\mathbf{n}} \perp \mathbf{B}$, which allowed us

to determine $\chi_\perp$. An independent measurement of $\chi_\perp$ at 1T shows little ($\sim 1\%$) difference from the 5T data, indicating that the field-induced order is negligible, which is consistent with the data on Cotton-Mouton constant [18]. Mass densities were measured with a densitometer DE45 (Mettler Toledo). Concentration and temperature dependences of $\Delta\chi$ are presented in Sect. 2.5.2.

To determine the elastic parameters, we used flat glass cells of thickness $d = 20 - 25\,\mu m$. A relatively large d and the smallness of director gradients in the Frederiks effect help us to avoid possible changes of scalar order parameters in a strongly distorted LCLC [19]. For planar alignment, the substrates were rubbed with a superfine abrasive paper (001 K Crystal Bay™ Crocus Cloth, 3 M), washed, dried, and treated with UV ozone for 5 min to improve wettability. Homeotropic alignment of SSY was achieved with unrubbed polyimide SE-7511L (Nissan).

The cell is placed in the magnetic field and probed with two orthogonal polarized laser beams. One beam is parallel to **B**. The normal to the cell $\hat{\mathbf{z}}$ makes an angle α with **B**, $\hat{\mathbf{y}}$ is the axis of rotation, and the $\hat{\mathbf{x}}$ axis is parallel to $\hat{\mathbf{n}}$ in the planar cell (Fig. 2.1). The angle α is controlled with a precision better than 0.1°.

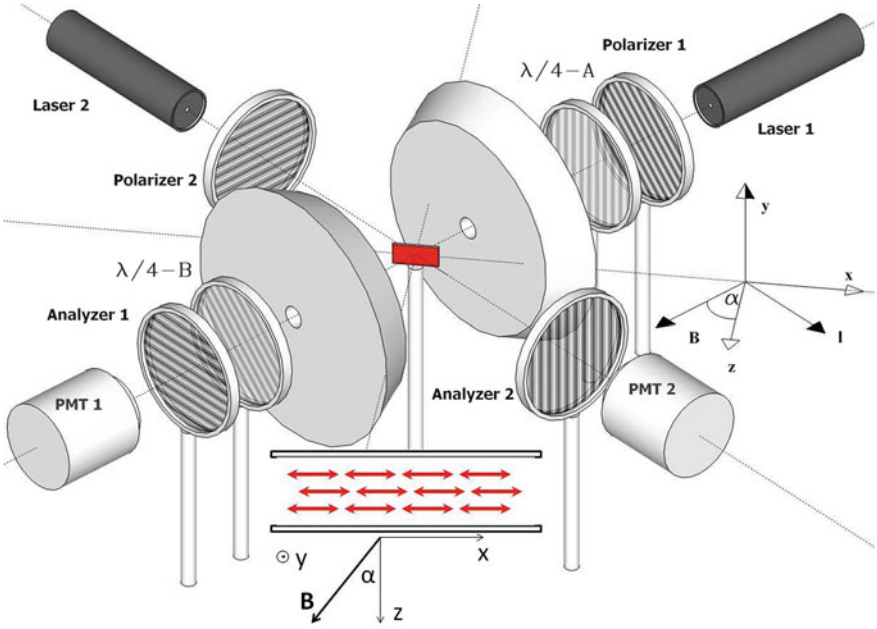

Fig. 2.1 Schematic of experiment setup. Sample is held in a hot stage for temperature control (not shown here). Both laser 1 and 2 are He–Ne lasers ($\lambda = 633\,nm$)

2.3 Results

2.3.1 Homeotropic Cells, Bend Constant K_3

K_3 is determined by setting $\alpha = 0$ and detecting the optical phase retardation for the laser beam 1, transmitted through the cell and two pairs of crossed circular polarizers (each comprising a linear polarizer and a $\lambda/4$ plate). Light transmission increases at the threshold

$$B_3 = \frac{\pi}{d}\sqrt{\frac{\mu_0 K_3}{-\Delta\chi}} \tag{2.2}$$

at which $\hat{\mathbf{n}}$ starts to tilt from the z axis (μ_0 is the magnetic permeability constant). The circular polarizers allowed us to detect the tilt regardless of its direction. To avoid the possible effect of umbilicus [20], we used beams of the expanded cross section (≈ 2 mm^2); moving the sample in the xy plane did not change the values of B_3.

In principle, Eq. (2.2) might need a correction, $d \to d + l$, where l is the so-called surface anchoring extrapolation length [21]. We verified the validity of Eq. (2.2) by measuring $B_3 = 3.5T$ in ultrathin cells ($d \approx 4\,\mu$m), using a 31 T solenoid at the National High Magnetic Field Laboratory (Tallahassee, FL). The result leads to $l = 0.15\,\mu$m, much smaller than d in the measurements of K_3, which validates Eq. (2.2).

We extracted B_3 from the hysteresis-free field dependences of transmitted light intensity obtained for a very low rate of field increments, 0.002 T/min (see Sect. 2.5.4). Repeating measurements at different points of the cell and on different cells, we established that the results were reproducible within 5%. Combining the corresponding measurement of $\Delta\chi$, we determine the temperature and concentration dependences of K_3, Fig. 2.2a.

2.3.2 Planar Cells, Splay Constant K_1

The splay Frederiks transition for $\Delta\chi < 0$ requires a planar cell placed at $\alpha = 90°$, i.e., $\mathbf{B} \parallel \hat{\mathbf{n}}$, Fig. 2.1. However, as K_2 is about an order of magnitude smaller than K_1, Fig. 2.2, twist will develop before splay. To impose splay, we aligned the cell at $\alpha = 25°$. As $\mathbf{B}$ increases from 0 to 0.33T, the director experiences threshold-less mixed splay-bend deformation. We measured the field dependence of optical retardation of the cell $R(B)$ by Senarmont technique [22]. The theoretical dependence $R(B)$ was determined by numerically calculating the profile of director tilt $\theta(z)$ (with respect to the z-axis) from the bulk equilibrium equation (see Sect. 2.5.5)

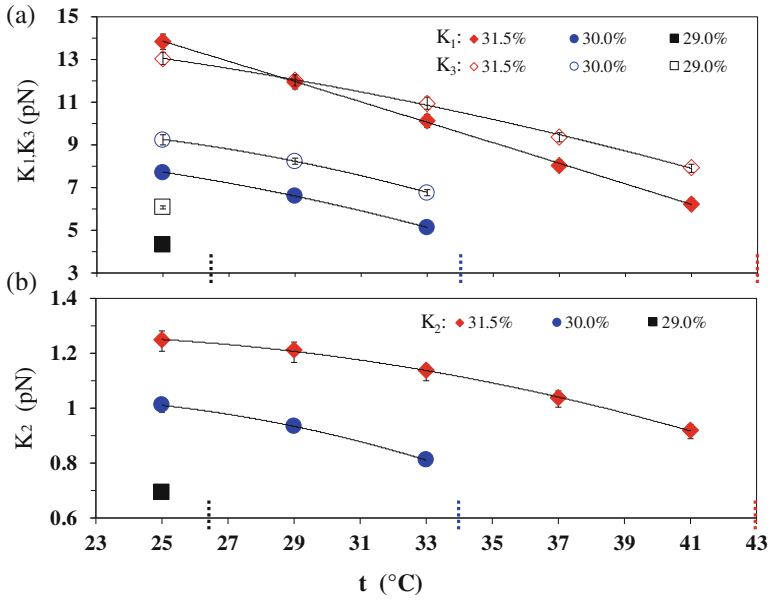

Fig. 2.2 Temperature and concentration dependences of **a** K_1, K_3 and **b** K_2. The *vertical dash lines* mark the nematic-biphasic transition temperature ($T_{N\to N+I}$) upon heating (same for other plots) for each concentration: 26.6 ± 0.6 °C, 34.4 ± 0.4 °C, 44.1 ± 0.5 °C for $c = 29$, 30.0 and 31.5% respectively

$$f = \frac{1}{2}\left(K_1 \sin^2\theta + K_3 \cos^2\theta\right)\left(\frac{d\theta}{dz}\right)^2 - \frac{1}{2}\frac{\Delta\chi}{\mu_0}B^2\cos^2(\alpha-\theta) \tag{2.3}$$

Since K_3 is already known, we fit the experimental $R(B)$ to extract K_1 as the only fitting parameter, Fig. 2.2a.

2.3.3 *Planar Cells, Twist Constant* K_2

The magnetic field applied parallel to $\hat{\mathbf{n}}$ in the geometry $\alpha = 90°$ often leads to periodic distortions instead of a uniform twist [10–12]. To avoid this regime, we use $\alpha = 75°$. The increasing field first sets up a uniform splay, followed by a uniform twist above the threshold (see Sect. 2.5.6):

$$B_2 \approx \frac{\pi}{d\sin\alpha}\sqrt{\frac{\mu_0 K_2}{-\Delta\chi}} \tag{2.4}$$

We used the laser beam 2 polarized parallel to **B**, Fig. 2.1. In the absence of twist, the propagating mode is purely extraordinary and is extinguished by the analyzer. When the field reaches B_2, the transmittance increases. Measuring B_2, we determine K_2, Fig. 2.2b. The azimuthal anchoring length was small $l_{az} \approx 0.15\,\mu\text{m}$, as determined by measuring B_2 in thin cells with $d \approx 7\,\mu\text{m}$. The optical response was hysteresis-free for the rate 0.002 T/min of field change.

For SSY concentration $c = 29.0\%$ at $t = 25$ °C, we found $K_1 = (4.3 \pm 0.4)\,\text{pN}$, $K_2 = (0.7 \pm 0.07)\,\text{pN}$, $K_3 = (6.1 \pm 0.6)\,\text{pN}$. Comparing these to 4-n-pentyl-4′-cyanobiphenyl (5CB) values [21], $K_1 = 6.6\,\text{pN}$, $K_2 = 3\,\text{pN}$, $K_3 = 10\,\text{pN}$, one sees that K_1 and K_3 are of the same order, but K_2 is much smaller than that in 5CB. The SSY data are close to those for a lyotropic polymer LC (LPLC) formed by monodisperse poly-γ-benzylglutamate (PBG) in organic solvents, with $\phi = 0.20$ and length-to-diameter ratio $L/D = 32$ [6]: $K_1 = 10\,\text{pN}$, $K_2 = 0.6\,\text{pN}$, $K_3 = 10\,\text{pN}$.

2.4 Discussion and Conclusion

The most dramatic and unusual (as compared to other types of LCs, either thermotropic or lyotropic, see, e.g., review by Singh [23]) trend observed in LCLC SSY is that the splay constant and its ratios such as $\frac{K_1}{K_3}$ and $\frac{K_1}{K_2}$ increase when c increases and t decreases, Figs. 2.2a and 2.3c, d. As already indicated, the detailed theoretical interpretation tools to describe the elasticity of LCLCs are yet to come. We first compare the observed trends to the predictions of the phenomenological Landau-de Gennes (LdG) model [24] and models developed for LPLCs [25–28].

Within the LdG model, the temperature dependences of $K_{1,2,3}$, $\Delta\chi$, and Δn are determined by that of the scalar order parameter S, namely, $K_{1,2,3} \propto S^2$, $\Delta\chi \propto S$, $\Delta n \propto S$ [24]. We measured $\Delta n(t)$ and $S(t)$, using the technique described in [29], Fig. 2.4. As seen from Fig. 2.3a, only K_2 follows the LdG behavior, with $\frac{K_2}{-\Delta\chi S}$ being practically independent of t. In contrast, $\frac{K_1}{-\Delta\chi S}$, $\frac{K_1}{K_2}$, and $\frac{K_1}{K_3}$ decrease strongly when t increases, Fig. 2.3b–d. Such a behavior is at odds not only with the LdG model, but also with the experiments for thermotropic LCs, which typically show $\frac{K_1}{K_3}$ and $\frac{K_1}{K_2}$ increasing with t [23].

In the models of LPLCs [25–28], the molecules of covalently fixed length L = const and diameter $D \ll L$ are considered either as rigid or semiflexible. If the rods are rigid, the excluded volume theory [25] predicts $K_1 \propto \phi \frac{L}{D}$, $K_1/K_3 = 3$, and $K_3 \propto \phi^3 \left(\frac{L}{D}\right)^3$, so that $\frac{K_1}{K_3} \propto \phi^{-2} \left(\frac{D}{L}\right)^2$ will be much smaller than 1 and decreasing at high ϕ. The behavior of SSY is very different, with $K_1/K_2 \approx 6 - 11$ and $K_1 \approx K_3$; importantly, K_1/K_3 increases with $\phi \propto c$, Fig. 2.3d. The disagreement remains when one considers a bidisperse system [25] or takes into account electrostatic effects [27]. The SSY aggregates are charged, as the ionizable groups at periphery dissociate in water. For the typical volume fractions of SSY in the nematic phase, $\phi \approx 0.2$, the Debye length λ_d is about 0.3 nm [16]. The electrostatic interactions

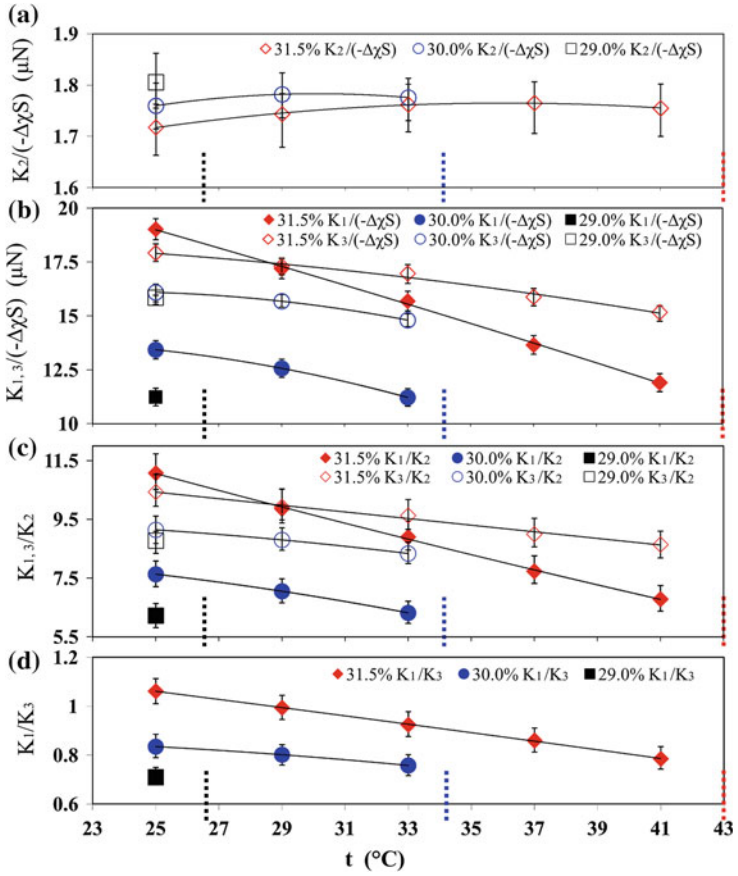

Fig. 2.3 Temperature and concentration dependences of **a** $\frac{K_2}{-\Delta\chi S}$, **b** $\frac{K_{1,3}}{-\Delta\chi S}$, **c** $\frac{K_{1,3}}{K_2}$, and **d** $\frac{K_1}{K_3}$

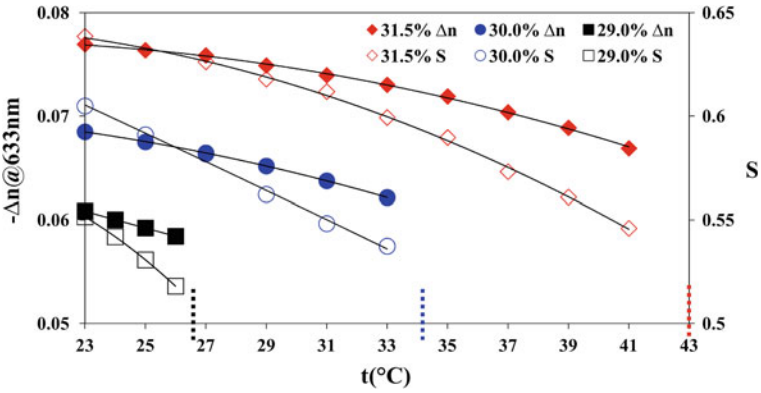

Fig. 2.4 Temperature and concentration dependences of Δn (at 633 nm) and scalar order parameter $\mathfrak{S}$

lead to a "twisting effect", as two similarly charged aggregates tend to align perpendicularly to each other. The effect decreases K_2 by a small factor $\approx (1-0.1h)$ [27], where $h=\lambda_d/(D+2\lambda_d)$ is only about 0.2 for the nematic phase of SSY [16]. In LPLCs, the electrostatic effect might also increase K_3 [27] (thus making K_1/K_3 even smaller than in the model of non-charged rods), since the mutual repulsion of similar charges along the polymer makes it stiffer. We conclude that the elasticity of SSY cannot be described by the model of rigid rods of fixed length, whether charged or not, and turn to the models of semiflexible LPLCs [25–28].

The SSY aggregates should be flexible, as the attraction between monomers is weak, with the scission energy E in the range $(7-11)k_BT$ [14, 16, 30]. In the theory of semiflexible LPLCs, K_2 and K_3 are determined by the persistence length λ_p of the polymers rather than by L [25, 26, 28]: $K_2=\frac{k_BT}{D}\phi^{1/3}\left(\frac{\lambda_p}{D}\right)^{1/3}$ [25]; $K_3=\frac{4}{\pi}\frac{k_BT}{D}\phi\frac{\lambda_p}{D}$ (we use the standard definition [31] $\lambda_p=B/k_BT$ through the bend modulus B, which makes K_3 twice as large as in Ref. [28]). The last formula, with the experimental $K_3=6\,\mathrm{pN}$ at $\phi=0.18$, $t=25\,^{\circ}\mathrm{C}$ and D = 1.1 nm [14, 16], yields $\lambda_p\approx 10$ nm. We are not aware of any other estimates of λ_p for LCLC, but the result appears reasonable when compared to $\lambda_p\approx 50$ nm for DNA duplex [31], as the latter is about twice wider than the SSY aggregate and we expect λ_p to increase with D.

The splay modulus K_1 still grows with the contour length L (as opposed to the persistence length λ_p) in flexible LPLCs: as explained by Meyer [3], splay deformations, under the condition of constant density, limit the freedom of molecular ends, which increases the entropy. A larger L implies a smaller number of molecular ends available to accommodate for splay and thus a higher K_1: $K_1=\frac{4}{\pi}\frac{k_BT}{D}\phi\frac{L}{D}$ [28].

The model of semiflexible LCLC aggregates, supplemented by the idea that their *average* length $\bar{L}$ in LCLCs is not fixed [1–3, 9], Eq. (2.1), explains the observed T and ϕ dependences of elastic ratios, expressed as:

$$\frac{K_1}{K_3}=\frac{\bar{L}}{\lambda_p},\quad \frac{K_1}{K_2}=\frac{4}{\pi}\phi^{2/3}\frac{\bar{L}}{\lambda_p^{1/3}D^{2/3}},\quad \frac{K_3}{K_2}=\frac{4}{\pi}\phi^{2/3}\left(\frac{\lambda_p}{D}\right)^{2/3}.$$

The dramatic decrease of $\bar{L}(\phi,t)\propto\exp(E/2k_BT)$ at elevated temperatures is expected to cause the strongest T-dependence of the splay constant K_1. The persistent length is determined mainly by E and should be only a weak function of T and ϕ. Numerical simulations [7] show that $\lambda_p\propto 5+2.14E/k_BT$ for chromonic aggregates. Using this empirical result and Eq. (2.1), we estimate the trends as:

$$\frac{K_1}{K_3}\propto\phi^{5/6}\frac{\exp[(E+\kappa\phi)/2k_BT]}{(E/k_BT)^{2/3}},$$

$$\frac{K_1}{K_2} \propto \phi^{3/2} \exp[(E + \kappa\phi)/2k_BT],$$

and

$$\frac{K_3}{K_2} \propto \phi^{2/3} (E/k_BT)^{2/3}.$$

All three ratios increase when T decreases and ϕ increases, as in the experiment, Fig. 2.3c, d. The ratio K_1/K_2 is the most sensitive to ϕ and T, in a good agreement with Fig. 2.3c. The strong increase of K_1/K_2 explains the effect of spontaneous chiral symmetry breaking in osmotically condensed LCLC tactoids [32]. The estimate $K_1/K_3 = \bar{L}/\lambda_p$ combined with the experimental fact that $K_1/K_3 = 1.1 - 0.7$, Fig. 2.3d, implies that $\bar{L}$ and λ_p are of the same order and that $\bar{L}/\lambda_p$ decreases at high temperatures, where the aggregates shorten while SSY approaches the isotropic phase. From the tilt of temperature dependencies, $\frac{K_3}{K_1}\frac{d(K_1/K_3)}{dT}$ and $\frac{K_2}{K_1}\frac{d(K_1/K_2)}{dT}$, we deduce $E \approx 10k_BT$ and $13k_BT$, respectively (for $\kappa = 4k_BT$ [9]).

To conclude, we measured the temperature and concentration dependences of Frank moduli of the self-assembled nematic LCLC. K_1 and K_3 are found to be comparable to each other and to the corresponding values in thermotropic LCs, while K_2 is one order of magnitude smaller. The splay constant K_1 and the elastic ratios $\frac{K_1}{K_3}$, $\frac{K_1}{K_2}$ increase significantly when the concentration of SSY increases or the temperature decreases. This unusual behavior is explained within a model of semiflexible SSY aggregates, the average length of which increases with concentration and decreases with temperature, a feature that is absent in conventional thermotropic and lyotropic LCs formed by units of fixed length.

2.5 Supplemental Information

2.5.1 Estimation of Average Aggregation Length

Van der Schoot and Cates [9] described the isotropic-to-nematic transition in the solution of semiflexible polydisperse micelles of spherocylindrical shape formed by surfactant molecules. The polar heads of the rod-like surfactant molecules are located at the interface with water while the hydrophobic hydrocarbon tails are hidden in the interior of the micelles. The theory [9] operated with the volume fraction of surfactant molecules ϕ (related to the numerical density of surfactant molecules v as $\phi = \pi v D^3/6m$, where D is the micelle diameter and m is the minimum aggregation number equal the number of surfactant molecules that reside in the semispherical caps at the two ends of the cylindrical body of the micelles), scission energy E (required to create two new ends of the micelle), persistence

length λ_p, numerical constant κ close to $4k_BT$ and the growth parameter $\bar{\alpha}$ found to be $\bar{\alpha}^{3/2} = \frac{8\lambda_p}{\sqrt{\pi}D}\phi$. In these notations, the aggregation number is

$$\bar{n} = \frac{\sqrt{\bar{\alpha}v}}{2} D^{3/2} \exp\frac{E + \kappa\phi}{2k_BT} \tag{2.5}$$

One can apply this expression to describe the average length $\bar{L}$ of the LCLC aggregates, by noticing that in the latter case, $\bar{L} = \bar{n}a_z$, where a_z is a repeat distance of stacking along the aggregate axis (the "thickness" of the chromonic molecule, typically equal 0.34 nm) and that $vD^3 = \frac{4\phi D}{\pi a_z}$ rather than $vD^3 = 6\phi m/\pi$ as in Ref. [9]. The result is

$$\bar{L} = \frac{2}{\pi^{2/3}} \sqrt{Da_z}\phi^{5/6} \left(\frac{\lambda_p}{D}\right)^{1/3} \exp\frac{E + \kappa\phi}{2k_BT} \tag{2.6}$$

which is rewritten as Eq. (2.1) in the beginning of this chapter.

2.5.2 *Measurement of Diamagnetic Anisotropy* $\Delta\chi$

We used a superconducting quantum interference device to determine the mass diamagnetic susceptibility of the sample as described in Ref. [33]. The LC sample, flame-sealed in a glass NMR tube (2 cm length, 5 mm outer diameter), was placed in the center of a superconducting solenoid soaked in a liquid He bath. The solenoid provided a uniform magnetic field up to 5T. The magnetization was determined by moving the sample up and down by a step motor and measuring the magnetization signal as a function of z coordinate using three sets of coils. The temperature of the sample space was controlled by heating wires on the outside shield and by a cooling stream of He gas with a low pressure of 800 Pa taken from the liquid He bath.

In the sample space, the glass tube with SSY was heated to $67 - 83\,^{\circ}\mathrm{C}$ (well above nematic-biphasic transition for c = 29–31.5%) and slowly cooled down to the nematic phase at 25 °C with 5T field applied. At 25 °C, a strong field aligns $\hat{\mathbf{n}} \perp \mathbf{B}$, thus we measured $\chi_\perp$ after monitoring the magnetization for over 10 h until its value saturated, indicating an equilibrium state of a homogeneous nematic phase. At high temperatures well above nematic-biphasic transition, the measurements of magnetization yield $\chi_{iso}(t)$ as a function of temperature, for example (67–47) °C for 29%. Following Stefanov and Saupe [17], we extrapolate the measured $\chi_{iso}(t)$ to $t = 25$ °C to find $\chi_{av} = \left(\chi_\parallel + 2\chi_\perp\right)/3$. Using the measured $\chi_\perp$ and extrapolated χ_{av}, we calculated $\Delta\chi = 3(\chi_{av} - \chi_\perp)$ [17], Fig. 2.5. An independent measurement of $\Delta\chi$ done under 1T field gave only a small difference of 1%, indicating that the

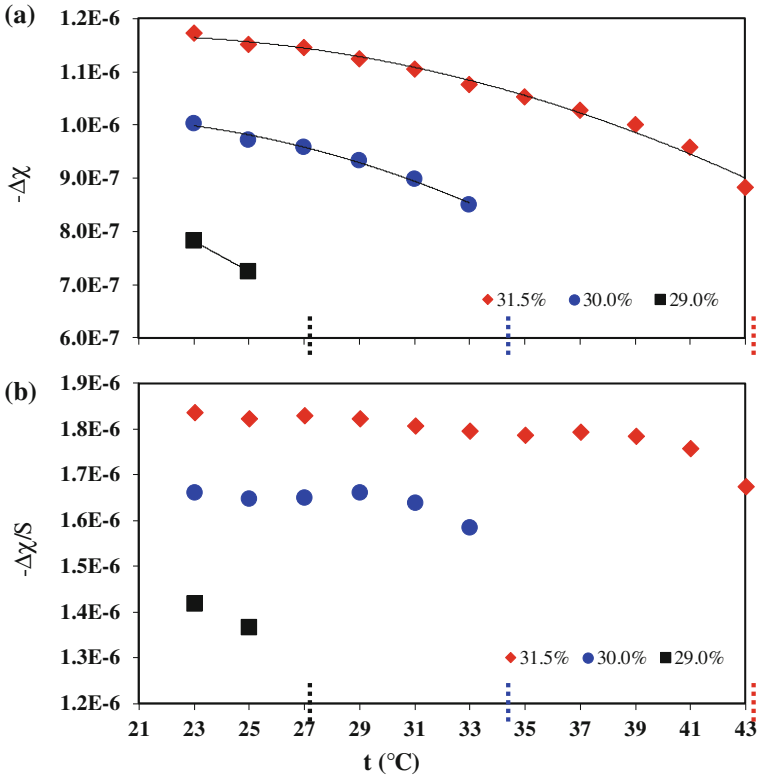

Fig. 2.5 Temperature and concentration dependences of **a** $\Delta\chi$ and **b** $\Delta\chi/S$ of SSY. Note that $\Delta\chi/S$ remains practically constant when temperature is more than $2-3$ °C below $T_{N\to N+1}$ for each concentration. In the vicinity of $T_{N\to N+1}$, $\Delta\chi$ deviates from $\Delta\chi \propto S$ behavior, likely due to pretransitional effects [34]. We estimate the accuracy of $\Delta\chi$ measurements to be $\pm 10\%$

magnetic field induced changes in the degree of orientational order are negligible, in agreement with the Luoma's data on the Cotton-Mouton constant [18].

The measurement errors are caused by several factors. First of all, the system was designed for samples of sub-millimeter size, much smaller than the motor scan range 4–6 cm. Our samples are longer, representing a 1 cm long SSY volume confined in a glass NMR tube. Second, the sample motion noise caused by the step motor limits the accuracy of sample positioning [33]. To estimate the possible errors introduced by these factors and the validity of the Stefanov-Saupe method, we measured the diamagnetic anisotropy of a standard thermotropic nematic material 4-n-pentyl-4′-cyanobiphenyl (5CB) (by extrapolating χ_{iso} to obtain χ_{av} and measuring directly $\chi_{\|}$) and found it to be about 10% lower than the value reported previously [33]. We thus estimate the accuracy of our measurements as $\pm 10\%$.

2.5.3 Measurements of Density ρ and Volume Fraction ϕ

In previous studies [14, 16], volume fraction of SSY was calculated by taking the SSY mass density $\rho_{SSY} = 1.4 \times 10^3\,\mathrm{kgm}^{-3}$ from Ref. [14] and assuming both volume and mass are additive quantities, as if water is a continuous medium and ρ_{SSY} is the mass density of individual aggregate. However, the second assumption is not needed if one knows the density of SSY solutions. We used a densitometer DE45 (Mettler Toledo) to measure the density of SSY solutions directly (Fig. 2.6) and with the obtained data determined volume fraction ϕ. As water molecules (typically 0.15 nm) are much smaller than SSY aggregates ($\sim$1.1 nm diameter, $\sim$7 nm length [14, 16]), we approximate water as a continuous medium. Given the weight concentration of SSY c, one can calculate the volume fraction of water ϕ_w :

$$\phi_w = \frac{(1-c)/\rho_w}{1/\rho_{sol}} = (1-c)\frac{\rho_{sol}}{\rho_w} \tag{2.7}$$

where ρ_w and ρ_{sol} are the densities of water and solution, respectively. $\phi_{SSY} = 1 - \phi_w$ is shown in Fig. 2.6.

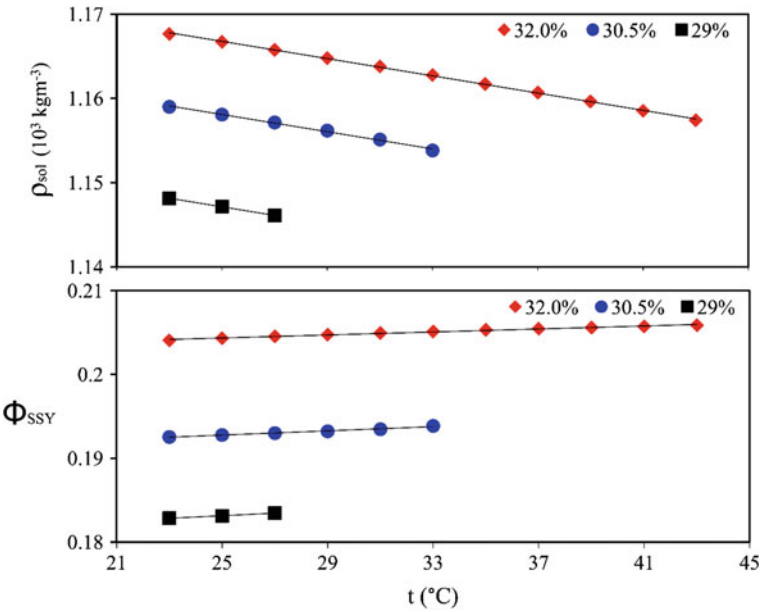

Fig. 2.6 Mass density measurements and calculated volume fraction

We can also calculate the effective mass density of SSY in the solution by:

$$\rho_{SSY} = \frac{c}{\frac{1}{\rho_{sol}}\phi_{SSY}} \tag{2.8}$$

which yields $\rho_{SSY} = (1.82 \pm 0.02) \times 10^3 \text{kgm}^{-3}$, significantly different from the value of $\rho_{SSY} = 1.4 \times 10^3 \text{kgm}^{-3}$ presented in Ref. [18]. If one takes the typical parameters of SSY aggregates, the outer diameter D = 1.1 nm, repeating distance a_z = 0.34 nm, and molar mass $M_{SSY} = 0.452 \text{kgmol}^{-1}$, one estimates the mass density for individual aggregates as $\rho_{SSY} = \frac{4M_{SSY}/N_A}{\pi D^2 a_z} = 2.32 \times 10^3 \text{kgm}^{-3}$ (N_A is the Avogadro's number), different from $\rho_{SSY} = (1.82 \pm 0.02) \times 10^3 \text{kgm}^{-3}$ calculated from Eq. (2.8). This difference might result from an inaccurate estimation of the aggregates size (e.g., $\rho_{SSY} \propto D^{-2}$ and D varies from 1.1 to 1.4 nm in literatures [14, 16, 18]), and from the assumption that water is a continuous medium.

2.5.4 Optical Response in Bend Frederiks Transition

To determine K_3, we measure the intensity of light passing through the homeotropic cell and two circular polarizers; this intensity depends on optical phase retardation $R(B)$ associated with the field-induced director distortions:

$$I = I_0 \sin^2 \frac{R}{2} \tag{2.9}$$

where I_0 is the intensity of the incident light. When the field was changed at a very slow rate (0.002 T/min, or 200 s pauses between 0.0065 T increments), the $I(B)$

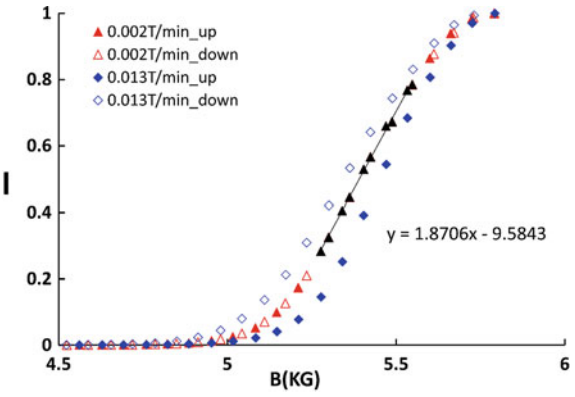

Fig. 2.7 Intensity versus $\mathfrak{B}$ for bend deformation. *Inset* equation is the fitting from linear part (black triangles) of the curve

curve shows no hysteresis, Fig. 2.7. Higher rates might cause hysteresis; as an example, we show a hysteresis observed for 0.013 T/min (30 s pauses between 0.0065 T increments), Fig. 2.7. From the linear part of the $I(B)$ curve, we found the critical field intensity B_3.

2.5.5 *Optical Simulation to Determine Splay Constant* K_1

When the LC is distorted by the magnetic field $\mathfrak{B}$, the free energy density in the general form writes [24]:

$$f = \frac{1}{2}K_1(\nabla\hat{\mathbf{n}})^2 + \frac{1}{2}K_2(\hat{\mathbf{n}}\cdot\nabla\times\hat{\mathbf{n}})^2 + \frac{1}{2}K_3(\hat{\mathbf{n}}\times\nabla\times\hat{\mathbf{n}})^2 - \frac{1}{2}\frac{\Delta\chi}{\mu_0}(\hat{\mathbf{n}}\cdot\mathbf{B})^2 \quad (2.10)$$

In our cases, the deformation is always uniform in the xy plane parallel to the cell, thus we express the director $\hat{\mathbf{n}}$ as a function of the normal $\mathfrak{Z}$ coordinate only: $\hat{\mathbf{n}}(z) = (n_x, n_y, n_z) = (\sin\theta\cos\varphi, \sin\theta\sin\varphi, \cos\theta)$, where $\theta(z)$ is the polar angle with respect to $\hat{z}$, and $\varphi(z)$ the azimuthal angle with respect to $\hat{x}$ (the easy axis of the planar cell). For $\mathbf{B} = B(\sin\alpha, 0, \cos\alpha)$, as shown in Fig. 2.1 in Sect. 2.2, Eq. (2.10) becomes:

$$f = \frac{1}{2}\left(K_1\sin^2\theta + K_3\cos^2\theta\right)^2\left(\frac{d\theta}{dz}\right)^2 + \frac{1}{2}\left(K_2\sin^2\theta + K_3\cos^2\theta\right)^2\sin^2\theta\left(\frac{d\varphi}{dz}\right)^2 - \frac{1}{2}\frac{\Delta\chi}{\mu_0}B^2(\cos\alpha\cos\theta + \sin\alpha\sin\theta\cos\varphi)^2 \quad (2.11)$$

In K_1 experiment, the boundary conditions at the two surfaces are $\theta(0) = \theta(d) = 90°$. A relatively small 0.3T field applied at $\alpha = 25°$ induces a weak deformation in the bulk. In the mid-plane, for 0.3 T field, director orientation changes from $\theta(d/2) = 90°$ to $\theta(d/2) = 80°$ but $\varphi(z)$ remains 0, as follows from the numerical minimization of the energy Eq. (2.11) for $\varphi(z) = 0$ simplifies to Eq. (2.3).

As $\cos^2 80° \approx 0.03$, the main contribution to the elastic energy is from the splay term. Solving the Euler-Lagrange equation,

$$\frac{\partial f}{\partial\theta} - \frac{d}{dz}\left(\frac{\partial f}{\partial\theta'}\right) = 0 \quad (2.12)$$

where $\theta' = \frac{d\theta}{dz}$, we find the $\theta(z)$ profile as a function of B and can calculate the optical retardation and light transmission, as explained below.

With $\theta(z, B)$ obtained from Eq. (2.12), one can calculate the effective extraordinary refractive index $n_{eff}(z, B)$ in the cell:

$$n_{eff}(z, B) = \frac{n_e n_o}{\sqrt{n_e^2 \cos^2(\beta - \theta(z, B)) + n_o^2 \sin^2(\beta - \theta(z, B))}} \tag{2.13}$$

where n_e and n_o are the extraordinary and ordinary refractive indices, respectively; we also take into account that the light propagation direction $\hat{\mathbf{k}}$ within the LC, characterized by the polar angle β measured with respect to $\hat{z}$, is different from **B** direction (polar angle α), because of refraction at interfaces. Since the birefringence of the LCLC is low, we use an average refractive index $n_{av} = 1.4$ to calculate $\beta = \sin^{-1}\left(\frac{\sin\alpha}{n_{av}}\right)$.

Integration over the cell thickness gives the total phase retardation of the splayed director field [22]:

$$R(B) = \frac{2\pi}{\lambda \cos\beta} \int_0^d \left(n_{eff}(z, B) - n_o\right) dz \tag{2.14}$$

Using this equation to fit the experimental data of $R(B)$ with an independently measured $\frac{K_3}{\Delta\chi}$, we obtain $\frac{K_1}{\Delta\chi}$, as shown in Fig. 2.8.

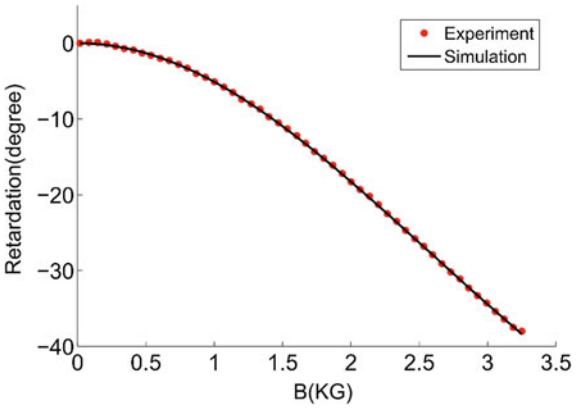

Fig. 2.8 Experimental measurement and numerical simulation of $R(B)$ which result in $\frac{K_1}{-\Delta\chi} = 13.2\,\mu\text{N}$ for a cell of 31.5% SSY with $\Delta n = -0.0768$ for λ = 633 nm at 25 °C

2.5.6 *Planar Cells, Twist Constant* K_2

Transient periodic patterns in twist geometry of Frederiks transition have been observed since 1980's [10], including the case of LCLCs [11]. We observed the same phenomenon in SSY. When **B** is applied at $\alpha = 90°$ direction, it causes "bamboo" patterns, Fig. 2.9, similar to that presented in Ref. [11] . As pointed in Ref. [11], the periodic patterns does not appear when **B** is tilted away from $\hat{\mathbf{n}}_0$ direction. In our experiments, we used a 15° tilt away from $\hat{\mathbf{n}}_0$ to avoid non-uniform twist, $\alpha = 75°$.

When **B** is applied at $\alpha = 75°$, the numerical simulations of the director field show that first a weak splay develops, with a small (<3°) deviation from the original orientation. Above some threshold B_2, a uniform twist develops, Fig. 2.10. Experimentally, B_2 can be determined from the $I(B)$ curves, similar to the K_3 case described above. The value can also be determined theoretically; analysis below shows that the threshold is determined mainly by the tilt angle α and by the constant $\frac{K_2}{\Delta\chi}$, and that the correction caused by splay is small ($\approx 1\%$).

As the splay is weak, we present the polar angle as a sinusoidal function of z, i.e. $\theta(z) = \frac{\pi}{2} + \delta \sin\left(\frac{\pi}{d} z\right)$, where δ is the maximum polar angle change that occurs in the middle plane of the cell. For fixed boundary condition (strong anchoring), $\theta(0) = \theta(d) = \pi/2$. For the twisted state near the threshold, we write

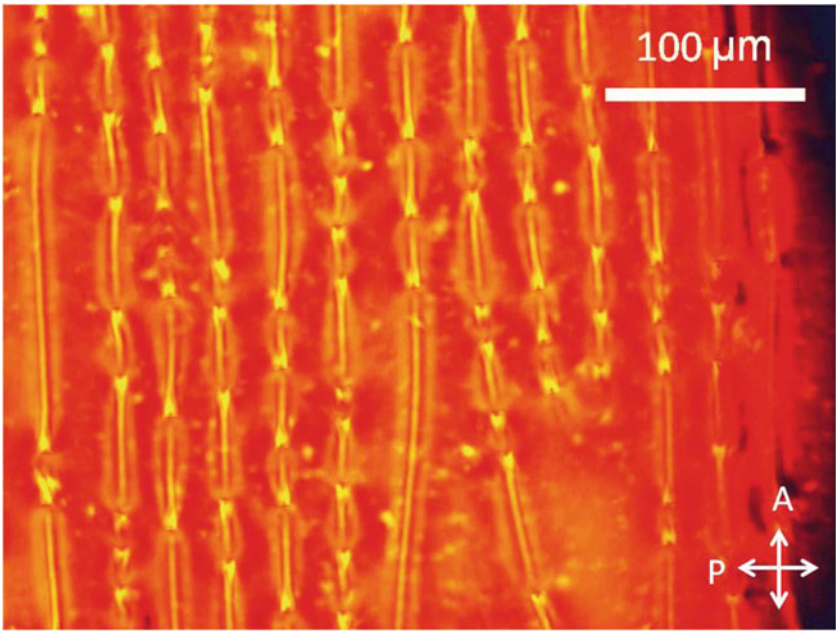

Fig. 2.9 Periodic pattern in a planar SSY cell induced after abruptly applying a magnetic field of 0.4 T at $\alpha = 90°$

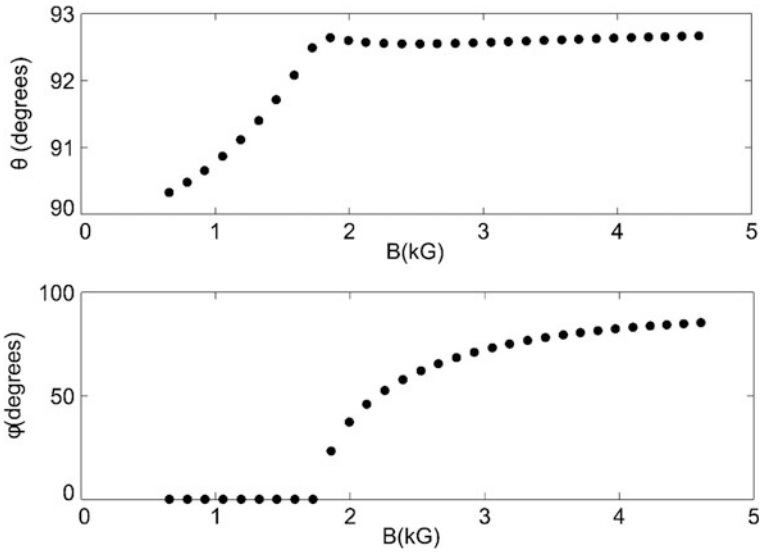

Fig. 2.10 Numerically simulated dependencies $\theta(d/2)$ and $\varphi(d/2)$ versus B representing maximum deformations in the mid-plane of cell, for a cell with $d = 23.8\,\mu m$, $\frac{K_2}{-\Delta\chi} = 1.22\,\mu N$, $\frac{K_1}{-\Delta\chi} = \frac{K_3}{-\Delta\chi} = 9.8\,\mu N$

$\varphi(z) = 0 + \gamma(z) = \varphi_m \sin\left(\frac{\pi}{d}z\right)$, ($\varphi(0) = \varphi(d) = 0$ fixed at two boundaries). If the twisted state is preferred as compared to pure splay, then the following integral should be negative:

$$J = \int_0^d \left(\frac{\partial f}{\partial \varphi}\gamma + \frac{\partial f}{\partial \varphi'}\gamma'\right) dz < 0 \tag{2.15}$$

where $\varphi' = \frac{d\varphi}{dz}$, $\gamma' = \frac{d\gamma}{dz}$. Using Eq. (2.11) and $\theta(z)$, $\varphi(z)$ specified above, we find (up to the first order in δ):

$$J \approx \varphi_m^2 \frac{d}{2}\left[\frac{\Delta\chi}{\mu_0}B^2\left(\sin^2\alpha - \frac{8}{3\pi}\delta\sin\alpha\cos\alpha\right) + \left(\frac{\pi}{d}\right)^2 K_2\right] < 0 \tag{2.16}$$

Thus,

$$B_2 = \frac{\pi}{d\sin\alpha}\sqrt{\frac{\mu_0 K_2}{-\Delta\chi\left(1 - \frac{8}{3\pi}\delta\cot\alpha\right)}} \tag{2.17}$$

With $\delta = 3^\circ$, one finds $\frac{8}{3\pi}\delta \cot\alpha \approx 0.01$, thus we conclude that the spay correction to the B_2 value is negligible, and use the simplified equation,

$$B_2 = \frac{\pi}{d \sin\alpha}\sqrt{\frac{\mu_0 K_2}{-\Delta\chi}} \tag{2.18}$$

to determine $\frac{K_2}{\Delta\chi}$, as indicated in Sect. 2.3.3.

References

1. Lydon J (2011) Chromonic liquid crystalline phases. Liq Cryst 38(11–12):1663–1681
2. Dickinson AJ, LaRacuente ND, McKitterick CB, Collings PJ (2009) Aggregate structure and free energy changes in chromonic liquid crystals. Mol Cryst Liq Cryst 509:751–762
3. Meyer RB (1982) Polymer liquid crystals, In: Ciferri A, Krigbaum WR, Meyer RB (ed) Academic Press, New York
4. Nakata M et al (2007) End-to-end stacking and liquid crystal condensation of 6-to 20-base pair DNA duplexes. Science 318(5854):1276–1279
5. Dogic Z, Fraden S (2006) Ordered phases of filamentous viruses. Curr Opin Colloid Interface Sci 11(1):47–55
6. Lee S-D, Meyer RB (1988) Crossover behavior of the elastic coefficients and viscosities of a polymer nematic liquid crystal. Phys Rev Lett 61:2217
7. Kuriabova T, Betterton MD, Glaser MA (2010) Linear aggregation and liquid-crystalline order: comparison of Monte Carlo simulation and analytic theory. J Mater Chem 20:10366
8. Chami F, Wilson MR (2010) Molecular order in a chromonic liquid crystal: a molecular simulation study of the anionic azo dye sunset yellow. J Am Chem Soc 132(22):7794–7802
9. der Schoot PV, Cates ME (1994) The isotropic-to-nematic transition in semi-flexible micellar solutions. Europhys Lett 25:515
10. Lonberg F, Fraden S, Hurd AJ, Meyer RE (1984) Field-induced transient periodic structures in nematic liquid crystals: the Twist-Freedericksz transition. Phys Rev Lett 52(21):1903–1906
11. Hui YW, Kuzma MR, San Miguel M, Labes MM (1985) Periodic structures induced by director reorientation in the lyotropic nematic phase of disodium cromoglycate–water. J Chem Phys 83(1):288–292
12. Golovanov AV, Kaznacheev AV, Sonin AS (1995) Izvestiya Akad. Nauk, Ser. Fiz. 59:82
13. Golovanov AV, Kaznacheev AV, Sonin AS (1996) Izvestiya Akad. Nauk, Ser. Fiz. 60:43
14. Horowitz VR, Janowitz LA, Modic AL, Heiney PA, CP J (2005) Aggregation behavior and chromonic liquid crystal properties of an anionic monoazo dye. Phys Rev E 72:041710
15. Edwards DJ et al (2008) Chromonic liquid crystal formation by edicol sunset yellow†. J Phys Chem B 112(46):14628–14636
16. Park HS et al (2008) Self-assembly of lyotropic chromonic liquid crystal sunset yellow and effects of ionic additives. J Phys Chem B 112(51):16307–16319
17. Stefanov M, Saupe A (1984) Density and susceptibility measurements on a micellar nematic system. Mol Cryst Liq Cryst 108(3–4):309–316
18. Luoma RJ (1995) X-ray scattering and magnetic birefringence studies of aqueous solutions of chromonic molecular aggregates. Ph.D. Thesis, Brandeis Unversity, Waltham, MA, USA
19. Nazarenko VG et al (2010) Surface alignment and anchoring transitions in nematic lyotropic chromonic liquid crystal. Phys Rev Lett 105(1):017801
20. Gu MX, Smalyukh II, Lavrentovich OD (2006) Directed vertical alignment liquid crystal display with fast switching. Appl Phys Lett 88(6)

21. Kleman M, Lavrentovich OD (2003) Soft matter physics: an introduction, Springer, New York, p 638
22. Nych A et al (2002) Measurement of the twist elastic constant by phase retardation technique. Mol Cryst Liq Cryst 384(1):77–83
23. Shri S (1996) Curvature elasticity in liquid crystals. Phys Rep 277(5–6):283–384
24. de Gennes PG, Prost J (1993) The physics of liquid crystals, Clarendon Press, Oxford, p 598
25. Odijk T (1986) Elastic constants of nematic solutions of rod-like and semi-flexible polymers. Liq Cryst 1:553–559
26. Grosberg AY, Zhestkov AV (1986) Polymer Sci USSR 28:97
27. Vroege GJ, Odijk T (1987) Elastic moduli of a nematic liquid–crystalline solution of polyelectrolytes. J Chem Phys 87(7):4223
28. Taratuta VG, Lonberg F, Meyer RB (1988) Anisotropic mechanical properties of a polymer nematic liquid crystal. Phys Rev A 37:1831
29. Nastishin YA et al (2005) Optical characterization of the nematic lyotropic chromonic liquid crystals: Light absorption, birefringence, and scalar order parameter. Phys Rev E 72(4):041711
30. Renshaw MP, Day IJ (2010) NMR characterization of the aggregation state of the Azo Dye sunset yellow in the isotropic phase. J Phys Chem B 114(31):10032–10038
31. Kornyshev AA, Lee DJ, Leikin S, Wynveen A (2007) Structure and interactions of biological helices *Rev*. Mod Phys 79:943
32. Tortora L, Lavrentovich OD (2011) Chiral symmetry breaking by spatial confinement in tactoidal droplets of lyotropic chromonic liquid crystals. Proc Natl Acad Sci USA 108 (13):5163–5168
33. Frisken BJ, Carolan JF, Palffy-Muhoray P, Perenboom JAAJ, Bates GS (1986) SQUID Susceptibility measurements of 5CB. Mol Cryst Liq Cryst Lett 3:57–62
34. Nastishin YA et al (2004) Pretransitional fluctuations in the isotropic phase of a lyotropic chromonic liquid crystal. Phys Rev E 70(5):051706

Chapter 3
Ionic-Content Dependence of Viscoelasticity of the Lyotropic Chromonic Liquid Crystal Sunset Yellow

3.1 Introduction

Self-assembly of organic molecules in water is central to functioning of biological systems and to a broadening range of modern technologies utilizing soft matter. The mechanisms driving a diverse spectrum of self-organized structures are complex and involve a delicate balance of dispersive, hydrophobic/hydrophilic, depletion, and electrostatic forces. To understand these mechanisms, it is important to design model systems in which the structural and mechanical features can be experimentally measured in a reliable way and connected to the underlying composition. In this work, we explore the lyotropic chromonic liquid crystals (LCLCs) as such a system that allows one to deduce the effect of ionic content on viscoelastic properties of orientationally ordered assemblies of organic molecules in aqueous solutions.

Presence of ionizable groups at the surface of chromonic aggregates makes the LCLCs very sensitive to the ionic environment in the solution, evidenced by the shifts in phase diagrams [1–4], Fig. 3.1c. Similar effects of ionic content on biomolecules are of prime importance in biological processes such as DNA wrapping around nucleosomes, packing inside bacteriophage capsids, and binding to proteins and so on [5, 6]. In this work, we quantify the effect of ionic content on the anisotropic elastic and viscous properties of the nematic LCLCs. The advantage of using the nematic LCLC in exploring the role of electrostatics is that the anisotropic viscoelastic parameters are well defined and can be accurately measured through the macroscopic deformations caused by the realigning action of an applied magnetic field (the so-called Frederiks effect) [7]. Using this technique, we measure the elastic constants of splay, bend and twist and the rotational viscosity. These

© Springer International Publishing AG 2017

S. Zhou, *Lyotropic Chromonic Liquid Crystals*, Springer Theses,
DOI 10.1007/978-3-319-52806-9_3

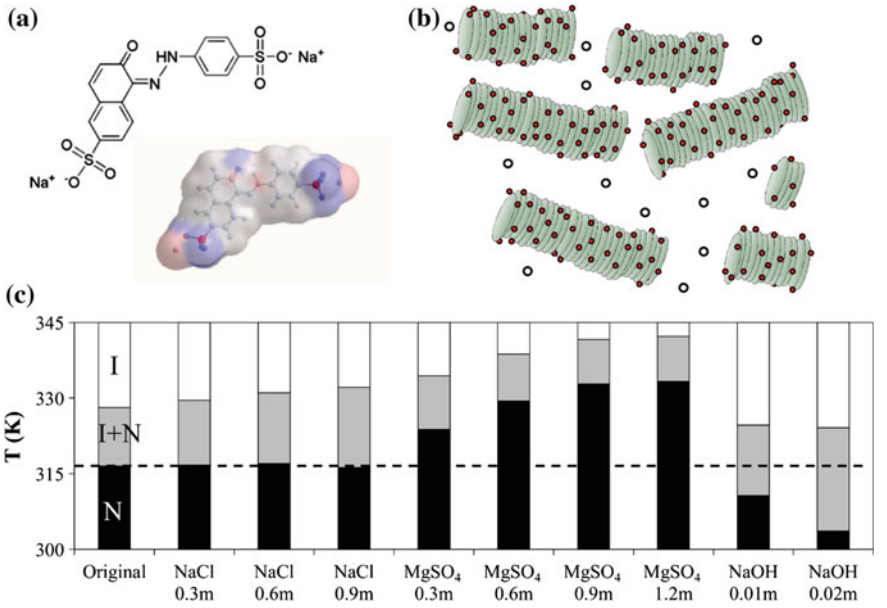

Fig. 3.1 Molecular structure (**a**), schematic of nematic LCLC phase (**b**), and phase diagram (**c**) of SSY aqueous solution with ionic additives. **a** The prevailing NH Hydroazone tautomer form is shown. **b** *Red dotes* on aggregates surface represent sulfonate groups, while isolated circles represent disassociated Na^+ ions. **c** *Dash line* marks the nematic to nematic-isotropic phase transition temperature $T_{N\to N+I} = 316.5\,\mathrm{K}$ of the original SSY LCLC

viscoelastic parameters have different and often very pronounced responses to the added monovalent and divalent salts and to pH changing agents. The observed dependencies of the viscoelastic parameters are discussed in terms of changes of the chromonic aggregates, namely, their contour and persistence lengths.

3.2 Materials and Methods

The aqueous solution of SSY is probably the simplest LCLC in terms of aggregate organization [8, 9]. The molecules, Fig. 3.1a, have two ionizable sulfonate groups at the periphery. When in water, they stack on top of each other, forming aggregates with only one molecule in its cross-section [9, 10], Fig. 3.1b. The diameter of aggregates is $D \approx 1.1$ nm, while the typical molecular separation along the axis is $a_z \approx 0.34$ nm [2, 10]. The maximum linear charge density along the aggregates is $\tau^{\max} e \approx 6e$/nm, similar to double-strand DNA (ds-DNA) molecules, where $\tau^{\max}$ is the maximum degree of ionization of the surface groups. Unlike ds-DNA, the length of SSY aggregates is not covalently fixed, a feature that makes the effect of ionic content on the length of chromonic aggregates very profound.

To vary the ionic content of the dispersions, we use a monovalent salt NaCl, divalent salt $MgSO_4$, and the pH-increasing agent NaOH. The volume fraction of SSY in all solutions remains practically constant, $\phi \approx 0.2$ [7] (see Sect. 3.5.2). The phase diagrams of the SSY dispersion with different additives is shown in Fig. 3.1c. The elastic constants of splay (K_1), twist (K_2) and bend (K_3) as well as the rotation viscosity γ_1 were measured as a function of temperature and additive concentration using the magnetic field realignment technique, as described in Ref. [7], Chap. 2 and in Sect. 3.5.5.

3.2.1 LCLC SSY with Ionic Additives

The disodium salt of 6-hydroxy-5-[(4-sulfophenyl)azo]-2-naphthalenesulfonic acid, a widely used food dye generally known as sunset yellow (SSY) was purchased from Sigma-Aldrich (90% purity) and purified twice following previously established procedures [2, 10, 11]. Deionized water (resistivity >18.1 MΩ cm) was used to make the original $c_{SSY} = 0.98$ mol/kg solution. The mixing was done on a vortex mixer at 2000 rpm in isotropic phase for several minutes, then at room temperature overnight. The SSY mixture was then split into smaller portions to add salts NaCl (99.5%, Sigma-Aldrich) or $MgSO_4$ (Reagent, Sigma-Aldrich). The new mixtures were mixed again on vortex overnight at 2000 rpm. Comparing to the previously reported procedure [2], in which SSY was added into pre-mixed salt solution, current procedure minimizes the error of c_{SSY} and its influence on the viscoelastic measurements.

The $c_{SSY} = 0.98$ mol/kg + NaOH solutions were made following previously reported procedure [2] by adding SSY into NaOH (Reagent, Acros) solutions of 0.01 and 0.02 mol/kg and then mixing in vortex for 3 h. Plastic vials and pipets were used to avoid reaction between NaOH and glass that reduces pH and affects LCLC properties.

3.2.2 Viscoelastic Constants Measurement

We follow the customized magnetic Frederiks transition technique for LCLCs, using cells of two distinct surface alignments, planar and homeotropic anchoring, to measure $\frac{K_1}{\Delta\chi}$, $\frac{K_2}{\Delta\chi}$ and $\frac{K_3}{\Delta\chi}$ [7]; $\Delta\chi$ is the diamagnetic anisotropy. In the twist measurement setup, we measure the dynamics of optical response to abruptly changed magnetic field and obtain the rotation viscosity coefficient γ_1 [12] (see Sect. 3.5.5). $\Delta\chi$ is measured using a superconducting quantum interference device (SQUID) following Ref. [7, 13], see Sect. 3.5.3, Fig. 3.6.

3.3 Results and Discussions

3.3.1 *Splay Constant* K_1

Splay constant K_1 is on the order of 10 pN and decreases as T increases, Fig. 3.2a. K_1 shows a dramatic response to the addition of divalent salt $MgSO_4$, by increasing its value by a factor of about 3. Similarly strong but opposite effect of decreasing K_1 is observed upon addition of small amount ($\sim$0.01 mol/kg) of NaOH. The monovalent salt NaCl shows little, if any, effect.

Following the earlier models of Onsager [14], Odijk [15] and Meyer [16], K_1 is expected to grow linearly with the length of aggregates $\bar{L}$, since splay deformation require one to fill splay-induced vacancies by the free ends of aggregates, as discussed by Meyer [16]:

$$K_1 = \frac{4}{\pi}\frac{k_B T}{D}\phi\frac{\bar{L}}{D} \tag{3.1}$$

The LCLC aggregates are polydisperse, so that the length $\bar{L}$ is some average measure of the balance of the attractive forces of stacking, characterized by the so-called scission energy E and entropy. The scission energy, estimated to be roughly of the order of $10\,k_BT$ [2, 10, 11, 17], measures the work one needs to perform to separate a single aggregate into two. In both isotropic and nematic phases [7, 18], the dependency of $\bar{L}$ on E is expected to be exponentially strong, $\bar{L} \propto \exp\left(\frac{E}{2k_BT}\right)$, where k_B is the Boltzmann constant and T is the absolute temperature. The scission energy can be approximated as $E = E_0 - E_e$ to reflect the fact that it depends on the strength (E_0) of $\pi - \pi$ attractions of aromatic cores and electrostatic repulsion (E_e) of ionized sulfonate groups at the periphery of SSY molecules. The strength of E_e should depend quadratically on linear charge density τ on aggregates, $E_e \propto \tau^2$. According to Manning [19–21], condensation of counter ions reduces linear charge density from $\tau^{\max}e \approx 6e$/nm to an effective one, $\tau e = \frac{1}{Zl_B}e$, where Z is the valence of counter ions, and $l_B = e^2/(4\pi\varepsilon\varepsilon_0 k_B T) \approx$ 0.7 nm is the Bjerrum length in water at 300 K. E_e should further decrease as Debye screening is enhanced by addition of ions. Following MacKintosh et al. [22], we estimate (see Sect. 3.5.1) that E_e scales as:

$$E_e \propto \tau^2\lambda_D \tag{3.2}$$

where $\lambda_D = \sqrt{\frac{\varepsilon\varepsilon_0 k_B T}{e^2\sum_i n_i q_i^2}}$ is the Debye screening length, n_i, q_i are the number density and strength of the ith ions in solution, respectively. According to Eq. (3.2), one expect the proportions of the electrostatic parts E_e of the scission energy for the salt-free SSY, SSY with added c_{NaCl} = 0.9 mol/kg of NaCl and SSY with

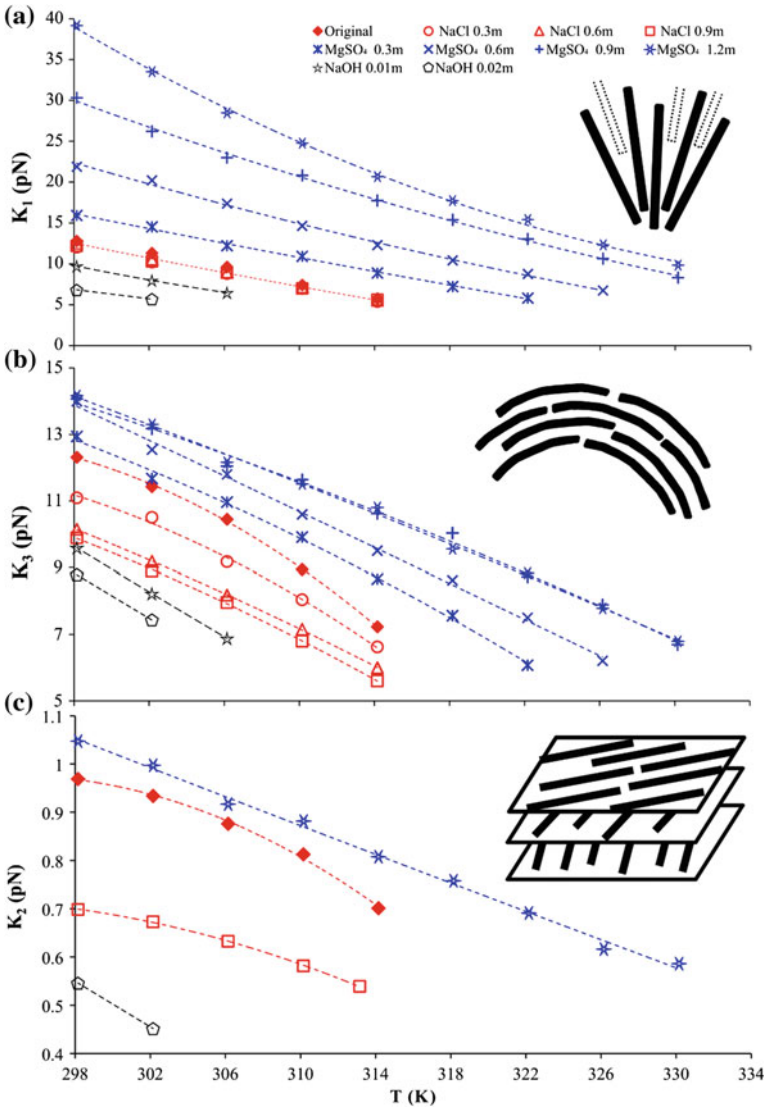

Fig. 3.2 Temperature and ionic content dependence of **a** splay constant K_1, **b** bend constant K_3 and **c** twist constant K_2 of SSY LCLC, $c_{SSY} = 0.98$ mol/kg with ionic additives. *Insets* illustrate the corresponding director deformation, where **a** splay creates vacancies that require free ends to fill in, **b** bend can be accommodated by bending the aggregates and **c** twist can be realized by stacking "pseudolayers" of uniformly aligned aggregates within the layers; director rotates only when moving across layers

c_{MgSO_4} = 1.2 mol/kg of $MaSO_4$ to be as following: $E_e^o : E_e^{NaCl} : E_e^{MgSO_4}$ = 1:0.72:0.10. This estimate suggests that Mg^{2+} has a stronger effect than Na^+ in the increase of E and thus K_1, since $K_1 \propto \bar{L} \propto \exp\left(\frac{E}{2k_BT}\right)$, in qualitative agreement with the experimental data. Interestingly, end-to-end attraction of short DNA strands has been observed in presence of divalent ion Mg^{2+} but not in presence of Na^+ [23]. Ionic additives are also known to change the aggregation length in self-assembled polyelectrolytes such as worm-like micelles [22, 24, 25].

The effect of NaOH is opposite to that of the addition of salts since high pH increases the degree of ionization τ of the sulfonate groups [2, 26], thus enhancing electrostatic repulsions of the molecules, shortening the aggregates and making the splay constant K_1 smaller.

3.3.2 *Bend Constant* K_3

Bend constant K_3 is on the order of 10 pN and decreases as T increases, Fig. 3.2b. When salts are added, at a given temperature, the effect of NaCl and $MgSO_4$ is different, namely, NaCl leads to a smaller K_3 and $MgSO_4$ makes K_3 larger. In presence of even small amount of NaOH (0.01 mol/kg), K_3 decreases. The bend constant is determined first of all by the flexibility of the aggregates that can be described by the persistence length λ_p, defined as the length over which unit vectors tangential to the aggregates lose correlation. The expected trend is [7, 15, 16]:

$$K_3 = \frac{4}{\pi}\frac{k_BT}{D}\phi\frac{\lambda_p}{D} \tag{3.3}$$

Flexibility of SSY aggregates should depend on the electrostatic repulsions of surface charges since bend brings these like-charges closer together. As discussed above, addition of NaCl does not change the scission energy E and the transition temperatures $T_{N\rightarrow N+I}$ much. However, when the bend deformation are imposed, the NaCl-induced screening of the like charges might become stronger at shorter distances, thus reduces K_3, Fig. 3.3. Interestingly, K_3 shows a linear dependence on λ_D^2 that decreases as c_{NaCl} increases, Fig. 3.3b. A similar mechanism of increased flexibility upon addition of salts such as NaCl is considered for isolated molecules of ds-DNA [27–29]. In the Odijk-Skolnick-Fixman (OSF) model [30, 31], the expected decrease of persistence length is on the order of 10% and only if the concentration of salt is below 0.05 M. In Manning's approach [19–21], the decrease of persistence length is larger, about 45% when NaCl concentration increases from 0.1 to 1 M. Our experimental data fall in between the two limits. Both models [20] predict $\lambda_p \propto \lambda_D^2$, consistent with our experimental K_3 and Eq. (3.3), Fig. 3.3b.

The effect of $MgSO_4$ on K_3 is harder to describe as the divalent salt noticeably enhances the temperature range of the nematic phase, increasing the scission energy and the transition point $T_{N\rightarrow N+I}$ (by up to 17 K). If the data are compared at the

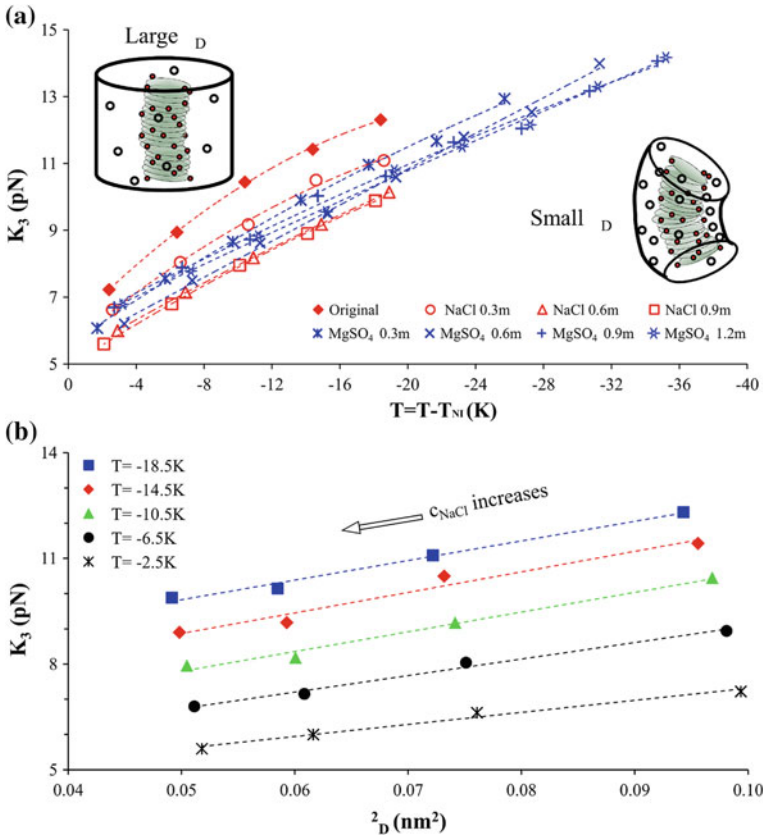

Fig. 3.3 **a** K_3 as a function of $\Delta T = T - T_{N\to N+I}$ for different ionic contents; *insets* show schematically that enhanced Debye screening increases the flexibility of aggregates. **b** For values measured at different ΔT, K_3 show linear relations with λ_D^2, which decreases as c_{NaCl} increases

same temperature, K_3 is increased in the presence of $MgSO_4$, Fig. 3.2b. However, if one plots K_3 versus a relative temperature, $\Delta T = T - T_{N\to N+I}$, Fig. 3.3a, then the effect of added $MgSO_4$ is in reduction of K_3, in agreement with the idea of salt-induced screening of the surface charges that make the aggregates more flexible.

3.3.3 *Twist Constant* K_2

Twist constant K_2 is on the order of 1 pN, about 10 times smaller than K_1 and K_3, Fig. 3.2c. Similarly to the case of K_3, addition of NaCl decreases K_2, while divalent salt $MgSO_4$ increases K_2; small amounts ($\sim$0.01 mol/kg) of NaOH decrease K_2.

As compared to other modes of deformation, twist is the easiest one in LCLCs, since it does not require finding free ends or deforming the aggregates. In an ideal arrangement, aggregates lie in consecutive "pseudolayers", with the director $\hat{n}$ rotating by a small angle only when moving between the pseudolayers, Fig. 3.2c inset. The aggregates may be displaced across the layers by thermal fluctuation and interfere with aggregates of a different orientation. This interference can be relieved by bending the aggregates to follow local orientational order. Thus K_2 is expected to be independent of $\bar{L}$ and weakly dependent on λ_p (as compared to K_3); as suggested by Odijk [15]

$$K_2 = \frac{k_B T}{D} \phi^{1/3} \left(\frac{\lambda_p}{D} \right)^{1/3} \tag{3.4}$$

From Eq. (3.4), we expect twist constant K_2 to change in a similar way as K_3 does in response to the ionic additives, since both of them depend on λ_p. Experimental results, Fig. 3.2c, do show a qualitative agreement with this prediction.

3.3.4 Rotation Viscosity γ_1

Rotation viscosity γ_1 covers a range of (0.2–7) $\mathrm{kgm^{-1}\,s^{-1}}$, several orders of magnitudes higher than $\gamma_1 \sim 0.01\ \mathrm{kgm^{-1}\,s^{-1}}$ of a standard thermotropic LC 5CB (4′-n-pentyl-4-cyanobiphenyl) [32]. γ_1 decreases exponentially as T increases, Fig. 3.4. Addition of NaCl increase γ_1 by a small factor, while $MgSO_4$ increases γ_1 dramatically; addition of NaOH decreases γ_1. Analysis of the experimental data shows that $\gamma_1 \propto K_1^2$ in all cases, Fig. 3.4. insets.

Director rotation in the nematic LCs composed of long slender particles ($L/D \gg 1$) induces mass displacement, and is thus coupled with macroscopic flows. According to Meyer's geometry argument [16, 33–35], a twist deformation that induces shear flow $\frac{\partial v}{\partial z}$ = constant causes power dissipation per monomer along the aggregates as $P = \mu z^2 \left(\frac{\partial v}{\partial z} \right)^2$, where μ is a friction coefficient and z is the distance of the monomer to the rotation center. The mean power dissipation $\bar{P} = \frac{1}{\bar{L}} \int_{-\bar{L}/2}^{\bar{L}/2} P dz = \mu \frac{\bar{L}^2}{12} \left(\frac{\partial v}{\partial z} \right)^2$; thus the rotation viscosity γ_1 scales as:

$$\gamma_1 \propto \bar{L}^2 \tag{3.5}$$

According to previous analysis of $\bar{L} \propto \exp\left(\frac{E}{2k_B T} \right)$ and Eq. (3.5), the exponential dependence $\gamma_1 \propto \bar{L}^2 \propto \exp\left(\frac{E}{k_B T} \right)$ makes γ_1 sensitive to T and E, and implies that $\gamma_1 \propto K_1^2$, Eq. (3.1). The experimental findings for γ_1, Fig. 3.4, such as exponential

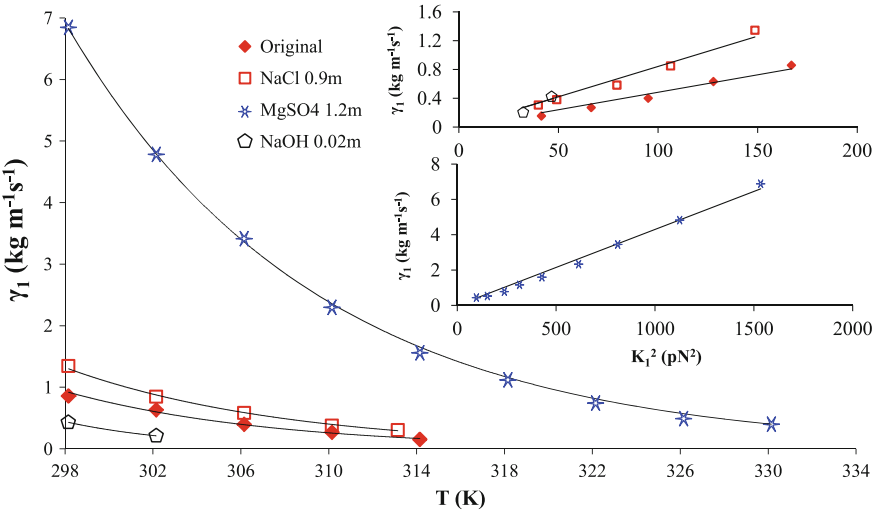

Fig. 3.4 Temperature and ionic content dependence of rotation viscosity γ_1 of SSY LCLC, c_{SSY} = 0.98 mol/kg with ionic additives. *Insets* show the linear relation, $\gamma_1 \propto K_1^2$ for all measurements

dependence on T, effect of $MgSO_4$ and NaOH, and the scaling $\gamma_1 \propto K_1^2$, all agree with these expectations and are consistent with the previous analysis of the K_1 behavior. The only discrepancy is that the addition of NaCl increases γ_1 while shows little influence on K_1. Of course, these trends are discussed only qualitatively and in the simplest terms possible, avoiding other important factors, such as possible structural defects in formation of SSY aggregates [2, 36, 37], collective and dynamic effects, etc.

3.4 Conclusion

We measured the temperature and ionic content dependences of anisotropic elastic moduli and rotation viscosity of the self-assembled orientationally ordered system formed by the polydisperse self-assembled aggregates of dye SSY bound by weak non-covalent forces. We observe dramatic and versatile changes of the viscoelastic properties induced by the ionic additives that alter the electrostatic interactions caused by charged groups at the surface of aggregates. We connect these macroscopic properties to the microscopic structural and mechanical features of the aggregates, such as the average contour length $\bar{L}$ and persistence length λ_p, and explain our findings through the idea that both $\bar{L}$ and λ_p are controlled by the ionic content. This type of sensitivity of the building units of an orientationally ordered system to the ionic properties of the medium are absent in the conventional

thermotropic and lyotropic LCs (such as polymer melts) featuring the building units with the shape that is fixed by the strong covalent bonds. Further understanding of the link between the viscoelastic anisotropy and composition of the chromonic system require a substantial advance in theoretical description at the level of individual aggregates and their collective behavior. The presented experimental data might be of importance in verifying the validity of various models.

3.5 Supplemental Information

3.5.1 *Estimation of* E_e

Disassociation of Na^+ into water makes SSY aggregates charged, with a maximum possible charge density $\tau^{\max} e \approx 6e$/nm, corresponding to Manning's reduced charge density $\xi = l_B \tau \approx 4.2$, where $l_B = e^2/(4\pi\varepsilon\varepsilon_0 k_B T) \approx 0.7$ nm is the Bjerrum length in water at 300 K. Counterion condensation happens at the aggregate surfaces [17, 19] and renormalizes $\xi > \frac{1}{Z}$ to $\xi = \frac{1}{Z}$, thus reduces τ to $\frac{1}{Zl_B}$, where Z is the valence of the counter ions. The repulsive interaction is further reduced by counterion screening. MacKintosh et al. [22] estimates E_e in the form of:

$$E_e = \frac{l_B D \tau^2 k_B T}{2\tilde{\phi}^{1/2}} \tag{3.6}$$

where $\tilde{\phi} = \phi + (D/\lambda_D)^2$ considers screening effect from both increases volume fraction ϕ (ions are pushed closer to aggregates) and enhanced screening by addition of ions. In all studied SSY, $\lambda_D \leq$ 0.31 nm, $(D/\lambda_D)^2 \gg 1$, thus we approximate $\tilde{\phi} \approx (D/\lambda_D)^2$ to simplify E_e:

$$E_e = \frac{l_B \tau^2 k_B T \lambda_D}{2} \tag{3.7}$$

3.5.2 *Volume Fraction* ϕ

We approximate the solvent of SSY (pure water, or water solution of ionic additives) as continuum media and measure the density of both the solvents $\rho_{solvent}$, and nematic SSY LCLC,ρ_{SSY}, with a densitometer DE45 (Mettler Toledo). From the molality of SSY and ionic additives, we calculate the weight percentage (w) of SSY in the final LCLC.

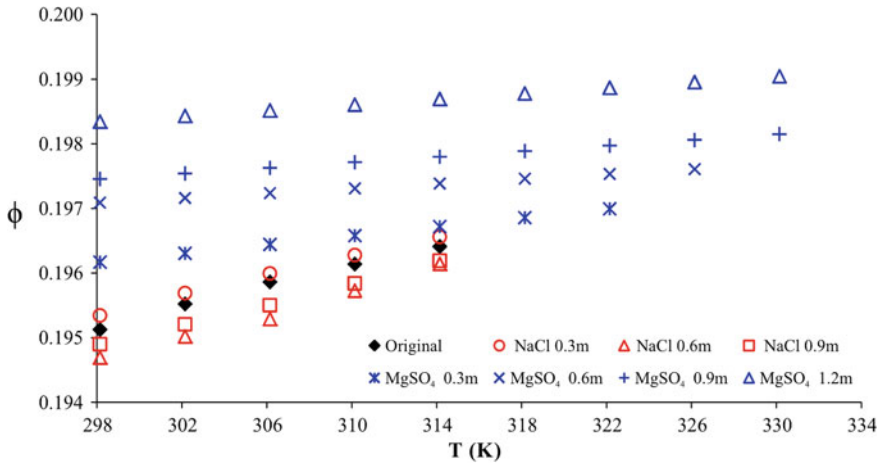

Fig. 3.5 Temperature and ionic content dependences of volume fraction ϕ of SSY

$$w = \frac{c_{SSY} M_{SSY}}{c_{SSY} M_{SSY} + c_{ion} M_{ion} + 1} \tag{3.8}$$

where molality of SSY $c_{SSY} = 0.98$ mol/kg is fixed in all experiments, $M_{SSY} = 0.452$ kg/mol is the molecular weight of SSY, c_{ion} and M_{ion} are the molality and molecular weight of ionic additives. We then calculate the volume fraction ϕ of SSY:

$$\phi = 1 - \phi_{solvent} = 1 - \frac{\frac{1-w}{\rho_{solvent}}}{\frac{1}{\rho_{SSY}}} = 1 - (1-w)\frac{\rho_{SSY}}{\rho_{solvent}} \tag{3.9}$$

The result of ϕ is shown in Fig. 3.5. The change of ϕ is insignificant, with a maximum increase of about 0.004, thus we can treat ϕ as constant in calculations. Notice that NaCl barely changes ϕ, while $MgSO_4$ slightly increases ϕ as c_{MgSO_4} increases. This is consistent with the analysis of the elongation of aggregates and enhanced nematic order reflected on phase diagram, Fig. 3.1. NaOH doped SSY solutions are not measured due to the corrosive nature of NaOH to SiO_x, which can damage the equipment and affect accuracy.

3.5.3 *Diamagnetic Anisotropy* $\Delta\chi$

As described earlier in Sect. 2.5.2 and Ref. [13], we used a superconducting quantum interference device to determine the mass diamagnetic susceptibility $\Delta\chi_m$

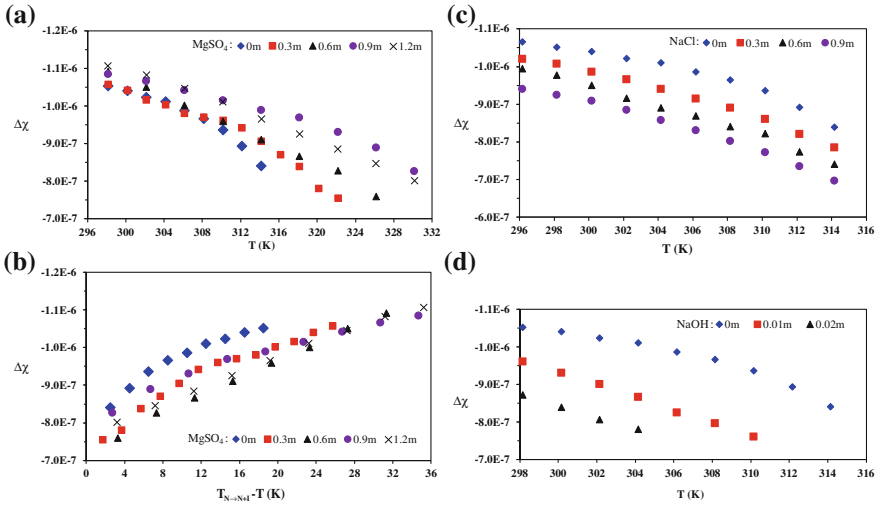

Fig. 3.6 Temperature dependence of diamagnetic anisotropy $\Delta\chi$ for SSY at fixed concentration c_{SSY} = 0.98 mol/kg, with various amount of additional ionic additives: **a**, **b** $MgSO_4$, **c** NaCl and **d** NaOH

of the samples. Combined with the density measurements, we obtain the dimensionless diamagnetic anisotropy $\Delta\chi$, as a function of temperature and ionic additives, Fig. 3.6. Since NaOH solution can react with glass tube and change the composition in SSY LLC, the phase diagram and consequently viscoelastic properties of the SSY LCLC are affected. To avoid it, we used a Teflon tube instead of glass NMR tube for the $\Delta\chi_m$ measurements. For the same reason, we cannot measure the density of SSY + NaOH solution directly using the densitometer. Instead, we used the density of the original SSY solution to calculate $\Delta\chi$, assuming that the density change of SSY with small amount of additional NaOH ($c_{NaOH} = (0.01 - 0.02)\ m$) is negligible.

Addition of $MgSO_4$ into the c_{SSY} = 0.98 mol/kg SSY solution stabilizes the nematic phase, Fig. 3.1. As a result, at a fixed absolute temperature, $\Delta\chi$ increases as $MgSO_4$ concentration increases, Fig. 3.6a. However, if we compare $\Delta\chi$ of SSY with different $MgSO_4$ concentrations at deduced temperature $T_{N\to N+I} - T$, we find that the addition of $MgSO_4$ decreases $\Delta\chi$, Fig. 3.6b, similar to NaCl and NaOH cases, Fig. 3.6c, d. This can be explained by the increased Debye screening that makes the aggregates more flexible, thus reduces the orientational order under thermal fluctuations.

3.5.4 Birefringence Δn and Scalar Order Parameter S

We measure the birefringence Δn and scalar order parameter S using the technique described in [38], same as in Chap. 2. Both Δn and S show similar behavior as $\Delta\chi$ does, which is reasonable, since $\Delta\chi,\ \Delta n \propto S$ (Fig. 3.7).

3.5.5 Measurement of Rotation Viscosity γ_1

In the twist geometry, as the magnetic field increases, the director experiences first a small splay deformation, then a uniform twist across the cell, see Sect. 2.5.6. Since change of the polar anger θ is less than 5°, we approximate θ = 90°, and describe the director field with a pure twist deformation with a director field $\hat{\mathrm{n}} = (\cos\varphi, \sin\varphi, 0)$, where $\varphi(z)$ is the azimuthal angle of local director at height z. The magnetic field $\mathrm{B} = B(\sin\theta_B, 0, \cos\theta_B)$ is applied with θ_B = 75°, and planar surface alignment provides the initial director direction $\mathrm{n}_0 = (1, 0, 0)$. The Frank-Oseen elastic energy density is:

$$f = \frac{1}{2}K_2\left(\frac{\partial\varphi}{\partial z}\right)^2 - \frac{1}{2}\frac{\Delta\chi}{\mu_0}B^2\sin^2\theta_B\cos^2\varphi \tag{3.10}$$

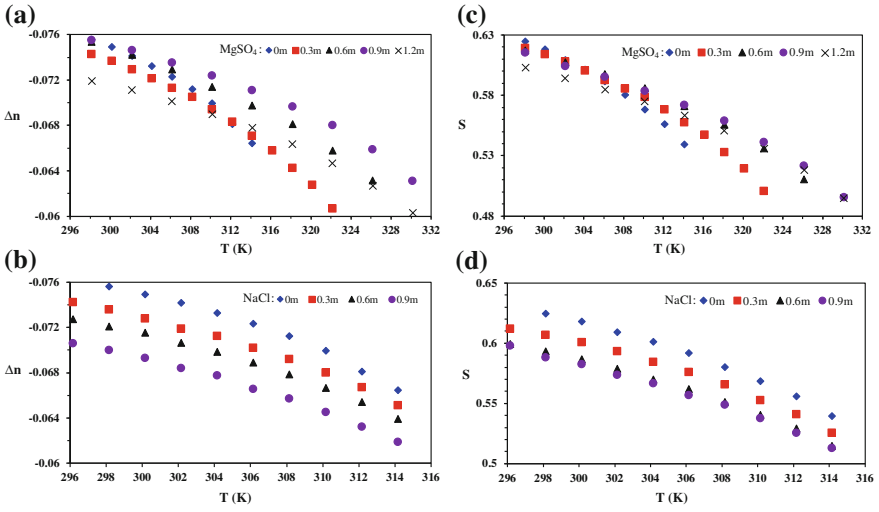

Fig. 3.7 Temperature dependence of birefringence Δn and scalar order parameter S for SSY at fixed c_{SSY} = 0.98 mol/kg with various concentration of ionic additives: Δn of SSY with additional **a** $MgSO_4$ and **b** NaCl; S of SSY with additional **c** $MgSO_4$ and **d** NaCl

We define a frictional coefficient γ to describe the energy dissipation when the total free energy changes:

$$A\int_0^d \gamma\left(\frac{d\hat{\boldsymbol{n}}}{dt}\right)^2 = -\frac{d}{dt}A\int_0^d f dz \tag{3.11}$$

Plug in $\hat{\boldsymbol{n}}$ and f, the differential form of Eq. (3.11) reads:

$$\gamma\frac{\partial\varphi}{\partial t} = K_2\frac{\partial^2\varphi}{\partial z^2} - \frac{\Delta\chi}{\mu_0}B^2\sin^2\theta_B sin\varphi\cos\varphi \tag{3.12}$$

At small φ, we linearize the above equation with approximations $\cos\varphi \approx 1$ and $\sin\varphi \approx \varphi$, and assume that φ follows a simple form of $\varphi = \varphi_0\exp\left(\frac{t}{\tau_0}\right)\sin(qz)$, where φ_0 is the azimuthal angle at center of the cell, τ_0 is a characteristic time describing the decay ($\tau_0 < 0$) or growth ($\tau_0 > 0$) of φ, $q = \frac{\pi}{d}$. The linearized Eq. (3.12) then turns into a linear relation between $\frac{1}{\tau_0}$ and B^2:

$$\frac{1}{\tau_0} = -\frac{1}{\gamma}\frac{\Delta\chi}{\mu_0}B^2\sin^2\theta_B - \frac{1}{\gamma}K_2q^2 \tag{3.13}$$

Experimentally, we can obtain relaxation rate $\frac{1}{\tau_0}$ from the dynamics of light intensity $I(t)$. In the twist geometry, we expect:

$$I \propto \sin^2\frac{\Gamma}{2} \tag{3.14}$$

where Γ is the total retardation caused by the azimuthal rotation of the director field, experienced by the oblique incident light. An analytical calculation of Γ is difficult, but in general one can assume:

$$\Gamma = \int_0^d \varphi_t\sin qz\cdot g(z)dz \propto \varphi_t \tag{3.15}$$

where $\varphi_t = \varphi_0\exp\left(\frac{t}{\tau_0}\right)$ is the time dependence of azimuthal angle, and $g(z)$ describes the detail of phase retardation calculation. At small Γ, we linearize Eq. (3.14):

$$I \propto \left[\varphi_0\exp\left(\frac{t}{\tau_0}\right)\right]^2 \tag{3.16}$$

Numerical simulation supports our expectation of Eq. (3.16), Fig. 3.8c. Up to $\varphi_0 \approx 12^\circ$, $I \propto \varphi_0^2$ is satisfied. In the experiments, we measure $I(t)$ up to $10^{-2}I_{\max}$

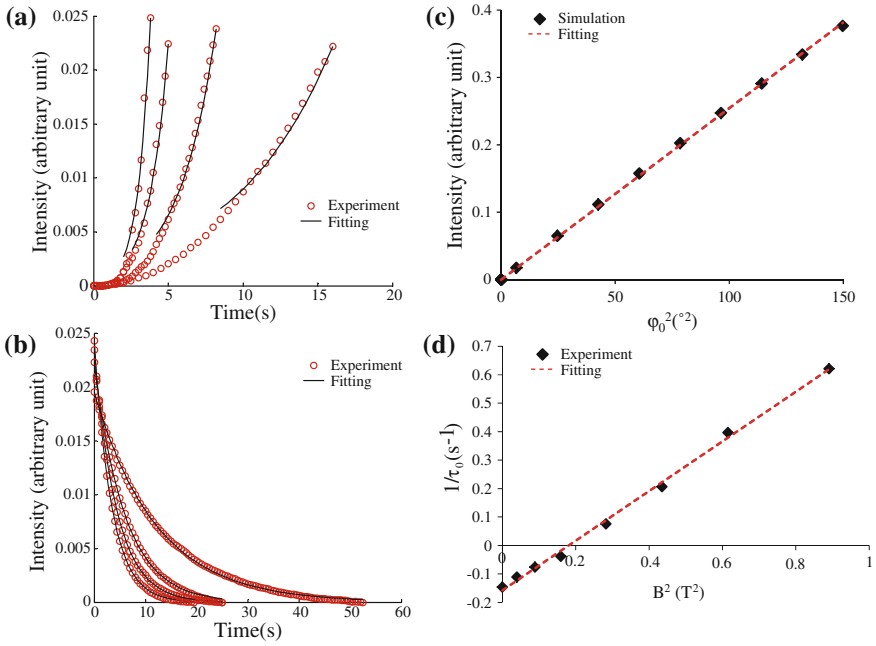

Fig. 3.8 Measurement of rotational viscosity γ_1 from the relaxation of magnetic field induced twist. **a** Intensity increase in response to suddenly applied magnetic fields $B > B_{th}$; B_{th} is the threshold field of twist Frederiks transition. **b** Intensity decay in response to suddenly reduced magnetic field. **c** Numerical simulation shows that intensity increases quadratically with the mid-plane twisting angle φ_0. **d** Linear fit of $1/\tau_0$ versus B^2, where the rotation viscosity γ_1 can be extracted from the slope

(to satisfy small Γ condition) and fit it with exponential function to obtain $1/\tau_0$ at various B values, Fig. 3.8a, b. Then we fit $1/\tau_0$ versus B^2 to obtain γ, Fig. 3.8d. A calculation strictly following nematodynamics [12] shows that γ is equivalent to the generally defined rotation viscosity γ_1.

References

1. Kostko AF et al (2005) Salt effects on the phase behavior, structure, and rheology of chromonic liquid crystals. J Phys Chem B 109:19126–19133
2. Park HS et al (2008) Self-assembly of lyotropic chromonic liquid crystal sunset yellow and effects of ionic additives. J Phys Chem B 112(51):16307–16319
3. Park HS, Kang SW, Tortora L, Kumar S, Lavrentovich OD (2011) Condensation of self-assembled lyotropic chromonic liquid crystal sunset yellow in aqueous solutions crowded with polyethylene glycol and doped with salt. Langmuir 27(7):4164–4175

4. Tortora L et al (2010) Self-assembly, condensation, and order in aqueous lyotropic chromonic liquid crystals crowded with additives. Soft Matter 6(17):4157–4167
5. Baumann CG, Smith SB, Bloomfield VA, Bustamante C (1997) Ionic effects on the elasticity of single DNA molecules. Proc Natl Acad Sci U S A 94:6185–6190
6. Smith SB, Cui Y, Bustamante C (1996) Overstretching B-DNA: the elastic response of individual double-stranded and single-stranded DNA molecules. Science 271(5250):795–799
7. Zhou S et al (2012) Elasticity of lyotropic chromonic liquid crystal probed by director reorientation in a magnetic field. Phys Rev Lett 109:037801
8. Lydon J (2011) Chromonic liquid crystalline phases. Liq Cryst 38(11–12):1663–1681
9. Dickinson AJ, LaRacuente ND, McKitterick CB, Collings PJ (2009) Aggregate structure and free energy changes in chromonic liquid crystals. Mol Cryst Liq Cryst 509:751–762
10. Horowitz VR, Janowitz LA, Modic AL, Heiney PA, Collings PJ (2005) Aggregation behavior and chromonic liquid crystal properties of an anionic monoazo dye. Phys Rev E 72:041710
11. Luoma RJ (1995) X-ray scattering and magnetic birefringence studies of aqueous solutions of chromonic molecular aggregates. Ph.D. Thesis, Brandeis Unversity, Waltham, MA, USA
12. de Gennes PG, Prost J (1993) The physics of liquid crystals. Clarendon Press, Oxford, p 598
13. Frisken BJ, Carolan JF, Palffy-Muhoray P, Perenboom JAAJ, Bates GS (1986) SQUID susceptibility measurements of 5CB. Mol Cryst Liq Cryst Lett 3:57–62
14. Onsager L (1949) The effects of shape on the interaction of colloidal particles. Ann NY Acad Sci 51:627–649
15. Odijk T (1986) Elastic constants of nematic solutions of rod-like and semi-flexible polymers. Liq Cryst 1:553–559
16. Meyer RB (1982) Polymer liquid crystals. In: Ciferri A, Krigbaum WR, Meyer RB (eds). Academic Press, New York
17. Chami F, Wilson MR (2010) Molecular order in a chromonic liquid crystal: a molecular simulation study of the anionic azo dye sunset yellow. J Am Chem Soc 132(22):7794–7802
18. der Schoot Pv, Cates ME (1994) The isotropic-to-nematic transition in semi-flexible micellar solutions. Europhys Lett 25:515
19. Manning GS (1978) The molecular theory of polyelectrolyte solutions with applications to the electrostatic properties of polynucleotides. Q Rev Biophys 11:179–246
20. Manning GS (2001) Counterion condensation on a helical charge lattice. Macromolecules 34:4650–5655
21. Manning GS (2006) The persistence length of DNA is reached from the persistence length of its null isomer through an internal electrostatic stretching force. Biophys J 91:3607–3616
22. MacKintosh FC, Safran SA, Pincus PA (1990) Self-assembly of linear aggregates: the effect of electrostatics on growth. Europhys Lett 12:697–702
23. Qiu X et al (2007) Inter-DNA attraction mediated by divalent counterions. Phys Rev Lett 99:038104
24. Safran SA, Pincus PA, Cates ME, MacKintosh FC (1990) Growth of charged micelles. J Phys France 51:503–510
25. Odijk T (1989) Ionic strength dependence of the length of charged linear micelles. J Phys Chem 93:3888–3889
26. Gooding JJ, Compton RG, Brennan CM, Atherton JH (1997) A new electrochemical method for the investigation of the aggregation of dyes in solution. Electroanalysis 9(10):759–764
27. Sobel ES, Harpst JA (1991) Effects of Na^+ on the persistence length and excluded volume of T7 bacteriophage DNA. Biopolymers 31:1559–1564
28. Manning GS (1981) A procedure for extracting persistence lengths from light-scattering data on intermediate molecular weight DNA. Biopolymers 20:1751–1755
29. Kam Z, Borochov N, Eisenberg H (1981) Dependence of laser light scattering of DNA on NaCl concentration. Biopolymers 20:2671–2690
30. Odijk T (1977) Polyelectrolytes near the rod limit. J Polym Sci Part B Polym Phys 15: 477–483
31. Fixman M, Skolnick J (1977) Electrostatic persistence length of a wormlike polyelectrolyte. Macromolecules 10(5):944–948

32. Cui M, Kelly JR (1999) Temperature dependence of visco-elastic properties of 5CB. Mol Cryst Liq Cryst 331:49–57
33. Lee S-D, Meyer RB (1990) Light scattering measurements of anisotropic viscoelastic coefficients of a main-chain polymer nematic liquid crystal. Liq Cryst 7(1):15–29
34. Lee S-D, Meyer RB (1988) Crossover behavior of the elastic coefficients and viscosities of a polymer nematic liquid crystal. Phys Rev Lett 61:2217
35. Taratuta VG, Hurd AJ, Meyer RB (1985) Light-scattering study of a polymer hematic liquid crystal. Phys Rev Lett 55:246
36. Zhou S et al (2014) Elasticity, viscosity, and orientational fluctuations of a lyotropic chromonic nematic liquid crystal disodium cromoglycate. Soft Matter. doi:10.1039/c1034sm00772g
37. Xiao W et al (2014) Structural correspondence of solution, liquid crystal, and crystalline phases of the chromonic mesogen sunset yellow. Cryst Growth Des. doi:10.1021/cg500752x
38. Nastishin YA et al (2005) Optical characterization of the nematic lyotropic chromonic liquid crystals: Light absorption, birefringence, and scalar order parameter. Phys Rev E 72(4): 041711

Chapter 4
Elasticity, Viscosity, and Orientational Fluctuations of a Lyotropic Chromonic Nematic Liquid Crystal Disodium Cromoglycate

4.1 Introduction

There are two primary experimental techniques to determine the viscoelastic properties of nematic liquid crystals (LCs) [1]: (1) the Frederiks transition, i.e., reorientation of the axis of nematic order (director) by an applied field, and (2) light scattering on thermal fluctuations of the director. The magnetic Frederiks transition has been applied to explore the elastic properties of two LCLCs, disulphoindantrone [2, 3] and sunset yellow (SSY) [4], as discussed in Chaps. 2–3. The Frederiks approach requires the LC director to be uniformly aligned in two different fashions, planar and homeotropic, with the director parallel to the bounding substrates of the sample cell and perpendicular to them, respectively. Such a requirement is difficult to satisfy for lyotropic systems. In particular, homeotropic anchoring of LCLCs has been reported only for a few cases [4–6]. One of the most studied LCLCs, representing water dispersions of disodium cromoglycate (DSCG), shows only transient homeotropic alignment (although there is a recent report on the homeotropic alignment at a grapheme substrate [6]), thus making it difficult to determine the viscoelastic properties of this material. On the other hand, knowledge of viscoelastic properties of DSCG is of particular importance for further understanding of LCLCs, since DSCG is optically transparent and has been used as a biocompatible component in real-time biological sensors [7] and in formulations of LCLC-bacterial dispersions [8–10].

In this chapter, in order to characterize the material parameters of the nematic phase of water solutions of DSCG, we use the dynamic light scattering (DLS) that requires only one type (planar) of surface anchoring. The approach is similar to the one used previously by Meyer et al. to characterize polymer solutions exhibiting the nematic phase [1, 11–15], and allows one to extract both the elastic moduli and the viscosity coefficients. By calibrating the set-up with the measurement of DLS spectrum for the well-studied nematic 4′-*n*-pentyl-4-cyanobiphenyl (5CB),

© Springer International Publishing AG 2017

S. Zhou, *Lyotropic Chromonic Liquid Crystals*, Springer Theses,
DOI 10.1007/978-3-319-52806-9_4

we extract the absolute values of the elastic constants and viscosities for DSCG. The approach allows us to trace both the concentration and temperature dependences of these viscoelastic parameters. A small portion of these results (one concentration only) were made available in 2008 in electronic-Liquid Crystal Communications [16] and arXiv [17].

In these measurements, we observe that the splay elastic constant K_1, splay and twist viscosities η_{splay} and η_{twist} all increase dramatically as the temperature is reduced. The DLS spectrum not only shows the modes that correspond to the standard viscoelastic response (director modes), but also reveals an additional fluctuation mode weakly coupled to the director. We suggest that this mode is associated with structural defects in packing of chromonic aggregates such as stacking faults. The observed peculiarities of viscoelastic properties of LCLCs, absent in other LCs, originate from the fact that the chromonic molecules in the aggregates are bound by weak non-covalent interactions. As a result, the length of aggregates and the viscoelastic parameters that depend on it are extremely sensitive to both concentration and temperature.

4.2 Experimental Details

4.2.1 Materials

Disodium Cromoglycate (DSCG), Fig. 4.1a, was purchased from Spectrum Chemicals (98% purity) and subsequently dissolved in deionized water (resistivity 18 MΩ cm) at concentrations of c = 12.5, 14.0, 16.0 and 18.0 wt%. Following Ref. [18], the corresponding volume fractions are: ϕ = 0.089, 0.100, 0.115, and 0.129. The transition temperatures of the nematic to nematic-isotropic biphasic region are T_{ni} = 297.0 ± 0.2, 299.6 ± 0.4, 303.5 ± 0.3 and 306.2 ± 0.2 K, respectively, according to the established phase diagram [19] and our independent microscopy analysis. The DLS measurements were performed in the homogeneous nematic phase over the temperature range from 294.5 K to within 1 K of T_{ni}. The nematic director was aligned in a planar fashion by glass substrates coated with buffed layers of polyimide SE-7511 (Nissan Chemical Inc.) [20]. Optical cells of thickness 19 μm were sealed with epoxy to prevent water evaporation from the samples. The value of T_{ni} of each sample was checked before and after the measurement, showing changes of less than 1 K in all cases. For light scattering measurements, the samples were housed in a hot stage with optical access and temperature control with an accuracy of 0.1 K and stability of 0.01 K over 1 h.

The thermotropic nematic liquid crystal 4′-*n*-pentyl-4-cyanobiphenyl (5CB), used for reference measurements, was purchased from Sigma-Aldrich (98% purity). Planar alignment of the director in a 13.7 μm thick sample is produced by buffed polyimide PI2555 layers (HD MicroSystems) applied to surfaces of the flat glass substrates.

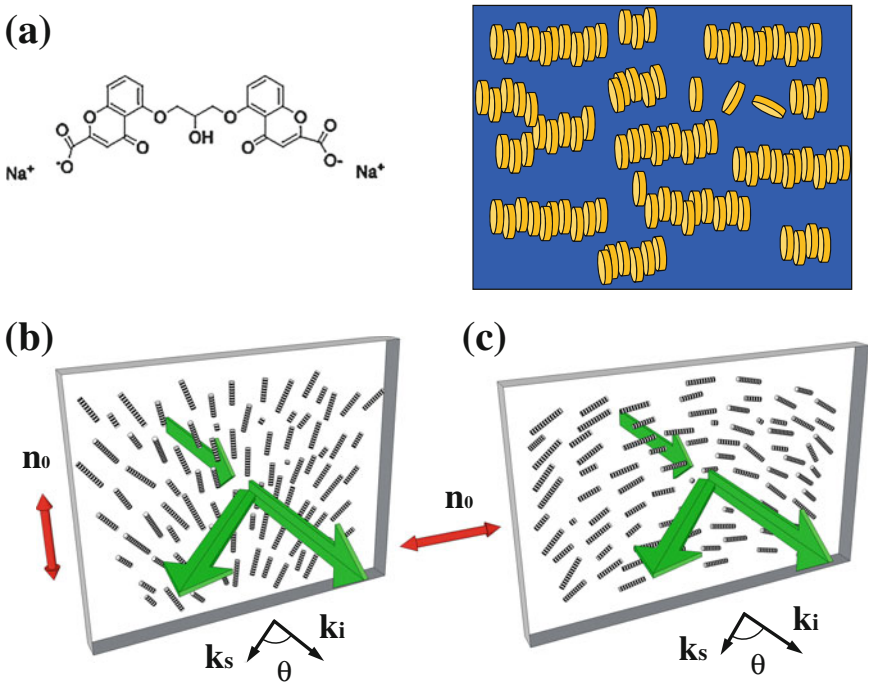

Fig. 4.1 **a** Structure of the DSCG molecule and generic representation of LCLC aggregates formed in aqueous solution. (Each disk in the aggregate stack may represent single or paired DSCG molecules.) **b**, **c** Schematic of experimental light scattering geometries used in our measurements: **b** "1&2", splay + twist (*pure splay shown*) geometry and **c** "3" bend-twist (*pure bend shown*) geometry. The *green arrows* indicate the incident ($\mathbf{k_i}$) and scattered ($\mathbf{k_s}$) light, with the polarization of light is in the plane of the *arrows*

4.2.2 Experimental Set-Up

In the two studied light scattering geometries, the director $\hat{\mathbf{n}}$ is either perpendicular (geometry "1&2", Fig. 4.1b) or parallel (geometry "3", Fig. 4.1c) to the scattering plane (the plane formed by incident wave vector $\mathbf{k_i}$ and scatter wave vector $\mathbf{k_s}$). The polarization ($\hat{\mathbf{i}}$) of the normally incident $\lambda = 532$ nm laser light is vertical; depolarized scattering was collected through a horizontal analyzer ($\hat{\mathbf{s}}$). The laser power was kept below 3 mW to avoid parasite effects of light absorption. Homodyne cross-correlation functions of the scattered light intensity (evenly split between two independent detectors) were recorded as a function of time on a nanosecond digital correlator. The angular-dependent average light intensity $I_{1\&2}(\theta)$ (divided by the incident light intensity I_0 in the sample) measured in geometry "1&2" may be expressed as [21]:

$$I_{1\&2} = I_1(\theta) + I_2(\theta) = (\Delta\varepsilon)^2(\pi\lambda^{-2})^2\Omega d A k_B T\left[\frac{G_1(\theta)}{K_1 q_\perp^2(\theta)} + \frac{G_2(\theta)}{K_2 q_\perp^2(\theta)}\right] \tag{4.1}$$

where θ is the laboratory scattering angle, Ω is the collection solid angle, A is the cross-sectional area and d the thickness of the illuminated sample volume, $\Delta\varepsilon = \varepsilon_\parallel - \varepsilon_\perp = n_\parallel^2 - n_\perp^2$ is the dielectric anisotropy at optical frequency, $n_\parallel$ and $n_\perp$ are the refractive indices for light polarized parallel and perpendicular to the director, respectively, and $q_\parallel(\theta)$ and $q_\perp(\theta)$ are the two components of scattering vector $\mathbf{q} = \mathbf{k_s} - \mathbf{k_i}$ along and perpendicular to $\hat{\mathbf{n}}$ respectively. The geometrical scattering factors $G_1(\theta)$ and $G_2(\theta)$ are:

$$G_1(\theta) = \frac{\cos^2\frac{\theta}{2}(1+p)^2}{1+p+s^2}, G_2(\theta) = \frac{\left(\sin\frac{\theta}{2} - s\cos\frac{\theta}{2}\right)^2}{1+p+s^2} \tag{4.2}$$

where $s = \frac{\Delta n}{2n_\perp \sin\frac{\theta}{2}}$, $p = \frac{\Delta n}{n_\perp}$, and $\Delta n = n_\parallel - n_\perp$ is the optical birefringence of the LCLC sample. The separation of $I_1(\theta)$ and $I_2(\theta)$ is done by fitting the time correlation function of the scattered intensity $I_{1\&2}(\theta)$ to two overdamped decay processes with different relaxation rates Γ_1 and Γ_2 (as discussed below).

The expression for the scattered intensity in geometry "3" is:

$$I_3(\theta) = (\Delta\varepsilon)^2(\pi\lambda^{-2})^2\Omega d A k_B T\frac{G_3(\theta)}{K_3 q_\parallel^2(\theta) + K_2 q_\perp^2(\theta)} \tag{4.3}$$

where $G_3(\theta) = \cos^2\theta$. In DSCG LCLC, as we will confirm below, $K_2 \ll K_3$. Over the range of angles $\theta = (5-35)^\circ$ studied, we estimate $\left(\frac{K_2 q_\perp^2}{K_3 q_\parallel^2}\right)_{\max} \approx 0.01$. Thus we neglect $K_2 q_\perp^2$ in Eq. (4.3), leading to:

$$I_3(\theta) = (\Delta\varepsilon)^2(\pi\lambda^{-2})^2\Omega d A k_B T\frac{G_3(\theta)}{K_3 q_\parallel^2(\theta)} \tag{4.4}$$

The cell gap (sample thickness) d was measured by interferometry in empty cells.

The measured intensities $I_{1,2,3}$ are functions of material parameters such as $\Delta\varepsilon$ and K's, and experimental conditions such as d and T. To obtain the absolute values of K_3, we calibrated the scattered intensity $I_3(\theta)$ measured on DSCG LCLC against measurements made in the identical geometry "3" set-up on a reference 5CB sample, whose values of $\Delta\varepsilon$, K_2 and K_3 are well known [22–24]. We can then deduce the absolute values of the DSCG elastic constant K_3 from the ratio

$$\frac{[I_3(\theta)]_{DSCG}}{[I_3(\theta)]_{5CB}} = \frac{\left[K_3 q_{\parallel}^2 + K_2 q_{\perp}^2\right]_{5CB}}{\left[K_3 q_{\parallel}^2\right]_{DSCG}} \frac{\left[G_3(\theta)(\Delta\varepsilon)^2 Td\right]_{DSCG}}{\left[G_3(\theta)(\Delta\varepsilon)^2 Td\right]_{5CB}} \tag{4.5}$$

and the values of K_1 and K_2 from similar ratios for $I_1(\theta)$ and $I_2(\theta)$.

From measurements of the homodyne intensity correlation function in time (τ), we obtain the angular dependent relaxation rates $\Gamma_\alpha(\theta)$ for the director fluctuations by fitting the experimental data in Fig. 4.2 to the standard expression for over-damped modes:

$$\langle I(0,\theta) I(\tau,\theta)\rangle = \bar{I}^2(\theta) + g^2 \left[\sum_\alpha \bar{I}_\alpha(\theta) \exp(-\Gamma_\alpha \tau)\right]^2 \tag{4.6}$$

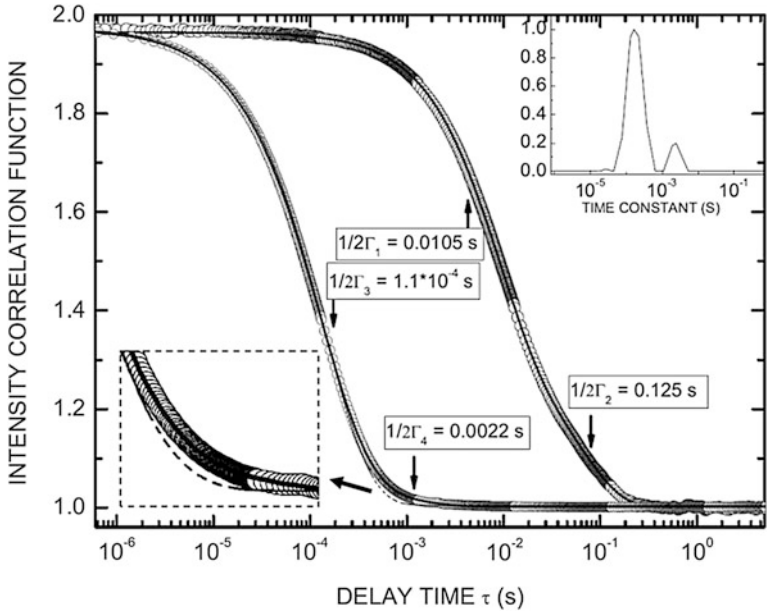

Fig. 4.2 Correlation functions (open *circles*) collected at T = 294 K for $q_{\parallel} = 1.64 \times 10^6$ m^{-1} in a bend (*left*) and for $q_{\perp} = 1.00 \times 10^7$ m^{-1} in splay + twist geometries (*right*) for the nematic LCLC formed by 14 wt% DSCG in water. Solid lines represent fits of the correlation functions (double exponential in the splay + twist geometry, stretched double exponential in bend geometry) to obtain relative normalized amplitudes I_α and relaxation rates Γ_α ($\alpha = 1 - 3$), of the fluctuation modes. In the bend geometry, the analysis reveals an additional, weak mode Γ_4. In this case, the best single-exponential fit (the *dashed line*) clearly misses the data in the ($10^{-4} - 10^{-3}$) s region (*left inset*). The *right inset* shows the relaxation time spectrum obtained by the regularization method [26] for the bend geometry correlation function; the small secondary peak confirms the presence of the additional mode

Here g is the optical coherence factor [25]. For geometry "1&2", $\alpha = 1, 2$, the splay and twist modes contribute separately to the total intensity; for geometry "3", $\alpha = 3$, from Eq. (4.4) only the bend mode should contribute to the total intensity. From $\Gamma_\alpha(\theta)$, we obtain the corresponding orientational viscosities as: $\eta_{splay} = K_1 q_\perp^2(\theta)/\Gamma_1(\theta)$, $\eta_{twist} = K_2 q_\perp^2(\theta)/\Gamma_2(\theta)$ and $\eta_{bend} = K_3 q_\parallel^2(\theta)/\Gamma_3(\theta)$.

4.3 Elastic Constants

The temperature and concentration dependences of the elastic moduli K_1, K_2 and K_3 of the nematic phase of DSCG are shown in Fig. 4.3. The splay constant K_1 and bend constant K_3 are comparable to each other, being on the order of 10 pN, while the twist constant K_2 is about 10 times smaller [confirming the estimate leading to Eq. (4.4)]. Similar values and large anisotropy were recently reported for another LCLC, Sunset Yellow [4]. All three elastic moduli increase as the temperature T decreases, but K_1 shows a much steeper dependence than that of K_2 and K_3. For example, for c = 18 wt%, K_1 increases by a factor of 9 within a $\sim$10 K temperature decrease, while K_2 increases only threefold and K_3 less than twofold. The temperature dependence of K_1 follows a universal exponential law for all concentrations

$$K_1(T) \propto \exp(-\beta_K T) \tag{4.7}$$

where β_K = 0.20 $\pm$ 0.01 K^{-1} is independent of concentration, Fig. 4.3a inset.

The anisotropy of the elastic moduli is further illustrated in Fig. 4.4 where the ratios of elastic constants are plotted as a function of T for different concentrations. When T decreases, both K_1/K_3 and K_1/K_2 increase. K_3/K_2 remains practically constant (35 $\pm$ 5) over a wide temperature range for c = 12.5, 14, 16 wt%, whereas for c = 18 wt%, the value slightly decreases to about 25 at $T \approx 294$ K.

The elastic moduli of DSCG shows some unique features as compared to conventional thermotropic nematics such as 5CB and to other nematic lyotropic LC systems, including the LCLC SSY and nematic polymeric LCs such as poly (γ-benzyl glutamate) (PBG), Table 4.1. First, the anisotropy of the elastic constants of DSCG is the largest among all the representative nematics shown in Table 4.1. It is not only distinctively different from thermotropic LCs such as 5CB, but also makes the record in lyotropic systems such as SSY and PBG. Second, K_1 has a much stronger (exponential) temperature dependence as compared to the linear dependences of K_2 and K_3. In thermotropic LC 5CB, the temperature dependences of elastic moduli is much weaker [22–24].

We now proceed to discuss our results in terms of relevant theoretical models for the elastic properties of lyotropic nematics.

The viscoelasticity of lyotropic systems is usually described by the Onsager type models [13, 27–29] based on the idea of excluded volume. In the simplest version, the building units are considered as long slender rods with the length-to-diameter ration L/D being fixed and much larger than 1. The nematic ordering is caused by

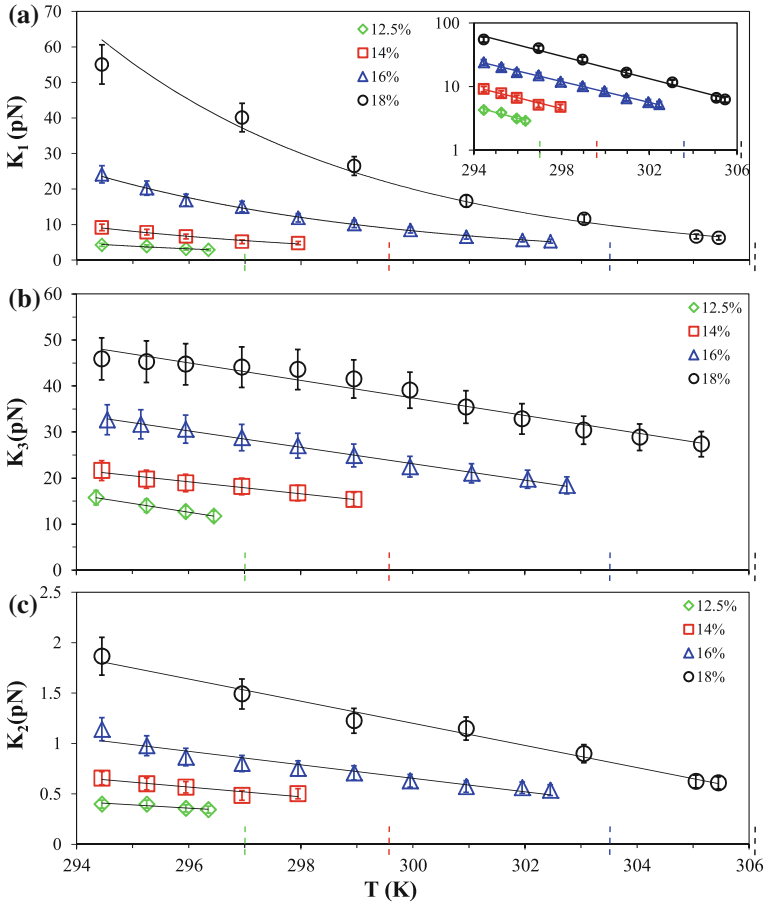

Fig. 4.3 Temperature and concentration dependences of elastic constants of **a** splay K_1, **b** bend K_3 and **c** twist K_2 in nematic phase. *Dashed vertical lines* on the horizontal axes indicate the transition temperature from nematic to nematic-isotropic coexistence phase. The *inset* shows K_1 has an exponential dependence of temperature T. K_3 and K_2 fit well with linear functions of temperature T

the increase of concentration; the rods sacrifice orientational freedom to maintain the ability to translate. The model is athermal as the behaviour is controlled exclusively by entropy. The excluded volume theory predicts the elastic constants in a system of rigid long rods [28] as follows: $K_1 = \frac{7}{8\pi}\frac{k_BT}{D}\phi\frac{L}{D}$, $K_2 = K_1/3$ and $K_3 = \frac{4}{3\pi^2}\frac{k_BT}{D}\phi^3\left(\frac{L}{D}\right)^3$. Clearly, this model does not describe our experimental findings for the LCLC system well. For example, the measured K_1/K_2 can be as high as $\sim$30 (c = 18 wt%, $T \approx 294$ K), Fig. 4.4b, much larger than the expected constant value of 3. Furthermore, to form a nematic phase, the system of rigid rods should be of a volume fraction that exceeds a critical value $\phi_c = 4.5D/L$ [21]. If that is the

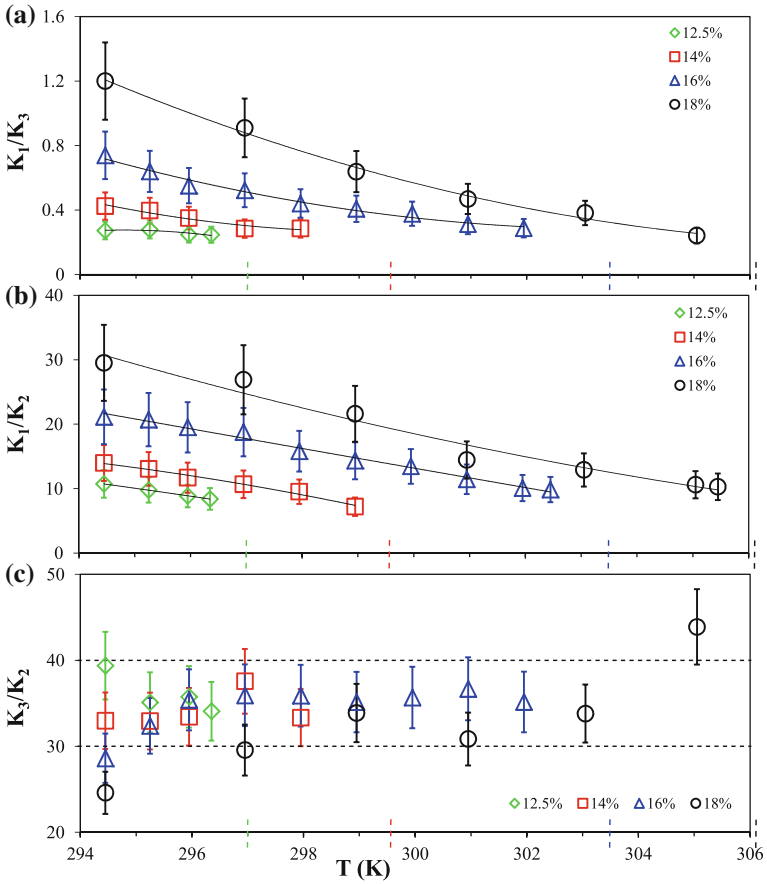

Fig. 4.4 Temperature and concentration dependences of the ratios between elastic constants. **a** K_1/K_3, **b** K_1/K_2 both increase as T decreases or ϕ increases; **c** K_3/K_2 remains practically constant for a wide range of T, but decreases at $T \approx 294$ K for 18 wt%

Table 4.1 Viscoelastic parameters of different liquid crystals

LCs	K_1 (pN)	K_2 (pN)	K_3 (pN)	η_{splay} (kgm^{-1} s^{-1})	η_{twist} (kgm^{-1} s^{-1})	η_{bend} (kgm^{-1} s^{-1})
DSCG	10.2	0.7	24.9	11.7	10.5	0.009
SSY	7.4	0.8	8.9	–	0.271	–
PBG	7.5	0.6	6	2.5	2.5	0.025
5CB	4.5	3	5.5	0.088	0.094	0.015

LCLC DSCG: 16 wt%, $\phi = 0.115$, $\Delta T = 4.3$ K; LCLC SSY: 30.5 wt%, $\phi = 0.20$, $\Delta T = 6.4$ K; lyotropic polymeric LC PBG: $L/D = 32$, $\phi = 0.16$; thermotropic LC 5CB: $\Delta T = 4$ K

case, then one would expect $\frac{K_3}{K_1} \approx \frac{1}{2}\phi^2\left(\frac{L}{D}\right)^2 > 10$, while our experiment yields a much lower value $\frac{K_3}{K_1} \sim (1-3)$ in nematic DSCG, Fig. 4.4a.

To explain the smallness of K_2, one may consider effects such as the electrostatic interaction of charged rods [27], since the dissociation of ionic groups into water from the periphery of the DSCG aggregates makes them charged. However this correction turns out to be negligible. Coulomb repulsion of similarly charged cylinders tends to arrange them perpendicularly to each other. This "twisting effect" thus modifies K_2 by a factor [27]$\approx (1-0.1h)$, where $h = \lambda_D/(D+2\lambda_D)$, $D \approx$ 1.6 nm is the "bare" diameter of DSCG aggregates [19] and λ_D is the Debye screening length. For the DSCG solutions used in this work, $\lambda_D \approx 0.5$ nm [30]. Therefore, the twisting effect might lead to a decrease of K_2 by only a few percent, and is most likely not the main reason for the observed smallness of K_2. The situation is very similar to the one for LCLC Sunset Yellow [4], discussed in Chaps. 2–3.

The next level of theoretical modelling is to take into account that the aggregates comprising the LCLC are not absolutely rigid but possess some flexibility [11, 28, 29], characterized by a finite persistence length λ_p, that should directly affect K_3. The persistence length is a measure of the length scale over which the unit vectors tangential to the flexible elongated object lose their correlations. Flexibility of LCLC aggregates is evident in recent numerical simulations [31, 32] and suggested by recent nuclear magnetic resonance measurements, where column undulation within the molecular stack involving 4–8 molecules was observed [33].

When the aggregates are flexible, the bend deformation is no longer inhibited by their length; each aggregate can bend to follow the director pattern, Fig. 4.5a. According to the well-known result of the elastic theory [34, 35], the bending energy of an elastic rod is $F_3 = \frac{1}{2}\kappa L\rho^2$, where κ is the bending stiffness and ρ is the curvature of the bent rod. The volumetric elastic energy density for a dispersion of elastic rods is then [13] $f_3 = F_3\phi\left(\frac{\pi}{4}D^2L\right)^{-1}$. Using the relationships between the persistence length λ_p and bending stiffness [34], $\lambda_p = \kappa/k_BT$, and between the energy density of bend and K_3, $f_3 = \frac{1}{2}K_3\rho^2$, one arrives at

$$K_3 = \frac{4}{\pi}\frac{k_BT}{D}\phi\frac{\lambda_p}{D} \tag{4.8}$$

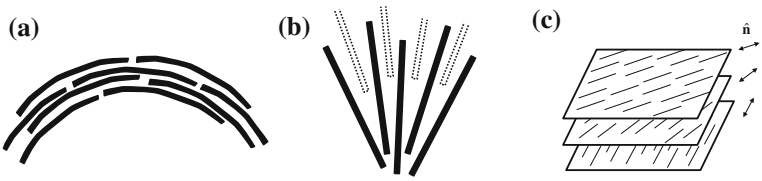

Fig. 4.5 Mechanism of elastic deformation in LCLC, following Meyer et al. [15]. **a** Flexible rods accommodate bend deformation by deforming the rods. **b** Splay deformation tends to create vacancies that require free ends (marked by *dashed lines*) to fill in. **c** Twist deformation causes minimum inter-aggregates interference by arranging aggregates in layers

The last result is twice as large as the expression derived by Taratuta et al. [13], who defined λ_p as $\frac{2\kappa}{k_BT}$. Equation (4.8) with the typical experimental values K_3 = 10 pN, ϕ = 0.1 and D = 1.6 nm [19] yields an estimate λ_p = 50 nm. This value is close to the persistence length of double-stranded DNA (dsDNA) [36], which has structural parameters similar to the aggregate of DSCG (diameter ~2 nm and 6 ionizable groups per 1 nm of length).

The value of K_3 for DSCG at $\phi \approx 0.1$ is several times larger than the value K_3 = 6.1 pN reported for SSY[4] with $\phi \approx 0.20$, Table 4.1. To discuss the difference, it is convenient to represent the bending stiffness of the chromonic aggregate through the Young's modulus Y of a homogeneous elastic cylinder [34]: $\kappa = \pi Y D^4/64$. Therefore,

$$K_3 = \frac{\phi Y D^2}{16} \tag{4.9}$$

The aggregates in the DSCG LCLC have a larger cross section [37] ($D^2 \sim 2.4$ nm^2) than those for SSY [37] ($D^2 \sim 1.2$ nm^2), so that the product ϕD^2 in Eq. (4.9) is essentially the same for the two LCLCs. Hence, the difference in the values of K_3 can be attributed to the difference in the Young modulus Y, which is worthy of further investigation. When K_3 = 10 pN, Eq. (4.9) leads to $Y = 6.7 \times 10^8$ N/m^2, which is the same order of magnitude as the sequence dependent Young's modulus for dsDNA [38] (for example, $Y \approx 3 \times 10^8$ N/m^2 for the λ-phage dsDNA [39]).

The flexibility of aggregates does not affect the splay constant K_1 much. As explained by Meyer [15], splay deformations, under the condition of constant density, limit the freedom of molecular ends, which decreases the entropy, Fig. 4.5b. A larger contour length L implies a smaller number of molecular ends available to accommodate for splay and thus a higher K_1 [13]:

$$K_1 = \frac{4}{\pi}\frac{k_BT}{D}\phi\frac{\overline{L}}{D} \tag{4.10}$$

Here we introduced a new notation $\overline{L}$ for the characteristic (average) length of aggregates. Using this expression and the values of K_1 = 5 pN, ϕ = 0.1, D = 1.6 nm for c = 14 wt% DSCG at T = 297 K (3 K below T_{ni}), we find $\overline{L} \approx$ 25 nm, which compares well with a previous estimate [40] $\overline{L}$ = 18 nm for the isotropic phase of the same concentration at 305 K (5 K above T_{ni}).

The twist elastic constant in the model of flexible rods is predicted to be [28]

$$K_2 = \frac{k_BT}{D}\phi^{1/3}\left(\frac{\lambda_p}{D}\right)^{1/3} \tag{4.11}$$

implying a rather weak dependency on λ_p and ϕ. The smallness of K_2 and its independence of the contour length $\overline{L}$ in LCLCs can be explained as follows[15],

Fig. 4.5c. Consider an ideal arrangement of the aggregates in layers to accommodate a twisted director field. Within each layer, the aggregates are straight and closely packed; the direction of director is changed by a small angle only when moving between consecutive layers. Successive layers of aggregates simply stack on top of each other to form a twisted nematic distortion with $\hat{\mathbf{n}}\perp$ helical axis. However, in reality, the aggregates cannot perfectly remain in the layers; for example, thermal fluctuations will displace the aggregates across layers and thus cause them to interfere with aggregates that have a different orientation. This interference can be relieved by bending the aggregates to conform to the local orientational order in the layer, instead of being aggravated by the extended aggregate length. Thus K_2 is independent of $\overline{L}$ and weakly dependent on λ_p (as compared to the bend elasticity K_3). From Eqs. (4.8) to (4.11), for typical values ϕ = 0.1, λ_p = 50 nm, D = 1.6 nm, we deduce $\frac{K_2}{K_3} = \frac{\pi}{4}\left(\phi\frac{\lambda_p}{D}\right)^{-2/3} \approx 0.37$, which qualitatively agrees with our argument that K_2 has weak dependence on λ_p, but still does not quantitatively explain the smallness of the observed ratio (K_2/K_3 in the range of 0.025–0.04 for all concentrations and temperatures). Clearly, an improved theory is needed.

Similarly to our previous study of SSY [27], and the ratio in DSCG decreases as the temperature increases, Fig. 4.4. As follows from Eqs. (4.8) and (4.10) for the model of flexible aggregates, the ratio is:

$$\frac{K_1}{K_3} = \frac{\bar{L}}{\lambda_p} \tag{4.12}$$

The observed temperature dependence of K_1/K_3 cannot be explained by the Onsager-type models either for rigid rods or for flexible rods, if the mean aggregate length $\overline{L}$ remains constant. Instead, as we now argue, different temperature dependences of the aggregate contour length $\overline{L}$ and persistence length λ_p are responsible, a possibility which is absent in LCs with a fixed, temperature-independent shape of building units.

Consider $\overline{L}$ first. Theoretical works suggest that $\bar{L}$ depends on volume fraction ϕ, temperature T and scission energy E_a [4, 15, 37, 41, 42]. Compared to the expression for $\bar{L}$ in a dilute ($\phi \ll 1$) isotropic phase, $\overline{L} = L_0\sqrt{\phi}\exp\left(\frac{E_a}{2k_BT}\right)$, the form of $\bar{L}$ in the nematic state exhibits a stronger dependence on ϕ due to the orientational order [4]:

$$\overline{L} = L_0\phi^{5/6}\left(\frac{\lambda_p}{D}\right)^{1/3}\exp\left(\frac{E_a+\sigma\phi}{2k_BT}\right) \tag{4.13}$$

Here $L_0 = 2\pi^{-2/3}\sqrt{a_z D}$ is a length characterizing the size of a monomer, a_z the period of molecular stacking along the aggregate, and σ a constant describing the enhancement of aggregation by the excluded volume effects. (In the second virial

approximation [43], $\sigma \approx 4k_BT$.) For DSCG, D = 1.6 nm, a_z = 0.34 nm [44], L_0 = 0.7 nm. Using Eq. (4.10) for K_1, we estimate that $\bar{L}$ is in the range of (20–270) nm, and $E_a(\phi, T) \approx (8-14)k_BT$, close to the estimates for SSY LCLC by Collings et al. [45], $E_a \approx 7k_BT$, and by Day et al. [46], $E_a \approx 11k_BT$, and for DNA oligomers [36] by Clark et al. $E_a \approx (4-8)k_BT$. To make contact with the empirical expression above for K_1 in Eq. (4.7), we expand $\frac{E_a(\phi,T)}{k_BT}$ near $T_{ni} \approx 300$ K as follows:

$$\frac{E_a(\phi,T)}{k_BT} = \frac{E_a(\phi,T_{ni})}{k_BT_{ni}} - \left(\frac{E_a}{k_BT} - \frac{\partial E_a}{k_B\partial T}\right)_{T_{ni}} \frac{1}{T_{ni}}(T-T_{ni}) + O(T-T_{ni})^2 \quad (4.14)$$

This gives (to lowest order in $T - T_{ni}$):

$$\bar{L} \propto \exp\left[-\left(\frac{E_a}{k_BT} - \frac{\partial E_a}{k_B\partial T}\right)\Big|_{T_{ni}} \frac{T}{2T_{ni}}\right] \quad (4.15)$$

Inserting this result into Eq. (4.10) and comparing it to Eq. (4.7), we identify $\beta_K = \frac{1}{2T_{ni}}\left(\frac{E_a}{k_BT} - \frac{\partial E_a}{k_B\partial T}\right)\Big|_{T_{ni}}$. Then using the experimental value of $\beta_K = 0.2 \pm 0.01$ K^{-1} and the above estimates for $E_a(\phi,T)/k_BT \sim 10$, we find:

$$\left.\frac{\partial E_a}{k_B\partial T}\right|_{T_{ni}} = \frac{E_a}{k_BT_{ni}} - 2\beta_K T_{ni} < 0 \quad (4.16)$$

and therefore conclude that $E_a(\phi, T)$ decreases with increasing T.

As shown by numerical simulations [32], the persistence length λ_p scales with ϕ and T as $\frac{\lambda_p}{L_0} \propto \frac{E_a(\phi,T)}{k_BT}$, and thus has a much weaker dependence on ϕ (mainly through ionic effects) and T than does $\bar{L}$ for chromonic aggregates formed by cylindrical monomers. From Eqs. (4.8), (4.10), and (4.13), we can deduce

$$\frac{K_1}{K_3} \propto \phi^{5/6} \exp\left(\frac{E_a + \kappa\phi}{2k_BT}\right)\left(\frac{E_a}{k_BT}\right)^{-2/3} \quad (4.17)$$

This equation implies that $\frac{K_1}{K_3}$ decreases when T increases or ϕ decreases, consistent with our measurements, Fig. 4.4a. Our experimental values of $\frac{K_1}{K_3}$ suggest that $\frac{\bar{L}}{\lambda_p}$ is in the range of (0.25–1.2), depending on T and ϕ. Interestingly, the numerical results of Kuriabova et al. [32], $L/\lambda_p \approx 1$, fall in this range.

The exponential dependence of K_1 on $\frac{E_a}{k_BT}$ and the weak dependence of K_2 on λ_p, Eq. (4.11), predict that $\frac{K_1}{K_2} \propto \phi^{3/2} \exp\left(\frac{E_a + 2\kappa\phi}{k_BT}\right)$ increases when T decreases or ϕ decreases, again consistent with our measurements, Fig. 4.4b. Regarding $\frac{K_3}{K_2}$,

Eqs. (4.8) and (4.11) indicate $\frac{K_3}{K_2} \propto \phi^{2/3}\left(\frac{\lambda_p}{D}\right)^{2/3} \propto \phi^{2/3}\left(\frac{E_a}{k_B T}\right)^{2/3}$. As temperature T decreases (ΔT increases), λ_p and $\frac{E_a}{k_B T}$ increase, thus $\frac{K_3}{K_2}$ should increase. However, experiments show that $\frac{K_3}{K_2}$ remains practically constant over a wide range of temperature for all studied ϕ, and that in fact it decreases at $T \approx 294$ K for the highest volume fraction $\phi = 0.129$ ($c = 18$ wt%), Fig. 4.4c. Apparently, some additional factor must account for this behaviour. One possibility is the following. For the c = 18 wt% sample at $T \approx 291$ K (3 K below our experimental range), the system transforms into a columnar phase [19]. In this phase, twist deformations are severely inhibited by the hexagonal packing of the long aggregates, and consequently $K_2 \to \infty$ is expected. A pretransitional increase of K_2 would explain the decrease in $\frac{K_3}{K_2}$ seen at low temperatures in Fig. 4.4c.

4.4 Viscosities

The concentration and temperature dependences of viscosities η_{splay}, η_{twist} and η_{bend} are shown in Fig. 4.6. The viscosities η_{splay} and η_{twist} are comparable to each other and are in the range of (1–500) $\mathrm{kgm^{-1}\,s^{-1}}$, several orders of magnitude larger than $\eta_{bend} = (0.007 - 0.03)$ $\mathrm{kgm^{-1}\,s^{-1}}$. η_{splay} and η_{twist} show very strong temperature dependences, changing by over two orders of magnitudes when the temperature changes by only about 10 K, Fig. 4.6a, b. For the same temperature range, η_{bend} changes by a factor of 3 only, Fig. 4.6c. The temperature dependence of η_{splay} and η_{twist} are described by the exponential laws

$$\eta_{splay}(T) \propto \exp(-\beta_s T), \quad \eta_{twist}(T) \propto \exp(-\beta_t T) \tag{4.18}$$

where the concentration independent coefficients are $\beta_s = 0.41 \pm 0.02$ $\mathrm{K^{-1}}$, $\beta_t = 0.37 \pm 0.01$ $\mathrm{K^{-1}}$. Note that β_s and β_t are roughly twice as large as β_K.

The ratio $\eta_{splay}/\eta_{twist}$ slowly increases with T, Fig. 4.6d. In the vicinity of nematic to nematic-isotropic biphasic transition (low concentrations or small ΔT), $\eta_{splay}/\eta_{twist}$ remains close to 1 within the accuracy of experiments. Deeper into the nematic phase (and specifically for the highest concentration $c = 18$ wt% and for $\Delta T \approx 12$ K), $\eta_{splay}/\eta_{twist}$ increases to about 2.

Table 4.1 compares the viscosity of DSCG to other lyotropic nematics (PBG, SSY) and thermotropic LC (5CB). The large values of the splay and twist viscosities measured in the DSCG LCLC, and the relatively small value of the bend viscosity, can be understood following the arguments put forward by de Gennes [47] and Meyer [11, 12, 14, 15] for nematic LC polymers in the "infinite" chain limit, $\bar{L}/D \to \infty$. In this limit, twisting the director field is associated with mass displacement of single chains, which produces flows perpendicular to the director with a gradient along the director. If the chains are not allowed to break, twist

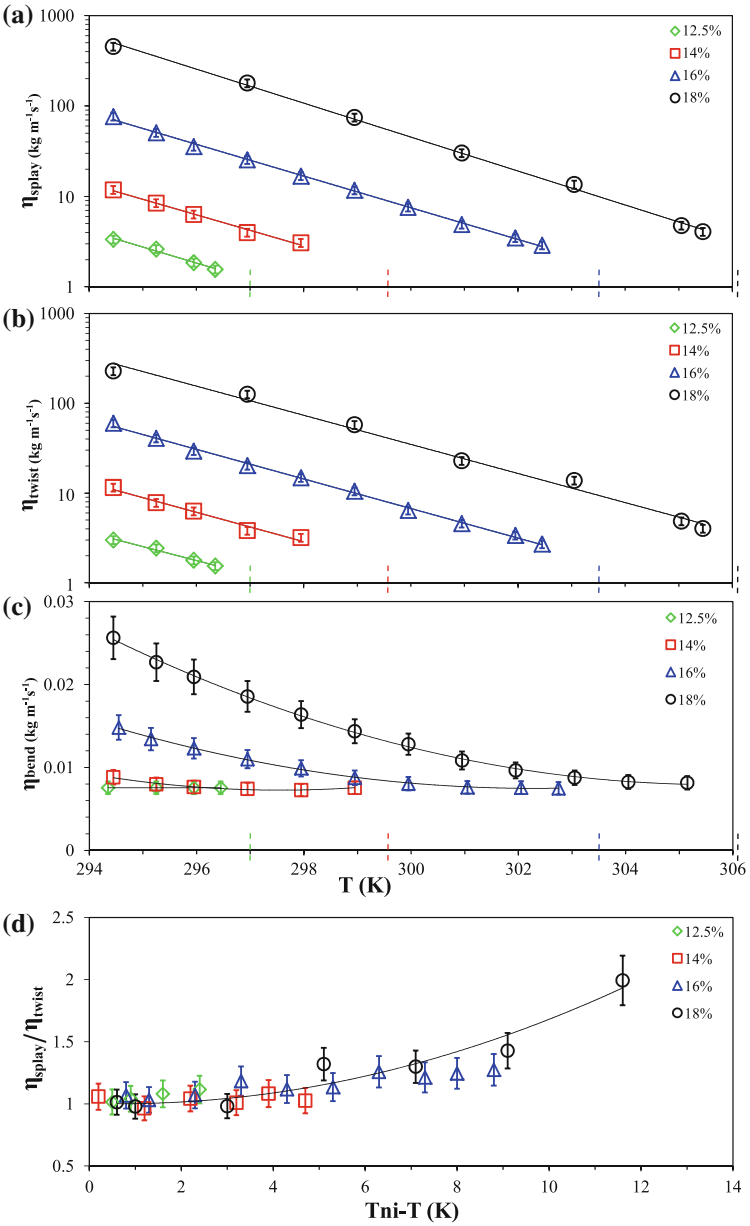

Fig. 4.6 Temperature and concentration dependences of viscosities and their ratios: **a** η_{splay}, **b** η_{twist}, **c** η_{bend} and **d** $\eta_{splay}/\eta_{twist}$ over the nematic range. *Dashed lines* in the horizontal axis indicate T_{ni}

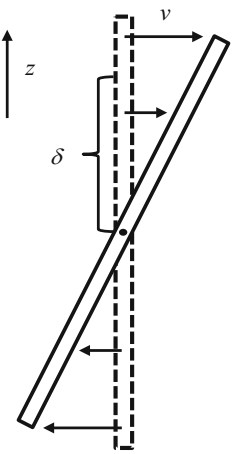

Fig. 4.7 An aggregate of LCLC rotates in a transverse shear flow, as one can find in a twist deformation, following Meyer et al. [15]

deformation, even though conceptually possible as a static state as we argued earlier, is forbidden as a dynamic process since it induces flows that tend to cut the chains; as a result $\eta_{twist} = \gamma_1 \to \infty$, where γ_1 is the rotation viscosity of the director field [21]. In a practical system with a finite (but still large) $\bar{L}/D \gg 1$, η_{twist} must increase as $\bar{L}$ increases. A simple geometric argument due to Meyer [14, 15] shows that $\eta_{twist} = \gamma_1 \propto \bar{L}^2$, Fig. 4.7. Consider a twist deformation that induces shear flow $\frac{\partial v}{\partial z} = \text{const}$. The power dissipated per monomer along the aggregates is $P = \mu\delta^2\left(\frac{\partial v}{\partial z}\right)^2$, where μ is a friction coefficient and δ is the distance of the monomer to the rotation centre. The mean power dissipation $\bar{P} = \frac{1}{\bar{L}}\int_{-\bar{L}/2}^{\bar{L}/2} P dz = \mu\frac{\bar{L}^2}{12}\left(\frac{\partial v}{\partial z}\right)^2$; thus the effective viscosity for the twist process is $\eta_{twist} \propto \bar{L}^2$. A similar analysis applies to splay deformation, giving $\eta_{splay} \propto \bar{L}^2$. These predictions are consistent with our experimental results for the η's and with the linear dependence $K_1 \propto \overline{L}$. Namely, as indicated in Figs. 4.3a and 4.6a, b: $K_1 \propto \exp(-\beta_K T)$ with $\beta_K = 0.20 \pm 0.01\ \ \mathrm{K}^{-1}$; $\eta_{twist} \propto \exp(-\beta_t T)$ with $\beta_t = 0.37 \pm 0.01\mathrm{K}^{-1}$; and $\eta_{splay} \propto \exp(-\beta_s T)$ with $\beta_t = 0.41 \pm 0.02\mathrm{K}^{-1}$. The result $\beta_t \approx \beta_s \approx 2\beta_K$ agrees with the theoretical scaling relations, $K_1, \eta_{splay}^{1/2}, \eta_{twist}^{1/2} \propto \overline{L}$, and the temperature dependence of the viscoelastic parameters predicted by Eq. (4.15) in the vicinity of T_{ni} is also confirmed.

The viscosity associated with bend deformation, η_{bend} is comparable to values for thermotropic LCs, Table 4.1, and is several orders of magnitude smaller than η_{splay} and η_{twist}. This is explained by the fact that bend deformation is associated with "sliding" the aggregates parallel to each other [12–15], which is not inhibited even if $\bar{L}/D$ becomes very large.

An important difference in the hydrodynamic properties of LCLCs relative to those of low-molecular LCs is illustrated in Fig. 4.6d, which shows the temperature

dependence of $\eta_{splay}/\eta_{twist}$. In DSCG, this ratio is close to but still somewhat larger than 1. The result is unusual from the point of view of the Ericksen-Leslie model [21], in which the twist viscosity $\eta_{twist} = \gamma_1$ is always larger than splay viscosity $\eta_{splay} = \gamma_1 - \frac{\alpha_3^2}{\eta_b}$. (Here α_3 is one of the Ericksen-Leslie coefficients [21], and $\eta_b > 0$ is one of the Miezowicz viscosities [21].) Our experimental results, Fig. 4.6d, however, show that $\eta_{splay}/\eta_{twist} \approx 1$ holds only in the vicinity of the transition to the isotropic phase. When ΔT increases and the system moves deeper into nematic phase, $\eta_{splay}/\eta_{twist}$ can be as larger as 2. This finding suggests that the explanation of the anomalous behaviour seen in Fig. 4.6d is again rooted in the strong temperature and concentration dependencies of the mean aggregate length $\bar{L}$.

4.5 An Additional Mode in Bend Geometry

As indicated by Eqs. (4.1) and (4.6), two modes, namely pure splay and pure twist, contribute separately to the total intensity in the "1&2" scattering geometry. The corresponding correlation function should reveal two relaxation processes with $\Gamma_1(\theta) = \frac{K_1 q_\perp^2(\theta)}{\eta_{splay}}$, $\Gamma_2(\theta) = \frac{K_2 q_\perp^2(\theta)}{\eta_{twist}}$. This is indeed what we obtain by fitting experimental data, as indicated in Fig. 4.2. On the other hand, Eqs. (4.4) and (4.6) predict that bend fluctuations contribute to the intensity in geometry "3", and thus the correlation function should show a single relaxation process with $\Gamma_3(\theta) = \frac{K_3 q_\parallel^2(\theta)}{\eta_{bend}}$. However, fitting the experimental data with a single exponential decay fails to match the data, Fig. 4.2. A minimum of two relaxation modes, with a stretching exponent $b = 0.9$, are needed to fit the correlation data:

$$\langle I(0,\theta)I(\tau,\theta)\rangle = \bar{I}^2(\theta) + g^2\left[\bar{I}_3(\theta)\exp(-\frac{K_3 q_\parallel^2}{\eta_{bend}}\tau)^b + \bar{I}_4(\theta)\exp(-\Gamma_4\tau)^b\right]^2 \quad (4.19)$$

Fits of the data in geometry "3" to Eq. (4.19) indicate $\Gamma_4 \propto q_\parallel^2$, thus the additional mode is hydrodynamic. The fact that b is close to 1 implies that the relaxation rates do not have single values but show narrow dispersion [48]. Since $I_4/I_3 \approx 0.1$, the presence of the additional mode does not increase the uncertainty in the values deduced for K_3 and η_{bend} by more than 10%; the other viscoelastic parameters (measured in geometry "1&2") are unaffected.

By examining the additional fluctuation mode ($\bar{I}_4$, Γ_4) detected in the bend scattering geometry, we found that the key features of this mode are: (1) it is hydrodynamic ($\Gamma_4 \propto q_\parallel^2$); (2) it couples weakly to light ($\bar{I}_4$ is about 10 times smaller than $\bar{I}_3$ for the director bend mode); and (3) it is ~ 10 times slower than the bend fluctuations but $\sim 10^2$–10^3 times faster than splay or twist.

We propose that the additional mode is associated with the thermal diffusion of structural defects in the chromonic aggregates. To establish this conjecture, we point out the following. The plank-like chromonic molecules tend to aggregate face-to-face, to shield the exposure of extended aromatic cores to water. The scission energy E_a of this non-covalent association is about 10 k_BT as shown in our analysis above and references [36, 45, 46]. The molecular association might therefore form metastable configurations that do not correspond to the absolute minimum of the interaction potential. For example, the association might happen with a lateral shift or rotation of the molecular planes. Some of these defects or their combinations alter the aggregate structure so significantly that they impose deformations on the surrounding director field. As illustrated in Fig. 4.8, a pair of lateral shifts, which we call a "C" defect, tends to impose a bend deformation ($\hat{\mathbf{n}} \times \text{curl}\, \hat{\mathbf{n}}$) on the director $\hat{\mathbf{n}}$. A sequence of such "C" defects can be pictured as a crankshaft. On the other hand, a junction of three aggregates, with the symmetry of the letter "Y", creates a different type of defect that imposes a splay distortion ($\hat{\mathbf{n}}$ div $\hat{\mathbf{n}}$) on the director field, Fig. 4.8. The presence of both defect types has already been suggested to explain a discrepancy between the length of chromonic aggregates expected from the point of view of the Onsager model of lyotropic mesomorphism and the length inferred from X-ray scattering data [44]. Interestingly, recent structural studies of sunset yellow support the existence of stacking features in the form of lateral shifts [49].

The stacking defects illustrated in Fig. 4.8 are polar. To incorporate their thermal diffusion into a description of the orientational fluctuation modes, we let the j-th type of polar defect be described by the vector density $\mathrm{v}_j(\mathrm{r})$. For example, j = 1 for

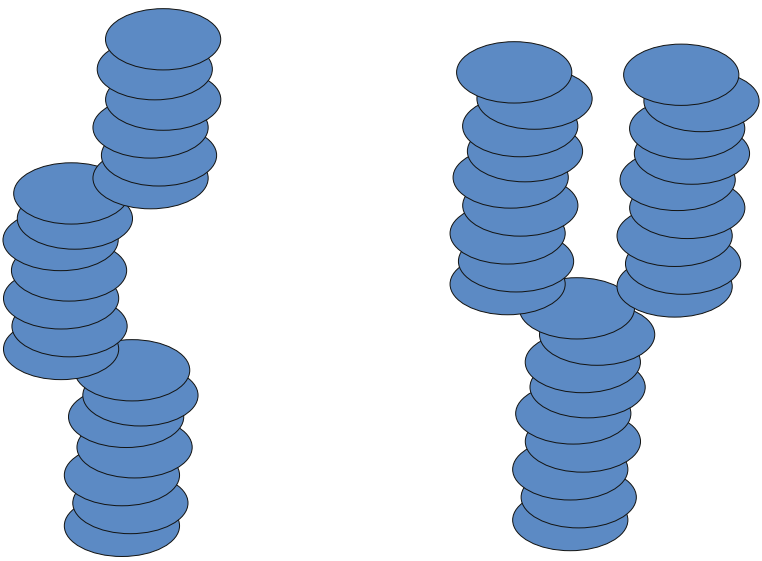

Fig. 4.8 "C"- (*left*) and "Y"-type (*right*) stacking defects in chromonic aggregates

"C" type, and j = 2 for "Y" type, Fig. 4.8. The effect of the defect dynamics on the light scattering is caused by their interaction with director distortions. This interaction, which may be termed flexopolarity, results in additional symmetry-allowed cross terms in the Frank elastic free energy. These terms couple the distortion vector $\mathbf{G}(\mathbf{r}) = g_s\hat{\mathbf{n}}div\hat{\mathbf{n}} + g_b(\hat{\mathbf{n}} \times curl\hat{\mathbf{n}})$, where g_s and g_b are splay and bend flexopolar coefficients, respectively, to the vector density v_j. Additionally, in the free energy we must consider an interaction between defects that penalizes fluctuations in their concentration. Generally, this may be expressed by a tensor coupling of the form $v \cdot h \cdot v$, where the tensor core $h_{jk}(\mathbf{r} - \mathbf{r}')$ defines the energy penalty for the polar defect densities and also ensures positivity of the free energy. To simplify the analysis, we neglect the interaction between different defect types and thus take $h_{jk}(\mathbf{r} - \mathbf{r}') = h_j(\mathbf{r} - \mathbf{r}')\delta_{jk}$. Based on these considerations, the free energy becomes:

$$F = \int \left[f_{FO} + \sum_j \mathbf{v}_j(\mathbf{r}) \cdot \mathbf{G}(\mathbf{r}) \right] d\mathbf{r} + \frac{1}{2} \int \sum_j \mathbf{v}_j(\mathbf{r}) \cdot h_j(\mathbf{r} - \mathbf{r}') \cdot \mathbf{v}_j(\mathbf{r}') d\mathbf{r} d\mathbf{r}' \tag{4.20}$$

where $f_{FO} = \frac{1}{2}\left[K_1(div\hat{\mathbf{n}})^2 + K_2(\hat{\mathbf{n}} \cdot curl\hat{\mathbf{n}})^2 + K_3(\hat{\mathbf{n}} \times curl\hat{\mathbf{n}})^2\right]$ is the standard Frank-Oseen bulk elastic energy [21].

Using the Fourier transform $\mathbf{v}_j(\mathbf{r}) = V^{-1}\sum_{\mathbf{q}} \mathbf{v}_j(\mathbf{q}) \exp(i\mathbf{q} \cdot \mathbf{r})$ and the standard quadratic representation for director fluctuation modes around the equilibrium director $\hat{\mathbf{n}}_0$, $\hat{\mathbf{n}}(r) = \hat{\mathbf{n}}_0 + V^{-1}\sum_{\mathbf{q}} \sum_{\alpha=1,2} n_\alpha(q)\, \hat{\mathbf{e}}_\alpha \exp(i\mathbf{q} \cdot \mathbf{r})$ in the frame $\{\hat{\mathbf{e}}_1, \hat{\mathbf{e}}_2, \hat{\mathbf{n}}_0\}$, where $\mathbf{q} = q_\perp\hat{\mathbf{e}}_1 + q_\parallel\hat{\mathbf{n}}_0$, we obtain:

$$\begin{aligned} F = \frac{1}{2V}\sum_{\mathbf{q}} \{ &\left(K_\alpha q_\perp^2 + K_3 q_\parallel^2\right)|n_\alpha(\mathbf{q})|^2 + 2ig_s q_\perp v_{j\parallel}^*(\mathbf{q}) n_1(\mathbf{q}) - \\ &2ig_b q_\parallel v_{j\alpha}^*(\mathbf{q}) n_\alpha(\mathbf{q}) + h_j^\parallel(\mathbf{q})\left|v_{j\parallel}(\mathbf{q})\right|^2 + h_j^\perp(\mathbf{q})\left|v_{j\alpha}(\mathbf{q})\right|^2\} \end{aligned} \tag{4.21}$$

where $v_j(\mathbf{q}) = v_{j1}\hat{\mathbf{e}}_1 + v_{j2}\hat{\mathbf{e}}_2 + v_{j\parallel}\hat{\mathbf{n}}_0$, summation is performed in Eq. (4.21) over indices j, and α = 1, 2 in the terms where they appear. Due to uniaxial anisotropy with respect to $\hat{\mathbf{n}}_0$, the tensors $h_j(\mathbf{q}) = \int h_j(\bar{\mathbf{r}} = \mathbf{r} - \mathbf{r}') \exp(-i\mathbf{q} \cdot \bar{\mathbf{r}}) d\bar{\mathbf{r}}$ are diagonal with components $h_j^\parallel(\mathbf{q})$ and $h_j^\perp(\mathbf{q})$ being parallel and perpendicular to $\hat{\mathbf{n}}_0$, respectively. We consider the polar defect mode $(j\beta)$,$\beta = 1, 2, \parallel$, as a 'fast' or 'slow' mode, depending on the magnitude of its relaxation rate $\Gamma_{j\beta}$ compared to the relaxation rate Γ_α^n of the director distortions $n_a(\mathbf{q})$.

Fast defect regime ($\Gamma_{j\beta} \gg \Gamma_\alpha^n$): When the director fluctuations are slow compared to the defect modes, their effect on the defect densities $v_{j\alpha}$ results in quasi-equilibrium values, $\tilde{v}_{j\alpha}(\mathbf{q}) = ig_b q_\parallel n_\alpha(\mathbf{q})/h_j^\perp(\mathbf{q})$ and $\tilde{v}_{j\parallel}(\mathbf{q}) = ig_s q_\perp n_1(\mathbf{q})/h_j^\parallel(\mathbf{q})$, determined by the minimization of F, Eq. (4.21), over $v_{j\alpha}^*(\mathbf{q})$ and $v_{j\parallel}^*(\mathbf{q})$. This "instantaneous"

response effectively renormalizes the elastic constants for 'spontaneous' director fluctuations

$$K_1 \rightarrow K_1 - \sum_j g_s^2/h_j^{\parallel}(\mathbf{q}), K_3 \rightarrow K_3 - \sum_j g_b^2/h_j^{\perp}(\mathbf{q}) \tag{4.22}$$

where the summation is over the fast defect modes. Except for this effect on the elastic moduli, "fast" defect modes are almost invisible in the DLS experiment probing director fluctuations. This fact is consistent with the lack of evidence for an additional, defect mode in the splay + twist scattering geometry, where the observed director fluctuations are much slower than either of the modes detected in the bend geometry.

Slow defect regime ($\Gamma_{j\beta} \ll \Gamma_{\alpha}^{n}$): Here the defect diffusion modes serve as a slowly changing random force field, that creates the quasi-equilibrium, defect-induced director distortions, obtained by minimizing F, Eq. (4.21), over $n_\alpha(\mathbf{q})$:

$$\tilde{n}_\alpha(q) = \sum_j \tilde{n}_\alpha^{(j)}(\mathbf{q}) = i \sum_j \frac{g_b q_\parallel v_{j\alpha}(\mathbf{q}) - g_s q_\perp v_{j\parallel}(\mathbf{q})}{K_\alpha q_\perp^2 + K_3 q_\parallel^2} \tag{4.23}$$

where the summation is over slow defect modes.

The bend scattering geometry, where the director mode is relatively fast, is the most favourable situation for directly observing fluctuations of $v_{j\beta}$, and is indeed the case where we do detect an extra mode. With $\alpha = 2$ (corresponding to the twist-bend director mode) and $q_\parallel \gg q_\perp$ (corresponding to nearly pure bend), we see from Eq. (4.23) that the diffusive modes v_{j2} couple to the director mode with coupling strength controlled by the parameter g_b. Even if v_{j2} fluctuations are slower than the bend fluctuations, their contribution to scattering can be weak, provided g_b is small, and thus agree with the behaviour observed experimentally for the additional mode ($\bar{I}_4$,Γ_4).

In principle, both translational and rotational diffusion of the polar defects could explicitly contribute to temporal variations of the defect density $\partial v_{j2}/\partial t$. However, when $q_\perp = 0$, the directions $\hat{\mathbf{e}}_1$ and $\hat{\mathbf{e}}_2$ in the plane perpendicular to $\hat{\mathbf{n}}_0$ are equivalent, v_{j2} and v_{j1} are degenerate, and rotational diffusion does not directly change the defect density that couples to the director mode. However, translational diffusion along $\hat{\mathbf{n}}_0$ can modulate v_{j2} (or v_{j1}) in regions of high or low bend distortion of the director. For $q = q_\parallel$ (as is essentially the case in the bend scattering geometry studied), we therefore expect a hydrodynamic mode with $\Gamma_{j2} \propto q_\parallel^2$, consistent with the experimental $\mathbf{q}$ dependence of Γ_4.

The fact that the stretching parameter b used in stretched exponential fits of the correlation functions in the bend geometry (Eq. (4.19)) is ~ 0.9 rather than 1 (pure exponential) indicates that both bend deformation and thermal diffusion of the configuration defects are associated with slightly dispersed instead of single valued relaxation rates Γ_3 and Γ_4. This could result from a geometric dispersion of stacking defects. Since the stacking of the DSCG molecules into aggregates is

isodesmic [41, 45], there is no obvious preference for certain geometrical parameters, such as the length of the arms of the "C" or "Y" defects, to prevail over others. As a result of dispersed geometric parameters of the stacking defects, we would expect some dispersion in relaxation rates $\Gamma_{j\beta}$ and Γ_{α}^{n} (Eq. (4.19) and Fig. 4.2).

4.6 Conclusions

We have measured the temperature and concentration dependences of the orientational elastic moduli and corresponding viscosities for the lyotropic nematic phase of a self-assembled LCLC system. Over the [3–10] K nematic temperature range of $c = (12.5 - 18)$ wt% DSCG LCLCs, $K_3 \approx K_1 \sim 10$pN, $K_2 \sim 1$pN, $\eta_{twist} \approx \eta_{splay} \sim$ (1–500) kgm^{-1}s^{-1} and $\eta_{bend} \approx 0.01$ kgm^{-1}s^{-1}. Of the three elastic constants, the splay constant (K_1) has the strongest temperature dependence, which is described by an exponential function of T. The twist and splay viscosities, η_{twist} and η_{splay} show similar exponential temperature dependences. We qualitatively explained these results by using the viscoelastic theory developed for LC systems formed by semi-flexible long chain particles with aspect ratio $\bar{L}/D \gg 1$ and by specifically confirming the predicted scaling of parameters, $K_1, \sqrt{\eta_{splay}}, \sqrt{\eta_{twist}} \propto \bar{L}$, with the strongly temperature-dependent average contour length $\bar{L}$. Our results demonstrating weak temperature dependence of the other parameters (K_2,K_3, and η_{bend}) also agree with theory. We detect an additional fluctuation mode in the bend geometry, which we attributed to the thermal diffusion of structural defects of the chromonic aggregates. These features, absent in conventional thermotropic LCs and lyotropic polymer LCs, highlight the fact that in LCLC system, the building units are non-covalently bound aggregates rather than molecules of fixed size.

4.7 Supplemental Information: Verification of K_1 and the Diamagnetic Anisotropy $\Delta\chi$ of DSCG

To verify the values of elastic constants from the DLS measurement, we measured K_1 of $c = 14.5$ wt% DSCG, using the technique of director reorientation in a magnetic field, as described in Sect. 2.3.2. The corresponding nematic-biphasic transition temperature of this concentration is $T_{N\rightarrow N+I} = 301$ K. The temperature dependence of K_1 of $c = 14.5$ wt% DSCG measured in the magnetic field falls between that of 14 and 16 wt% measured in DLS, Fig. 4.9, indicating a reasonable agreement of the results in both techniques. The concentration and temperature dependences of $\Delta\chi$ for DSCG, Fig. 4.9b, is measured using a super conducting quantum interference device, as described in Sect. 2.5.2.

4.8 A Summary of the Viscoelastic Properties of LCLCs

Through Chaps. 2–4, we explored the elasticity and viscosity of two LCLC materials, SSY and DSCG, in great details. A first common feature found in the LCLC systems is the anomalously large anisotropy of the elastic constants, namely, $K_3 \approx K_1 \approx 10K_2$, which was never seen in the low molecular weight thermotropic LCs. Obviously, the often-used one constant approximation ($K = K_1 = K_2 = K_3$) for theoretical consideration no longer holds in LCLCs. This changes our intuition when it comes to estimating the equilibrium director field in confined geometries, such as in droplets or capillaries, where strong deformation is imposed by the boundary conditions. Since K_2 is very small, elastic deformations of splay or bend type might be relieved by twist deformations with occurrence of chiral structures in molecularly non-chiral system. An experimental demonstration of such an effect caused by a small K_2 was presented for nematic tactoids of DSCG condensed by the osmotic pressure from an isotropic solution [50]. In these tactoids, the deformations of bend and splay are being partially replaced by twists. Since DSCG is not chiral, left- and right-handed tactoids are met with an equal probability. If the system

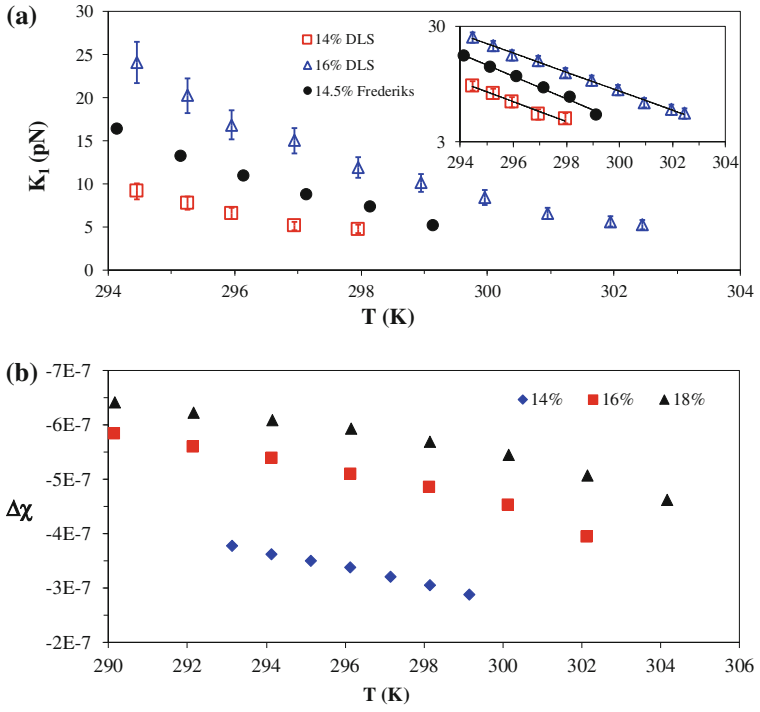

Fig. 4.9 Verification of K_1 value using the technique of director reorientation in a magnetic field (**a**) and the diamagnetic anisotropy $\Delta\chi$ of DSCG at various concentration and temperature (**b**). Note that $\Delta\chi$ is dimensionless in SI unit

contains a small amount of chiral molecules, this tactoids adopt the handedness of the additive, which allows one to use the effect for the detection and amplification of chiral molecules [51]. Furthermore, in cases of SSY droplets embedded in oil, the bipolar director field of the droplets are found to have over 90° twist [52] measured from the central line that connects the two poles. Similar super-twist of director was also found in cylindrical capillaries with planer anchoring [53–55]. These unusual observations were explained by the smallness of K_2, and also by the influence of the saddle-splay term in the Frank-Oseen free energy density with a constant K_{24} that was found to be extraordinary large, $K_{24} \approx (4-7)\,K_3$ for SSY [54, 55] and $K_{24} \approx (0.75-1.75)\,K_3$ for DSCG [55].

The anisotropy of the elastic constants is also found to cause a strong coupling between the director field and scalar order parameter field around topological defects (disclinations) [56] and at the isotropic-nematic boundaries [57]. In the traditional condensed matter theory for LCs, the phase (director $\hat{\mathbf{n}}$) and magnitude (scalar order parameter $\mathfrak{S}$) of the order parameter are usually treated as decoupled; the shape of the "melted" cores in the centre of the disclinations is thus cylindrical, independent on the azimuthal coordinate. We found in experiments that the core of disclinations and boojums in thin layers of DSCG have $2(1-m)$ number of cusps, where $m = \pm 1/2, \pm 1$ is the topological strength of the defect. Around these defects, both $\hat{\mathbf{n}}$ and S show radial and azimuthal dependences. We demonstrate that the smallness of K_2 as compared with K_1 and K_3 is connected to a large anisotropy of the coefficients in the Landau-de Gennes free energy density, $L_a \approx 40L_1$, which makes the spatial gradients of S, ∇S, dependent on the direction of change with respect to the direction of $\hat{\mathbf{n}}$. Namely, the gradients $\nabla S \perp \hat{\mathbf{n}}$ are about two times larger than the gradients $\nabla S \parallel \hat{\mathbf{n}}$. This anisotropy gives rise to the anisotropic shape of the defect cores and the strong coupling between $\hat{\mathbf{n}}$ and S.

The second common feature of the LCLCs is the enormously large rotational viscosities ($\gamma_1 \equiv \eta_{twist} = (1-500)\ \mathrm{kgm^{-1}s^{-1}} \approx \eta_{splay}$) as compared to a "normal" bend viscosity ($\eta_{bend} \approx 10^{-2}\ \mathrm{kgm^{-1}s^{-1}}$), usually measured in low molecular weight thermotropic LCs, Table 4.1. Because of this and also because of the anisotropy of elastic constants, the characteristic times of director relaxations through the bend, splay and twist modes are very different from each other, $\tau_{bend} \propto \frac{\eta_{bend}}{K_3} \ll \tau_{splay} \propto \frac{\eta_{splay}}{K_1} \ll \tau_{twist} \propto \frac{\eta_{twist}}{K_2}$. The bend mode, with τ_{bend} being the smallest among all three times, is thus most dynamically favourable. An illustration of this feature is the twist Frederiks transition under a suddenly applied external field. Instead of a direct transition from uniform planar to a uniform twist state, the system first develops periodic stripes involving large amount of bend deformation [4, 58, 59], Fig. 2.8. Then it takes some hours to relax into the uniform twist, since τ_{twist} is very large. As a comparison, in small molecule thermotropic LCs, the elastic and viscous constants of different mode are close to each other: $K_1 \approx K_2 \approx K_3 \approx 10\,\mathrm{pN}$, $\eta_{splay} \approx \eta_{twist} \approx \eta_{bend} \approx (10^{-2}-10^{-1})\,\mathrm{kgm^{-1}s^{-1}}$. As a result, the transient bend modes developing under similar experimental conditions relax into the twist state rather quickly, within milliseconds [58]. This distinctive dynamics of different modes in LCLCs is useful to identify director deformations

when direct measurements are difficult. For example, in the wake of a bacterium swimming perpendicularly to the director in a homeotropically aligned DSCG, the flagella bundle only agitates a local and short-living distortion. From the relaxation time scale, we conclude that the distortion is a mix of splay and bend, localized near the bacterium height, and diminishes without a chance to propagate to the entire sample thickness. As the LCLCs are finding their application as materials for polarizers [60], biosensors [7, 61], nanoparticle assembly templates [62], to hosting media of living organisms [10, 63–66], the knowledge of their viscoelastic properties can be very useful and critical.

References

1. Meyer RB et al (1985) Measurements of the anisotropic viscous and elastic properties of lyotropic polymer nematics. Faraday Discuss Chem Soc 79:125–132
2. Golovanov AV, Kaznacheev AV, Sonin AS (1995) Izvestiya Akad. Nauk Ser Fiz 59:82
3. Golovanov AV, Kaznacheev AV, Sonin AS (1996) Izvestiya Akad. Nauk Ser Fiz 60:43
4. Zhou S et al (2012) Elasticity of lyotropic chromonic liquid crystal probed by director reorientation in a magnetic field. Phys Rev Lett 109:037801
5. Nazarenko VG et al (2010) Surface alignment and anchoring transitions in nematic lyotropic chromonic liquid crystal. Phys Rev Lett 105(1):017801
6. Jeong J et al (2014) Homeotropic alignment of lyotropic chromonic liquid crystals using noncovalent interactions. Langmuir 30:2914–2920
7. Shiyanovskii SV et al (2005) Real-time microbe detection based on director distortions around growing immune complexes in lyotropic chromonic liquid crystals. Phys Rev E 71 (2):020702
8. Kuma A, Galstian T, Pattanayek SK, Rainville S (2013) The motility of bacteria in an anisotropic liquid environment. Mol Cryst Liq Cryst 574:33–39
9. Mushenheim PC, Trivedi RR, Tuson HH, Weibel DB, Abbott NL (2014) Dynamic self-assembly of motile bacteria in liquid crystals. Soft Matter 10:88–95
10. Zhou S, Sokolov A, Lavrentovich OD, Aranson IS (2014) Living liquid crystals. Proc Natl Acad Sci U S A 111(4):1265–1270
11. Taratuta VG, Hurd AJ, Meyer RB (1985) Light-scattering study of a polymer hematic liquid crystal. Phys Rev Lett 55:246
12. Lee S-D, Meyer RB (1990) Light scattering measurements of anisotropic viscoelastic coefficients of a main-chain polymer nematic liquid crystal. Liq Cryst 7(1):15–29
13. Taratuta VG, Lonberg F, Meyer RB (1988) Anisotropic mechanical properties of a polymer nematic liquid crystal. Phys Rev A 37:1831
14. Lee S-D, Meyer RB (1988) Crossover behavior of the elastic coefficients and viscosities of a polymer nematic liquid crystal. Phys Rev Lett 61:2217
15. Meyer RB (1982) Polymer liquid crystals. In: Ciferri A, Krigbaum WR, Meyer RB (eds). Academic Press, New York
16. Nastishin YA, Neupane K, Baldwin AR, Lavrentovich OD, Sprunt S (2008) Elasticity and viscosity of a lyotropic chromonic nematic studied with dynamic light scattering. Electron-Liq Cryst Commun
17. Nastishin YA, Neupane K, Baldwin AR, Lavrentovich OD, Sprunt S (2008) Elasticity and viscosity of a lyotropic chromonic nematic studied with dynamic light scattering. arXiv:0807.2669

18. Park HS, Lavrentovich OD (2012) Lyotropic chromonic liquid crystals: emerging applications. In: Li Q (ed) Liquid crystals beyond displays: chemistry, physics, and applications. Wiley, Hoboken, New Jersey, pp 449–484
19. Hartshor Nh, Woodard GD (1973) Mesomorphism in system disodium chromoglycate-water. Mol Cryst Liq Cryst 23(3–4):343–368
20. Nastishin YA et al (2005) Optical characterization of the nematic lyotropic chromonic liquid crystals: light absorption, birefringence, and scalar order parameter. Phys Rev E 72(4):041711
21. de Gennes PG, Prost J (1993) The physics of liquid crystals. Clarendon Press, Oxford, p 598
22. Karat PP, Madhusudana NV (1977) Elasticity and orientational order in some 4′-*n*-Alkyl-4-Cyanobiphenyls: part II. Mol Cryst Liq Cryst 40:239–245
23. Toyooka T, Chen G-P, Takezoe H, Fukuda A (1987) Determination of twist elastic constant K22 in 5CB by four independent light-scattering techniques. Jpn J Appl Phys 26:1959–1966
24. Cui M, Kelly JR (1999) Temperature dependence of visco-elastic properties of 5CB. Mol Cryst Liq Cryst 331:49–57
25. Berne BJ, Pecora R (1976) Dynamic light scattering. Wiley, New York
26. Provencher SW (1982) Comput Phys Commun 27:213–229
27. Vroege GJ, Odijk T (1987) Elastic moduli of a nematic liquid–crystalline solution of polyelectrolytes. J Chem Phys 87(7):4223
28. Odijk T (1986) Elastic constants of nematic solutions of rod-like and semi-flexible polymers. Liq Cryst 1:553–559
29. Grosberg AY, Zhestkov AV (1986) Polym Sci USSR 28:97
30. Tortora L et al (2010) Self-assembly, condensation, and order in aqueous lyotropic chromonic liquid crystals crowded with additives. Soft Matter 6(17):4157–4167
31. Chami F, Wilson MR (2010) Molecular order in a chromonic liquid crystal: a molecular simulation study of the anionic azo dye sunset yellow. J Am Chem Soc 132(22):7794–7802
32. Kuriabova T, Betterton MD, Glaser MA (2010) Linear aggregation and liquid-crystalline order: comparison of Monte Carlo simulation and analytic theory. J Mater Chem 20:10366
33. Cachitas H, Sebastião PJ, Feio G, Chávez FV (2014) Proton NMR relaxation study of molecular dynamics of chromonic liquid crystal Edicol sunset yellow. Liq Cryst. Accepted
34. Landau LD, Lifshitz EM (1980) Statistical physics. Pergamon Press
35. Landau LD, Lifshitz EM (1986) Theory of elasticity, 3rd edn. Butterworth-Heinemann, Oxford
36. Nakata M et al (2007) End-to-end stacking and liquid crystal condensation of 6-to 20-base pair DNA duplexes. Science 318(5854):1276–1279
37. Dickinson AJ, LaRacuente ND, McKitterick CB, Collings PJ (2009) Aggregate structure and free energy changes in chromonic liquid crystals. Mol Cryst Liq Cryst 509:751–762
38. Hogan M, LeGrange J, Austin B (1983) Dependence of DNA helix flexibility on base composition. Nature 304:752–754
39. Smith SB, Cui Y, Bustamante C (1996) Overstretching B-DNA: the elastic response of individual double-stranded and single-stranded DNA molecules. Science 271:795–799
40. Nastishin YA et al (2004) Pretransitional fluctuations in the isotropic phase of a lyotropic chromonic liquid crystal. Phys Rev E 70(5):051706
41. Lydon J (2011) Chromonic liquid crystalline phases. Liq Cryst 38(11–12):1663–1681
42. der Schoot Pv, Cates ME (1994) Growth, static light-scattering, and spontaneous ordering of Rodlike Micelles. Langmuir 10(3):670–679
43. der Schoot Pv, Cates ME (1994) The isotropic-to-nematic transition in semi-flexible micellar solutions. Europhys Lett 25:515
44. Park HS et al (2008) Self-assembly of lyotropic chromonic liquid crystal sunset yellow and effects of ionic additives. J Phys Chem B 112(51):16307–16319
45. Horowitz VR, Janowitz LA, Modic AL, Heiney PA, Collings PJ (2005) Aggregation behavior and chromonic liquid crystal properties of an anionic monoazo dye. Phys Rev E 72:041710
46. Renshaw MP, Day IJ (2010) NMR characterization of the aggregation state of the azo dye sunset yellow in the isotropic phase. J Phys Chem B 114(31):10032–10038
47. de Gennes PG (1982) Polymer liquid crystals. Academic Press, New York

48. Berberan-Santos MN, Bodunov EN, Valeur B (2005) Mathematical functions for the analysis of luminescence decays with underlying distributions 1. Kohlrausch decay function (stretched exponential). Chem Phys 315:171182
49. Xiao W et al (2014) Structural correspondence of solution, liquid crystal, and crystalline phases of the chromonic mesogen sunset yellow. Cryst Growth Des. doi:10.1021/cg500752x
50. Tortora L, Lavrentovich OD (2011) Chiral symmetry breaking by spatial confinement in tactoidal droplets of lyotropic chromonic liquid crystals. Proc Natl Acad Sci U S A 108(13):5163–5168
51. Peng C, Lavrentovich OD (2015) Chirality amplification and detection by tactoids of lyotropic chromonic liquid crystals. Soft Matter 11(37):7257–7263
52. Jeong J, Davidson ZS, Collings PJ, Lubensky TC, Yodh AG (2014) Chiral symmetry breaking and surface faceting in chromonic liquid crystal droplets with giant elastic anisotropy. Proc Natl Acad Sci U S A 111(5):1742–1747
53. Jeong J et al (2015) Chiral structures from achiral liquid crystals in cylindrical capillaries. Proc Natl Acad Sci 112(15):E1837–E1844
54. Davidson ZS et al (2015) Chiral structures and defects of lyotropic chromonic liquid crystals induced by saddle-splay elasticity. Phys Rev E 91(5):050501
55. Nayani K et al (2015) Spontaneous emergence of chirality in achiral lyotropic chromonic liquid crystals confined to cylinders. Nat Commun 6:8067
56. Zhou S, Shiyanovskii SV, Park H-S, Lavrentovich OD (2017) Fine structure of the topological defect cores studied for disclinations in lyotropic chromonic liquid crystals. Nat Comm. Accepted
57. Kim Y-K, Shiyanovskii SV, Lavrentovich OD (2013) Morphogenesis of defects and tactoids during isotropic–nematic phase transition in self-assembled lyotropic chromonic liquid crystals. J Phys Condens Matter 25(40):404202
58. Lonberg F, Fraden S, Hurd AJ, Meyer RE (1984) Field-induced transient periodic structures in nematic liquid crystals: the twist-Freedericksz transition. Phys Rev Lett 52(21):1903–1906
59. Hui YW, Kuzma MR, San Miguel M, Labes MM (1985) Periodic structures induced by director reorientation in the lyotropic nematic phase of disodium cromoglycate–water. J Chem Phys 83(1):288–292
60. Schneider T, Lavrentovich OD (2000) Self-assembled monolayers and multilayered stacks of lyotropic chromonic liquid crystalline dyes with in-plane orientational order. Langmuir 16(12):5227–5230
61. Shiyanovskii SV et al (2005) Lyotropic chromonic liquid crystals for biological sensing applications. Mol Cryst Liq Cryst 434:587–598
62. Ould-Moussa N et al (2013) Dispersion and orientation of single-walled carbon nanotubes in a chromonic liquid crystal. Liq Cryst 40(12):1628–1635
63. Sokolov A, Zhou S, Lavrentovich OD, Aranson IS (2015) Individual behavior and pairwise interactions between microswimmers in anisotropic liquid. Phys Rev E 91(1):013009
64. Mushenheim PC, Trivedi RR, Tuson HH, Weibel DB, Abbott NL (2014) Dynamic self-assembly of motile bacteria in liquid crystals. Soft Matter 10(1):88–95
65. Mushenheim Peter C, Trivedi Rishi R, Weibel Douglas B, Abbott Nicholas L (2014) Using liquid crystals to reveal how mechanical anisotropy changes interfacial behaviors of motile bacteria. Biophys J 107(1):255–265
66. Mushenheim PC et al (2015) Effects of confinement, surface-induced orientations and strain on dynamical behaviors of bacteria in thin liquid crystalline films. Soft Matter 11(34): 6821–6831

Chapter 5
Living Liquid Crystals

5.1 Introduction

Biological systems composed of large amount of active individuals often show fascinating collective phenomena, such as swirling of fish schools, flocking of birds, migrating of mammal in herds and swarming of bacteria, Fig. 1.4. Despite the wide range of size covered ($10^0 \sim 10^{-6}$ m), individual "particles" of these systems share some common features: (1) they self-propel using internally stored or locally harvested energy, and (2) they interact with each other following simple laws such as steric or hydrodynamic interaction. Describing theses *active matter* systems, physicists apply theories of non-equilibrium statistical mechanics and hydrodynamics [1–4]. For example, in the celebrative Viscek model inspired by bird flocking, each bird is treated as a velocity vector in an two-dimension lattice that takes the average value of the neighboring vectors at the next moment. Viscek showed that an ordered polar pattern (flocking) could emerge as one increases the velocities or the concentration of active particles [1, 4].

The experimental realization of active matter is most conveniently achieved by suspensions of active colloids, for example, swimming bacteria, such as *E-coli* [5] or *Bacillus subtilis* [6]. The interaction of these active particles among themselves and with the medium produces a rich variety of dynamic effects and patterns. Most of the studies so far deal with active particles embedded into a Newtonian isotropic fluid. In this case the interactions among particles are caused by long-range hydrodynamic and short-range excluded volume effects [6–15].

In our work, we conceive a new general class of active fluids, termed living liquid crystals (LLCs). The suspending medium is a non-toxic liquid crystal that supports the activity of self-propelled particles, namely, bacteria. At the very same time, the medium imposes long-range anisotropic interactions onto bacteria, thanks to the intrinsic orientational order that persists even when the bacteria are not active. The importance of the new system is two-fold. Firstly, the bacterial activity modifies the orientational order of the system, by producing well-defined and

© Springer International Publishing AG 2017

S. Zhou, *Lyotropic Chromonic Liquid Crystals*, Springer Theses,
DOI 10.1007/978-3-319-52806-9_5

reproducible patterns with or without topological defects. Secondly, the orientational order of the suspending medium reveals new facets of bacterial behavior, allowing one to control trajectories of individual bacteria and to visualize rotation of flagella through birefringence of the host. The LLCs represent a new example of a biomechanical system, capable of controlled transduction of stored energy into a systematic movement, which is of critical importance in a variety of application, from bio-inspired micromachines to self-assembled microrobots [16, 17]. The study of bacterial motion in LCs and non-Newtonian fluids takes us a step closer to realizing in vitro environments that more closely resemble conditions in vivo [18, 19].

5.2 Materials and Methods

5.2.1 Bacteria

Experiments were conducted with the strain 1085 of *Bacillus subtilis*. The bacteria were initially grown on LB agar plates, then transferred to a Terrific Broth liquid medium (Sigma T5574) and grown in shaking incubator at temperature 35 °C for 10–12 h. To increase resistance to oxygen starvation the bacteria are grown in sealed vials under micro-aerobic conditions [6]. We monitored the concentration of bacteria by the measurement of the optical scattering of the growth media. The bacteria at the end of their exponential growth stage were extracted and washed. The growth medium was separated from the bacteria and removed as completely as possible by centrifugation.

Bacillus subtilis represents a "pusher" type of a swimmer, Fig. 1.3. It has a rod-shaped head of 5–7 μm in length and 0.7 μm in diameters, with about 20 helicoidal 10-μm long flagella filaments attached over the entire head's area. In isotropic media, an active bacterium swims in the so called "run-and-tumble" fashion [20, 21]. In the about 1 s "run" phase, the filaments bundle on one end of the bacterium head and rotate counter clockwise (ccw), when viewed from behind, thus powering unidirectional "head-forward" motion. During the following "tumble" phase that lasts about 0.1 s, one or a few of the flagella reverse their rotation to clockwise (cw) and leave the bundle, causing bacterium to change its orientation randomly. Then the bacterium "runs" again. The motility of aerobic bacteria (such as *Bacillus subtilis*) is controlled by the amount of dissolved oxygen [6, 15, 16]. Substantial amount of research has been in place regarding the individual "pusher" bacteria behavior in isotropic media [20, 22], their interaction with surfaces and with each other [23], as well as collective motion at high volume fraction [6, 11, 16, 21].

5.2.2 LLC Preparation

Chromonic lyotropic LC material disodium cromoglycate (DSCG) purchased from Spectrum Chemicals, 98% purity, was dissolved in Terrific Broth at 16 wt%. This

solution was added to the concentrated bacteria obtained as described above. The resulting LLC was mixed by stirring with a clean toothpick and then in a vortex mixer at 3000 rpm. The LLC mixture was injected (by pressure gradient) into a flat cell made from two square glass plates (10 × 10 mm) separated by spacers. Two interior surfaces were pretreated with polyimide SE7511 and rubbed with velvet cloth along the x-axis, to provide a uniform planar alignment of the LLC [24], $\hat{\mathbf{n}}_0 = (1, 0, 0)$. The cell was sealed with high vacuum grease (Dow Corning) to prevent water evaporation. The temperature shift of the LC phase diagrams during several hours of the experiments is less than 1 °C and thus does not affect the data presented. The observations were started immediately after the sealed cells were placed in a heating stage (Linkam PE94) at 25 °C.

The range of a stable nematic phase of the LLC depends on both the concentration of the mesogenic material and temperature; at low concentrations and/or high temperatures, the material melts into an isotropic fluid. The bacterial-free chromonic LC and the LLC show approximately the same phase diagram in the concentration-temperature coordinates. For the used lyotropic LC, the average value of the splay and bend elastic constants is K = 10–12 pN [25]; the average viscosity $\eta \sim 10\ \mathrm{kgm^{-1}s^{-1}}$ as determined in the dynamic light scattering experiment that measures the director relaxation in uniformly aligned planar cells [4, 25–27].

5.2.3 Videomicroscopy

An inverted microscope Olympus IX71 with a motorized stage, mounted on a piezoelectric insolation platform Herzan TS-150 and Prosilica GX 1660 camera (resolution of 1600 × 1200) were used to record motion of individual bacteria in thin cells. Images were acquired with the frame rate up to 100 frames/s, at 60× magnification, oil-immersion objective, in cross-polarized light. Color camera with the resolution 1280 × 1024 and the frame rate 10 frames/s and 2×–20× magnifications were used to acquire large-scale patterns of collective motion. The acquired images were processed in Matlab.

5.2.4 PolScope Microscopy

The LLC textures were examined by a polarizing microscope (Nikon E600) equipped with Cambridge Research Incorporation (CRI) Abrio LC-PolScope package. The LC PolScope uses a monochromatic illumination at 546 nm and maps optical retardance $\Gamma(x, y)$ in the range (0–273) nm and orientation of the slow axis [28]. For tangentially anchored LLC, $\Gamma = |n_e - n_o|h$, where n_e and n_o are the extraordinary and ordinary refractive indices, h is the cell thickness. For DSCG,

optical birefringence is negative, $n_e - n_o \approx -0.02$ [29]. The slow axis is thus perpendicular to the optic axis and to $\hat{\mathbf{n}}$. The PolScope was set up to map the local orientation $\hat{\mathbf{n}}(x, y)$, Fig. 5.5b.

5.3 Results and Discussions

The concept of LLC is enabled by the recent progress in water-soluble non-toxic chromonic LCs [18, 19, 29] and growing expertise in control and manipulation of bacterial suspensions in confined geometries [6, 13–16]. Our studies have shown that *living bacteria can be transferred to the LC media, and yield highly nontrivial interactions with the molecular ordering of the LC*. We quantify this interaction by examining the simplest nematic phase of the LLC at different levels of bacteria activity. In the absence of activity, the LLC is a standard nematic characterized by the long-range orientational order described by a unit director $\hat{\mathbf{n}}$ with the property $\hat{\mathbf{n}} = -\hat{\mathbf{n}}$. Its ground state is a uniform director field, $\hat{\mathbf{n}} = \text{const}$. When the activity is turned on, but kept very low, i.e. individual bacteria are separated by long distances, the nematic order dominates the motion of the swimmers: their trajectories are along the director field predetermined by the LC medium. As the activity is further increased by an elevated bacteria volume fraction, the LLC exhibits the onset of large-scale undulations of a nematic director with a characteristic length ξ (see below) determined by the balance between bacteria activity and anisotropic viscoelasticity of the lyotropic chromonic.

5.3.1 Single Bacteria Motion

When placed in the uniformly aligned LC, the bacteria show a number of intriguing dynamic phenomena that can be attributed to the coupling of the LC structure to an individual bacterium and to the collective effects. Since the individual behavior is pertinent for the understanding of emerging collective motion, we first discuss the dynamics of individual bacteria in relatively thin (of thickness $h = 5$ μm) LLC flat glass cells, Fig. 5.1.

At low density, when bacteria are separated at large distances, we find that individual bacteria swim along director $\hat{\mathbf{n}}_0$, in agreement with earlier observations [19, 30]. The most striking feature observed in our experiments is that the bacterial flagella, having a diameter of only about 24 nm, produces director perturbations on a scales of micrometers, Fig. 5.1a–c. Birefringence of the LLC makes these perturbations clearly seen under the polarizing microscope, Fig. 5.1a. The texture in Fig. 5.1a observed with de-crossed polarizers, reveals periodic dark and bright elongated spots tilted with respect to $\hat{\mathbf{n}}_0$ and caused by the broken chiral symmetry of the director distortions (see Sect. 5.5). The map of optical retardance in

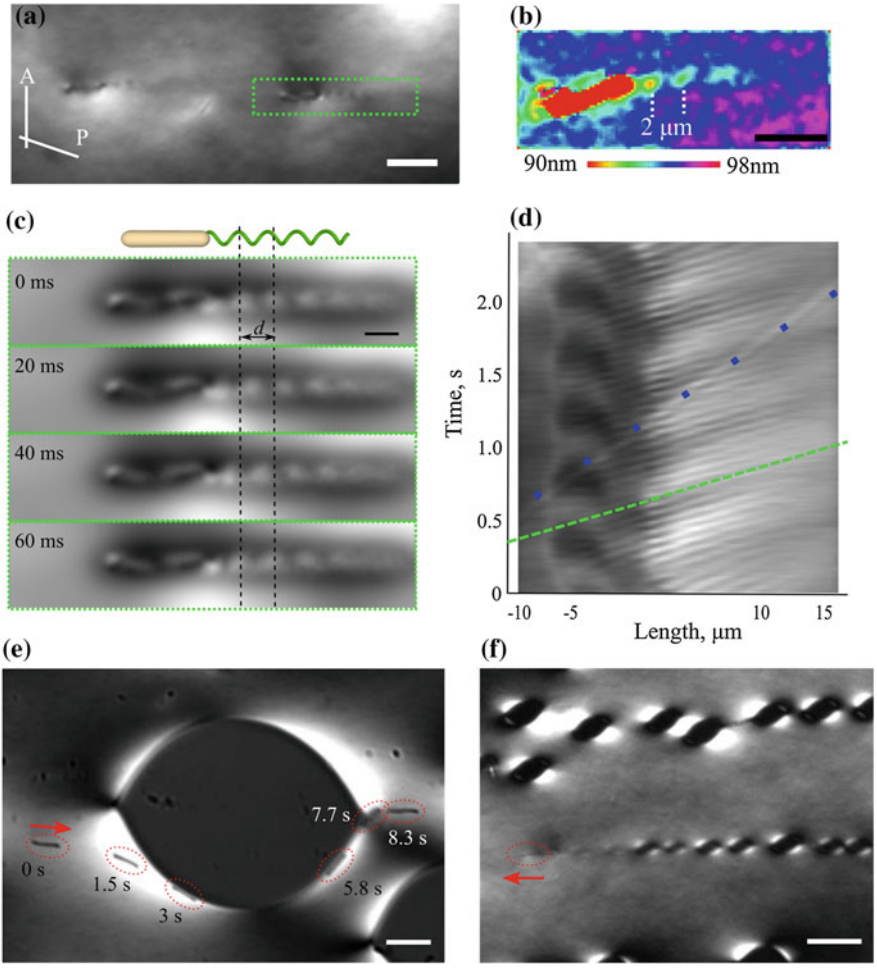

Fig. 5.1 Distortion of the nematic director detected by optical microscopy. **a** Snapshot of swimming bacteria observed under a microscope with slightly de-crossed polarizer (P) and analyzer (A). The bacterium shown in *green box* swims from the *right* to *left*. **b** Optical retardance pattern around a swimming bacterium, see also Figs. 5.4, 5.5 and 5.6. **c** Time evolution of the director waves created by rotating flagella in the co-moving reference frame. **d** Space-time diagram for director waves extracted for the bacterium shown in panel **c**. A total of 240 cross-sections were extracted from 2.4 s video. *Dashed green line* depicts phase velocity of the flagella wave. *Dots* mark an immobilized dust particle. **e** The trajectory of a single bacterium around a tactoid. **f** Trace of isotropic tactoids left by a bacterium at temperature about 0.5 °C below the nematic-biphasic transition point. Observations are made under a microscope with slightly de-crossed polarizer (P) and analyzer (A). Scale bar 5 μm (**a**, **b**), 2 μm (**c**), 10 μm (**e**), 20 μm (**f**)

Fig. 5.1b, obtained with a PolScope (see Sect. 5.2) [28], demonstrates that the effective birefringence near the bacterium is reduced as compared to the uniform director surrounding.

The pattern of alternating bright and dark spots in the bacterium wake propagates with a wavelength about $d = 2$ μm. At a fixed distance from the body of bacterium, the bright and dark regions alternate with the frequency of about 16 Hz, Fig. 5.1c. The wavelength is determined by the pitch of helical flagella, and the frequency by the flagella rotation rate. We constructed a space-time diagram by stacking a total of 240 consecutive cross-sections along the bacterium's axis in a co-moving reference frame from each image, Fig. 5.1d. From the space-time diagram we clearly see propagation of the flagella wave (parallel white lines between 0 and 15 μm) and counter-rotation of the bacterial body (dark regions at −5 μm) with a rate of 2.5 Hz. The ratio of flagella rotation to the counter-rotation of the body is about 7:1, similar to that known for *Bacillus subtilis* under normal conditions (160 Hz flagella rotation and 20 Hz body counter-rotation [31]) in isotropic media.

Individual behavior of bacteria and its coupling to the orientational order becomes especially interesting as the temperature is increased and the LLC approaches a biphasic region, in which the isotropic and nematic phases coexist. The isotropic regions appear as characteristic "negative tactoids" elongated along the overall director of the surrounding nematic [26, 32]. The isotropic tactoids, seen as dark islands in Fig. 5.1e, distort the director around them and change the trajectories of the bacteria. As shown in Fig. 5.1e, far away from the tactoid, a bacterium is swimming along a straight line set by the uniform director. In the vicinity of tactoid, the trajectory deviates from the straight line and follows the local distorted director. After a collision with the isotropic-nematic interface, the bacterium follows the curved interface, and finally escapes at the cusp of the tactoid. The fact that bacteria can follow the nematic-isotropic interface and the overall director in the LLC offers numerous design concepts of reconfigurable microfluidic devices for the control and manipulation of bacteria. The desired trajectories of bacterial transport can be engineered by patterned surface anchoring and by local dynamic heating (for example, with focused laser beams).

Following the idea that bacteria swim only along the director $\hat{\mathbf{n}}$, we demonstrate that bacteria can transfer cargo particles placed in front of them, along the director line that the bacterial trajectory follows [33]. The cargo particle starts to respond to the hydrodynamic force exerted by the bacterium when the distance between the two is rather large, $50 \sim 80$ μm, or 10–16 bacterial body lengths. The force is narrowly concentrated within the bacterial trajectory; particles placed just $1 - 2$ μm off the trajectory are not affected. Combining this effect with the idea of reconfiguring director field by localized laser heating, one can imagine "domestication" of bacteria to assemble cargo particles into various shapes without a predesigned microfluidic device.

The reason why bacteria swim along the director lies in both their elongated body shape and planar anchoring of the director at their surface. As demonstrated later in Sect. 5.3.2, when the oxygen is turned off, inactive bacteria align along the director to minimize the elastic energy of distortions, Fig. 5.2a. When geometrically confined in shallow homeotropic cells, bacteria can swim perpendicularly to the overall director field by locally distorting it [34]. By estimating the elastic torque, we conclude that the bacterial body provides only weak and degenerate planar

anchoring, on the order of 10^{-6} Jm^{-2}. This elastic alignment might be further assisted by hydrodynamic effect. The anomalously large anisotropy of the viscosity coefficients in DSCG confines the flow field narrowly along $\hat{\mathbf{n}}$, as evidenced by the cargo transportation experiments mentioned above. The details of hydrodynamic effects need further clarification.

When the LLC temperature is close to the biphasic region, even more strikingly, the bacteria themselves can create isotropic tactoids in their wake, Fig. 5.1f. The LLC acts as miniature "Wilson chamber" in which the isotropic droplets decorate the path of swimming bacteria. The feature underscores the complexity of interplay between velocity fields and the state of orientational order that can involve a number of different mechanisms, such as existence of a nucleation barrier, non-uniform distribution of components between the nematic and isotropic phase, etc. Nucleation of the isotropic phase in Fig. 5.1f implies that the bacterial flows reduce the local degree of orientational order, most probably through disintegration of the chromonic aggregates [29]. A strong reduction of the degree of ordering in LCLC by director deformations is also evidenced in the observations of disclination cores [35], around which the director field $\hat{\mathbf{n}}$ makes a $\pm\pi$ turn. The scalar order parameter is greatly reduced from its equilibrium value of undistorted nematic phase already at distances as large as ~ 10 μm from the center. Therefore, the observed reduction of optical retardance in the bacteria wake, Fig. 5.1b, may result from both the director realignment and from the reduction of the degree of orientational order.

5.3.2 *Collective Behavior*

Now we discuss collective behavior of LLC emerging at higher concentrations of bacteria. We discovered that a long-range nematic alignment of the LLC is affected by the flow created by the swimming bacteria. The coupling of the orientational order and hydrodynamic flow yields nontrivial dynamic patterns of the director and bacterial orientations, see Figs. 5.2 and 5.3.

The first example, Fig. 5.2, demonstrates the existence of a characteristic spatial length scale ξ in LLCs that sets this non-equilibrium system apart from standard equilibrium LCs. The LLC is confined between two glass plates that fix $\hat{\mathbf{n}}_0 = (1, 0, 0)$ along the rubbing direction. In the samples with inactive bacteria the steady state is uniform, $\hat{\mathbf{n}} = \hat{\mathbf{n}}_0 = \text{const}$, and the immobilized bacteria are aligned along the same direction, Fig. 5.2a, b. In chambers with active bacteria, supported by the influx of oxygen through the air-LLC interface (on the left hand side in Fig. 5.2e), the uniform state becomes unstable and develops a stripe pattern with periodic bend-like deviations of $\hat{\mathbf{n}}$ from $\hat{\mathbf{n}}_0$, Fig. 5.2c–e. The swimming bacteria are aligned along the local director $\hat{\mathbf{n}}$, Fig. 5.2d. Since the oxygen permeates the LLC from the open side of the channel, its concentration is the highest at the air-LC interface; accordingly, the stripes appear first near the air-LLC interface. The period ξ of

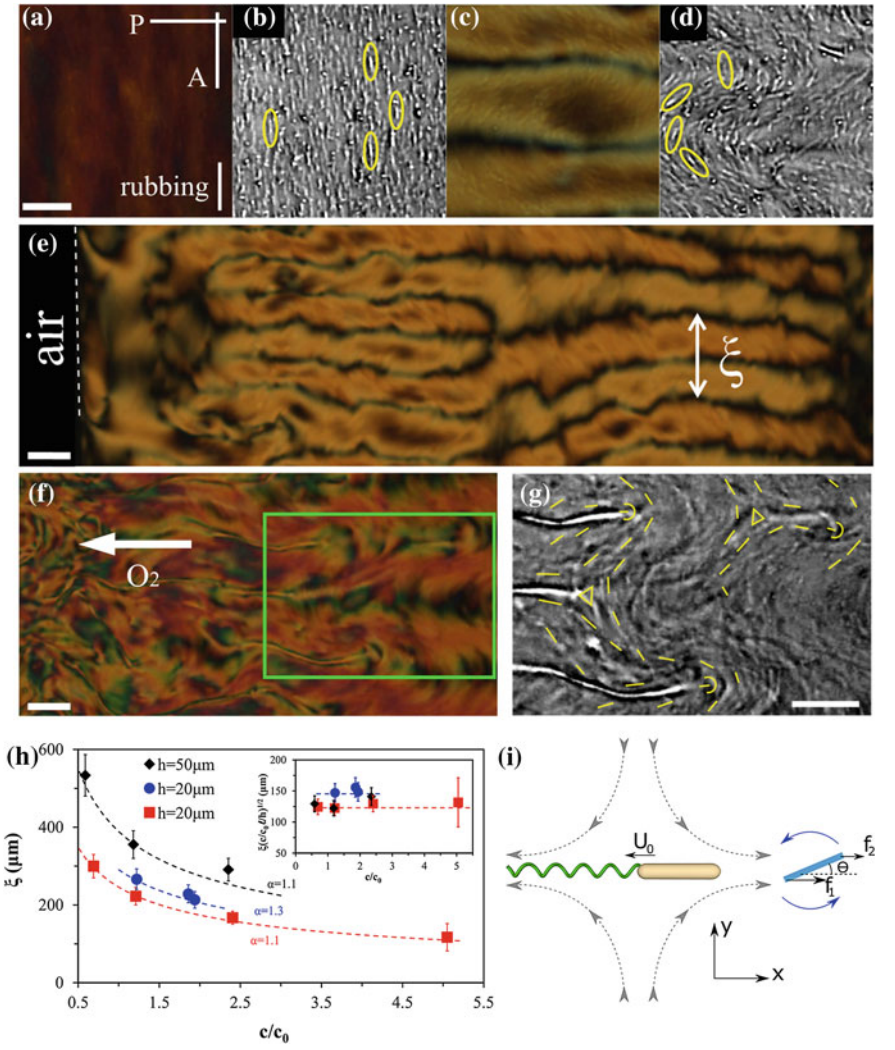

Fig. 5.2 Emergence of a characteristic length scale in LLCs. **a**, **b** LLC with inactive bacteria is at its equilibrium state with the director and bacteria (*highlighted by ellipses*) aligned uniformly along the rubbing direction; **c**, **d** active bacteria produce periodically distorted director. **e** Proliferation of *stripe pattern* in the sample of thickness $h = 20$ μm and for low concentration of bacteria, $c \approx 0.9 \times 10^9$ cells/cm^3. Oxygen permeates from the left hand side. **f** LLC patterns in thicker sample ($h = 50$ μm) and for higher concentration of bacteria, $c \approx 1.6 \times 10^9$ cells/cm^3. *White arrow* points toward a higher concentration of oxygen. **g** Zoomed area in panel **f** shows nucleating disclinations of strength +1/2 (*semi-circles*) and −1/2 (*triangles*). *Bright dashes* visualize bacterial orientation. **h** Dependence of characteristic period ξ on c and h; *dashed lines* depict fit to theoretical prediction $\xi = \sqrt{\frac{Kh}{c\alpha_0 l U_0}}$. *Inset* illustrates collapse of the data into a universal behavior that follows from the theoretical model. **i** Director realignment (shown as a *rod*) caused by the bacterium-generated flow (shown by *dashed lines with arrows*). Scale bar 50 μm (**a**–**d**), 100 μm (**e**–**g**). Error bars are ±10% SEM (standard error of the mean), except for ±30% SEM at $c/c_0 = 5.05$

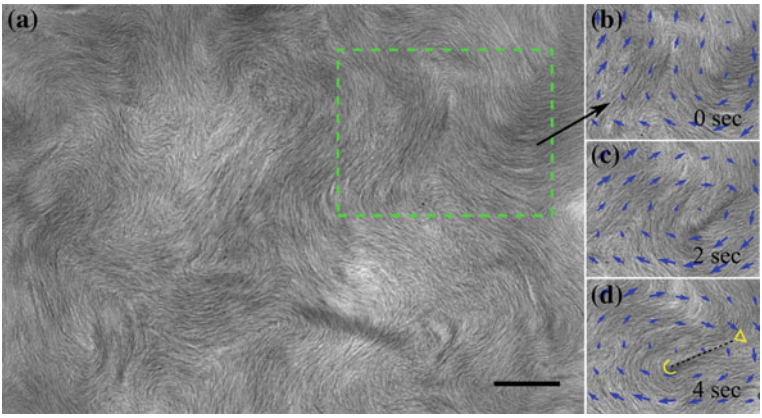

Fig. 5.3 LLC in sessile drop. **a** Texture with multiple disclination pairs, *green rectangle* indicates the region shown in (**b**, **c**, **d**). Bacteria are aligned along the local nematic director, as revealed by the fine stripes. Scale bar 30 μm. No polarizers. (**b**, **c**, **d**) LLC texture with −1/2 and 1/2 disclinations and the pattern of local flow velocity (*blue arrows*) determined by particle-image velocimetry. The flow typically encircles the close pair of defects

stripes increases with the increase of the distance from the air-LLC interface as the amount of oxygen and the bacterial activity decrease. Figure 5.2h shows that ξ increases when the concentration c of bacteria and the chamber height h decrease. The data in Fig. 5.2h are collected for different samples in which the velocity of bacteria was similar (8 ± 3 μm/s), as established by a particle-tracking velocimetry; the concentration is normalized by the concentration $c_0 \approx 8 \times 10^8$ cells/cm^3 of the stationary growth phase.

As time evolves, in the regions with the highest bacterial activity, near the open edge, the stripe pattern becomes unstable against nucleation of pairs of ± ½ disclinations, Fig. 5.2f, g. Remarkably, the pattern-forming instabilities occurring here have no direct analog for bacterial suspensions in Newtonian fluids or for bacteria-free pure LCs. The concentration of bacteria in our experiments (close to 0.2% of volume fraction) is about 1/10 of that needed for the onset of collective swimming in Newtonian liquids (about 10^{10} cells/cm^3 [6]).

Figure 5.3 illustrates the profound effect of bacterial activity on spatio-temporal patterns in a sessile drop of LCCs [6, 36] in which there is no preferred director orientation in the plane of film. Bacterial activity generates persistently rearranging bacterial and director patterns with ± ½ disclinations that nucleate and annihilate in pairs, similarly to the recent experiments on active microtubule bundles [7], Fig. 5.3a. The characteristic spatial scale of the pattern, determined as an average distance between the disclination cores, is in the range of 150–200 μm, of the same order of magnitude as ξ in the stripe pattern in strongly anchored sample. The fluid flow typically encircles disclination pairs, Fig. 5.3b–d.

Emergence of a characteristic length scale ξ in LCCs, either as a period of the stipe pattern in Fig. 5.2 or as a characteristic separation of disclinations in Fig. 5.3,

is caused by the balance of director-mediated elasticity and bacteria-generated flows, Fig. 5.2i. Since no net force is applied to a self-propelled object, a swimming bacterium represents a moving negative hydrodynamic force dipole of the strength $\mathfrak{U}_0$ ("pusher"), as it produces two outward fluid streams coaxial with the bacterial body [37]. The strength of the dipole (of a dimension of torque or energy) is of the order 1 pN μm [23]. In the approximation of nearly parallel orientation of the bacterium and the local director $\hat{\mathbf{n}}$, the bacteria-induced streams, Fig. 5.2i, impose a reorienting torque $\sim \alpha(h) c U_0 \theta$, where $\alpha(h)$ is a dimensionless factor that describes the flow strength and depends on the cell thickness h; c is the concentration of bacteria, and Θ is the angle between local orientation of bacteria and $\hat{\mathbf{n}}$. Similar torques caused by shear flow are well known in the physics of liquid crystals [26], see Sect. 5.5 and Fig. 5.6. Mass conservation yields an estimate $\alpha = \alpha_0 l/h$, where constant $\alpha_0 \approx \boldsymbol{O}(1)$, and l is the length of a bacterium. It implies that the channel's thickness reduction increases the flow because the bacteria pump the same amount of liquid. The local bacterium-induced reorienting hydrodynamic torque is opposed by the restoring elastic torque $\sim K \frac{\partial^2 \theta}{\partial x^2}$; K is an average Frank elastic constant of the LC. In the case of a very thin layer confined between two plates with strong surface anchoring, the strongest elastic torque $K_2 \frac{\partial^2 \theta}{\partial z^2}$ will be associated with the twist deformation along the vertical z-axis. However, since the elastic constant for twist is an order of magnitude smaller than the splay and bend constants [25], the restoring torque in relatively thick (20 and 50 μm) samples is caused mainly by in-plane distortions. By balancing the elastic and bacterial torques, $\partial^2 \theta / \partial x^2 = \theta / \xi$, one defines a "bacterial coherence length" $\xi = \sqrt{\frac{Kh}{\alpha_0 l c U_0}}$ (somewhat similar arguments for the characteristic length of bending instability in active nematics were suggested in [2]). This expression fits the experimental data on the periodicity of stripe patterns for different concentrations of bacteria c and thicknesses h remarkably well with a choice of $\alpha_0 \approx 1$, see Fig. 5.2h.

The experiments in Figs. 5.2 and 5.3 clarifies the rich sequence of instabilities by which the activity of bacteria transforms the initial non-flowing homogeneous uniform steady state in Fig. 5.2a, b into the state of self-sustained active fluid turbulence, Fig. 5.3. The first step is through appearance of the periodic director bend with a characteristic length scale ξ, Fig. 5.2c–e. The period becomes shorter as the activity increases, Fig. 5.2h. Further escalation of the activity causes a qualitative transformation, namely, nucleation of defect pairs, Fig. 5.2f, g. Note that the axis connecting the cores of 1/2 and −1/2 disclinations in the pair and the local director $\hat{\mathbf{n}}$ along this axis are perpendicular the original director $\hat{\mathbf{n}}_0$, Fig. 5.2g. Once the system can overcomes the stabilizing action of surface anchoring, as in Fig. 5.3, the dynamic array of moving defects forms a globally isotropic state in which the local director $\hat{\mathbf{n}}$ is defined only locally (somewhat similar dynamic behavior was observed in simulations of "active nematic" in Refs. [38, 39]). The final state, Fig. 5.3, is an example of "active fluid" turbulence at vanishing Reynolds number [6, 36], which is in our case on the order of 10^{-5}.

5.4 Conclusions

LLC demonstrates a wealth of new phenomena not observed for either suspension of bacteria in a Newtonian fluid or in passive ordered fluid. The concept of a characteristic length ξ, contrasting the elastic response of orientationally ordered medium and the activity of microswimmers, may also be useful for understanding hierarchy of spatial scales in other active matter systems [6, 9–13]. One advantage of our system is the independent control of activity (through bacteria concentration c and oxygen availability) and of the nematic order (through the DSCG concentration and temperature), which enabled us to tune ξ with different combinations of parameters such as c and h, as well as drive the system through different stages of transition from the equilibrium uniform state with immobilized bacteria to the dynamic state of periodic bend, and at the higher levels of activity or concentration, topological turbulence with defects nucleating in pairs from the bend structure. Our studies were focused on the simplest nematic LLC. However, more complex LLCs can be explored as well, for example, smectics and cholesteric LCs with controlled chirality. Exploration of LLCs may have intriguing applications in various fields. Our biomechanical system may provide the basis for devices with new functionalities, including specific responses to chemical agents, toxins, or photons. Swimming bacteria can also serve as autonomous "microprobes" for the properties of LCs. Unlike passive microprobes [40], swimming bacteria introduce local perturbations of the LC molecular order in terms of both the director and the degree of order, and thus provide unique information on the mesostructure of the material. In turn, LC medium provides valuable optically accessible information on the intricate submicrometer structure of bacteria-generated microflow that deserves further investigation.

5.5 Supplemental Information

5.5.1 *Optics of Director Patterns in the Wake of a Moving Bacterium*

We numerically simulated the optical patterns observed under the polarizing microscope, using standard Berreman 4×4 matrix method [41]. We model the director field distorted by the flagella as following:

$$\begin{aligned} n_y(x,y,z) &= \sin\varphi_0 \sin(-kx)(1-\beta|z-z_0|)\exp\left(-\frac{|y-y_0|}{\lambda}\right), \\ n_z(x,y,z) &= -\sin\varphi_0 \cos(-kx)(1-\beta|z-z_0|)\exp\left(-\frac{|y-y_0|}{\lambda}\right), \\ n_x(x,y,z) &= \sqrt{1-n_y^2-n_z^2} \end{aligned} \tag{5.1}$$

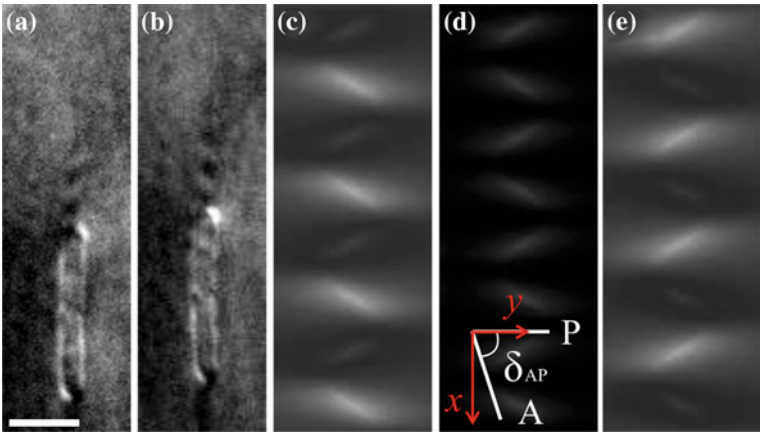

Fig. 5.4 Light intensity pattern for a linearly polarized light passing through the twisted director configuration as described in the Sect. 5.5.1. **a**, **b** polarizing microscopy textures of oblique *black and white regions* in the wake area of swimming bacteria. **c**, **d**, **e** Optical simulation of director textures deformed by the helicoidal flagella viewed between two linear polarizers making a different angle δ_{AP} = 80° (**c**), 90° (**d**) and 100° (**e**). Scale bar 5 μm

where $(x, y_0, z_0) = (x, r_0\cos(-kx), r_0\sin(-kx))$ defines the position of left handed helical flagella along x-axis and centered at (0, 0) of y–z plane. By its rotation, director $\hat{\mathbf{n}}$ deviates from $\hat{\mathbf{n}}_0 = (1, 0, 0)$ by the angle $\phi_0 = 10°$ at the flagella and linearly decay in z direction with the rates $\beta = \left(z_0 + \frac{h}{2}\right)^{-1}$ (for $z < z_0$) and $\left(\frac{h}{2} - z_0\right)^{-1}$ (for $z \geq z_0$), and exponentially decay in the y direction with a characteristic decay length λ = 1 μm; $r_0 = 0.5$ μm is the rotation radius of flagella; $k = 2\pi P^{-1}$, $\mathfrak{P}$ = 2 μm is the helical pitch of the flagella. By using this model, we display in Fig. 5.4 the textures for different analyzer orientations in the area corresponding to four periods of the director pattern along the x direction and to 3λ along the y direction.

5.5.2 *Optics of Director Patterns Distorted by Flows Produced by Individual Bacterium*

Figure 5.1a shows that the regions under and above a moving bacterium have a different optical density. Figure 5.5 shows a clear manifestation of this effect, for a bacterium that is pinned or does not swim (but otherwise active and has rotating flagella), apparently because it is close to the stage of division into two bacteria and has two sets of flagella. For this bacterium, the optical density pattern resembles a butterfly, Fig. 5.5a, in which the director distortions propagate over tens of micrometers. PolScope image of the director field indicates that the director forms a

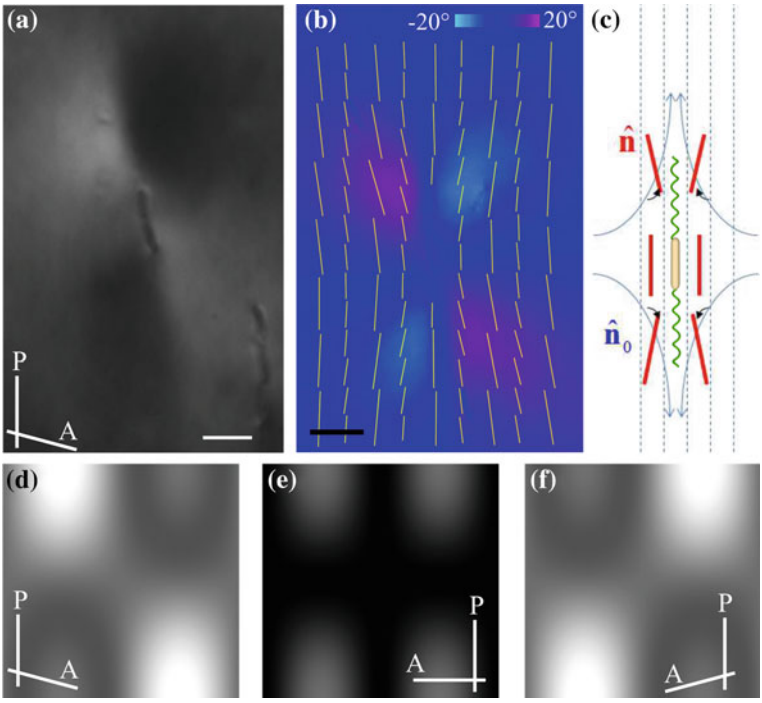

Fig. 5.5 Director distortions around an immobile bacterium. **a** Optical polarizing microscopy texture with de-crossed polarizers shows a "*butterfly*" pattern. **b** PolScope texture maps director pattern (*yellow lines*) resembling an "X" letter; color scale is proportional to the angle that the local director makes with the long axis of the image. **c** A schematic representation showing how the director (*red bar*) deviates from $\hat{\mathbf{n}}_0 = (1, 0, 0)$ (*blue dashed lines*) due to the flow (*blue arcs with arrows*) induced by non-swimming two-tail bacterium. **d**, **e**, **f** Optical simulation of the director pattern in part **b** shows the *butterfly* pattern in the intensity map when the two polarizers are crossed at different angles (**a**, **b**). Scale bar 5 μm (**a**), 10 μm (**b**)

tilted pattern in the shape of the letter "X", Fig. 5.5b. The effect can be explained by the flow-induced reorientation of the director, schematically shown in Fig. 5.5c (see also Fig. 5.3i). Optical simulations based on the Berreman matrices show that these director distortions results in the butterfly pattern when the sample is observed between two polarizers, Fig. 5.5d–f. Analytical calculation with Jones matrix method shows that the field of light passing through a polarizer, a sample with retardance Γ oriented at φ, and a analyzer at φ_{AP} follows

$$\begin{bmatrix} E_a \\ 0 \end{bmatrix} = \frac{1}{\sqrt{2}} \begin{bmatrix} 1 & 0 \\ 0 & 0 \end{bmatrix} \begin{bmatrix} \cos\varphi_{\mathrm{AP}} & \sin\varphi_{\mathrm{AP}} \\ -\sin\varphi_{\mathrm{AP}} & \cos\varphi_{\mathrm{AP}} \end{bmatrix} \begin{bmatrix} \cos\varphi & -\sin\varphi \\ \sin\varphi & \cos\varphi \end{bmatrix} \begin{bmatrix} \mathrm{e}^{-i\Gamma/2} & 0 \\ 0 & \mathrm{e}^{i\Gamma/2} \end{bmatrix} \begin{bmatrix} \cos\varphi & \sin\varphi \\ -\sin\varphi & \cos\varphi \end{bmatrix} \begin{bmatrix} 1 \\ 0 \end{bmatrix} \tag{5.2}$$

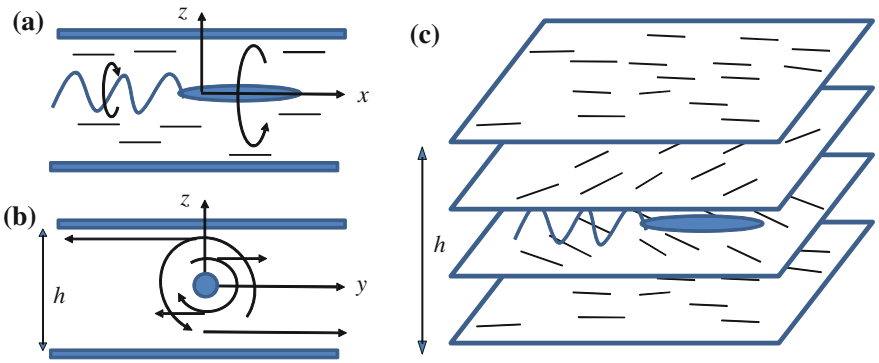

Fig. 5.6 Chiral symmetry breaking of the LLC director pattern caused by a rotating bacterium. **a**, **b** Schematics of the flows generated by the rotating bacterium. **c** Scheme of the director twist along the vertical z-axis

thus intensity at the analyzer

$$I_a = \frac{1}{2}\cos^2(\varphi_{AP} - \varphi)\cos^2\varphi + \sin^2(\varphi_{AP} - \varphi)\sin^2\varphi - \frac{1}{4}\sin 2(\varphi_{AP} - \varphi)\sin 2\varphi \cos\Gamma \quad (5.3)$$

For $\Gamma = -1.15$ (ɧ = 5 μm, $\Delta n = -0.02$, wavelength of the light 546 nm) as in our samples, I_a has minimum values at $\varphi_{AP} \approx 90^\circ + \frac{1}{2}\varphi$ when $\varphi < 25^\circ$. This confirms the experimental and optical simulation texture of "butterfly" shaped director field, Fig. 5.5a, d–f. For a moving bacterium, the effect is qualitatively similar, with the difference that the propulsion enhances the front two "wings" of the butterfly and weakens the rear two wings; as a result, the regions below and above the bacterium's head have different brightness, Fig. 5.1a, c.

Besides the two coaxial streams, the bacterium also creates velocity fields associated with rotations of its body and its flagella (in opposite directions, Fig. 5.6a, b). These rotations cause director reorientations that lack the mirror symmetry with respect to the plane passing through the long axis of the bacterium, Fig. 5.6c; these deformations would further complicate the director pattern in the close vicinity of a moving bacterium; these effects will be explored in details in the future.

The director distortions would be created by a moving bacterium when the viscous torque overcomes the elastic one, which is equivalent to the requirement that the Ericksen number of the problem is larger than 1. For a rotating bacterium in a cell of thickness ɧ, the Ericksen number [26] is $Er = \eta f r h/K$, where η is an effective viscosity, f is the frequency of bacterium head rotation, ɾ is the bacterium radius. For typical values of parameters in our problem, $K = 10$ pN, $\eta = 10$ kg/(m · s), $f = 2$ Hz, $r = 0.4$ μm, ɧ = 20 μm, this requirement is easily

satisfied, as $Er = 16$. As already discussed in the main text, the shear flows produced by the bacteria can also cause a decrease in the degree of orientational order, which corresponds to Deborah numbers close to 1 or larger.

References

1. Vicsek T, Zafeiris A (2012) Collective motion. Phys Rep 517(3–4):71–140
2. Ramaswamy S (2010) The mechanics and statistics of active matter. Annu Rev Condens Matter Phys 1(1):323–345
3. Marchetti MC et al (2013) Hydrodynamics of soft active matter. Rev Mod Phys 85(3): 1143–1189
4. Vicsek T, Czirók A, Ben-Jacob E, Cohen I, Shochet O (1995) Novel type of phase transition in a system of self-driven particles. Phys Rev Lett 75(6):1226–1229
5. Schwarz-Linek J et al (2016) Escherichia coli as a model active colloid: a practical introduction. Colloids Surf B 137:2–16
6. Sokolov A, Aranson IS (2012) Physical properties of collective motion in suspensions of bacteria. Phys Rev Lett 109(24):248109
7. Sanchez T, Chen DTN, DeCamp SJ, Heymann M, Dogic Z (2012) Spontaneous motion in hierarchically assembled active matter. Nature 491(7424):431–434
8. Sumino Y et al (2012) Large-scale vortex lattice emerging from collectively moving microtubules. Nature 483(7390):448–452
9. Palacci J, Sacanna S, Steinberg AP, Pine DJ, Chaikin PM (2013) Living crystals of light-activated colloidal surfers. Science 339(6122):936–940
10. Schaller V, Weber C, Semmrich C, Frey E, Bausch AR (2010) Polar patterns of driven filaments. Nature 467(7311):73–77
11. Zhang HP, Be'er A, Florin E-L, Swinney HL (2010) Collective motion and density fluctuations in bacterial colonies. Proc Nat Acad Sci 107(31):13626–13630
12. Schwarz-Linek J et al (2012) Phase separation and rotor self-assembly in active particle suspensions. Proc Nat Acad Sci 109(11):4052–4057
13. Wensink HH et al (2012) Meso-scale turbulence in living fluids. Proc Nat Acad Sci 109(36): 14308–14313
14. Gachelin J et al (2013) Non-Newtonian viscosity of Escherichia coli suspensions. Phys Rev Lett 110(26):268103
15. Dunkel J et al (2013) Fluid dynamics of bacterial turbulence. Phys Rev Lett 110(22):228102
16. Sokolov A, Apodaca MM, Grzybowski BA, Aranson IS (2010) Swimming bacteria power microscopic gears. Proc Nat Acad Sci 107(3):969–974
17. Snezhko A, Aranson IS (2011) Magnetic manipulation of self-assembled colloidal asters. Nat Mater 10(9):698–703
18. Woolverton CJ, Gustely E, Li L, Lavrentovich OD (2005) Liquid crystal effects on bacterial viability. Liq Cryst 32(4):417–423
19. Mushenheim PC, Trivedi RR, Tuson HH, Weibel DB, Abbott NL (2014) Dynamic self-assembly of motile bacteria in liquid crystals. Soft Matter 10(1):88–95
20. Darnton NC, Turner L, Rojevsky S, Berg HC (2007) On torque and tumbling in swimming Escherichia coli. J Bacteriol 189(5):1756–1764
21. Elgeti J, Winkler RG, Gompper G (2015) Physics of microswimmers—single particle motion and collective behavior: a review. Rep Prog Phys 78(5):056601
22. Chattopadhyay S, Moldovan R, Yeung C, Wu XL (2006) Swimming efficiency of bacterium Escherichiacoli. Proc Nat Acad Sci 103(37):13712–13717

23. Drescher K, Dunkel J, Cisneros LH, Ganguly S, Goldstein RE (2011) Fluid dynamics and noise in bacterial cell–cell and cell–surface scattering. Proc Nat Acad Sci 108(27): 10940–10945
24. Nastishin YA et al (2005) Optical characterization of the nematic lyotropic chromonic liquid crystals: Light absorption, birefringence, and scalar order parameter. Phys Rev E 72(4): 041711
25. Zhou S et al (2012) Elasticity of lyotropic chromonic liquid crystal probed by director reorientation in a magnetic field. Phys Rev Lett 109:037801
26. Kleman M, Lavrentovich OD (2003) Soft matter physics: an introduction. Springer, New York, p 638
27. Zhou S et al (2014) Elasticity, viscosity, and orientational fluctuations of a lyotropic chromonic nematic liquid crystal disodium cromoglycate. Soft Matter. doi:10.1039/c1034sm00772g
28. Shribak M, Oldenbourg R (2003) Techniques for fast and sensitive measurements of two-dimensional birefringence distributions. Appl Opt 42(16):3009–3017
29. Park HS, Lavrentovich OD (2012) Lyotropic chromonic liquid crystals: emerging applications. In: Li Q (ed) Liquid crystals beyond displays: chemistry, physics, and applications, Wiley, New Jersey p 449–484
30. Kumar A, Galstian T, Pattanayek SK, Rainville S (2013) The motility of bacteria in an anisotropic liquid environment. Mol Cryst Liq Cryst 574(1):33–39
31. Dewenter L, Alpmann C, Woerdemann M, Denz C (2012) Video-based analysis of the rotational behaviour of rod-shaped, self-propelled bacteria in holographic optical tweezers, p 84270N–84270N–84210
32. Kim Y-K, Shiyanovskii SV, Lavrentovich OD (2013) Morphogenesis of defects and tactoids during isotropic–nematic phase transition in self-assembled lyotropic chromonic liquid crystals. J Phys Cond Matter 25(40):404202
33. Sokolov A, Zhou S, Lavrentovich OD, Aranson IS (2015) Individual behavior and pairwise interactions between microswimmers in anisotropic liquid. Phys Rev E 91(1):013009
34. Zhou S, Sokolov A, Aranson IS, Lavrentovich OD (2016) Controlling dynamic states of active bacterial suspensions through surface alignment of a nematic liquid crystal environment (submitted)
35. Zhou S, Shiyanovskii SV, Park H-S, Lavrentovich OD (2017) Fine structure of the topological defect cores studied for disclinations in lyotropic chromonic liquid crystals. Nat Comm. Accepted
36. Dombrowski C, Cisneros L, Chatkaew S, Goldstein RE, Kessler JO (2004) Self-concentration and large-scale coherence in bacterial dynamics. Phys Rev Lett 93(9):098103
37. Kim S, Karrila SJ (2005) Microhydrodynamics: principles and selected applications. Dover, New York
38. Giomi L, Bowick MJ, Ma X, Marchetti MC (2013) Defect annihilation and proliferation in active nematics. Phys Rev Lett 110(22):228101
39. Thampi SP, Golestanian R, Yeomans JM (2013) Velocity correlations in an active nematic. Phys Rev Lett 111(11):118101
40. De Luca A et al (2008) Optical nanotomography of anisotropic fluids. Nat Phys 4(11): 869–872
41. Yeh P, Gu C (1999) Optics of liquid crystal displays. Wiley, New York

Chapter 6
Summary

Lyotropic chromonic liquid crystals (LCLCs) represent a novel type of liquid crystals formed by self-assembly of disk-shape molecules in aqueous environment. The underlying physics that governs the anisotropic elastic and viscous properties of such materials is fundamentally different from that of thermotropic LCs, lyotropic LCs formed by rigid rods, and lyotropic polymer LCs (LPLCs) formed by semi-flexible chains with fixed size. In the LCLCs, the aggregates are formed by weak van der Waals force, thus their length and flexibility strongly depend on temperature, concentration, ionic contents, pH of the system and so on. As a result, the macroscopic viscoelastic properties show dramatic dependence when temperature, concentration, ionic content of the solution, or pH changes. LCLCs also provide biocompatible environment so that bacteria remain motile in them. The interaction between self-propelled rod-shape bacteria *Bacillus subtilis* and long-range nematic order of LCLCs gives rise to intriguing phenomena and new design concepts of manipulating active colloids. The results are summarized as follows.

1. We determined experimentally the viscoelastic parameters of LCLCs. In the first experiment, we measured the Frank elastic moduli of Sunset Yellow LCLC by studying the director reorientation in magnetic field. We find that the splay constant K_1 and bend constant K_3 are on the order of 10 pN, comparable to each other and to those of the thermotropic LC 5CB. The twist constant $K_2 \approx 1$ pN is about 10 times smaller. The splay constant K_1 and the elastic ratios $\frac{K_1}{K_3}$, $\frac{K_1}{K_2}$ increase significantly as the concentration of SSY increases or temperature decreases. We explain our findings within a model of semi-flexible SSY aggregates, the length of which changes dramatically when the concentration increases or temperature decreases. K_1, determined by the contour length of aggregates L, thus has the strongest temperature dependence among all three. K_3 is determined by the persistence length λ_p. K_2 is the smallest among all three since twist deformation can happen at imaginary "pseudo-layers" without disturbing the orientation of aggregates on each layer. We also estimated the

© Springer International Publishing AG 2017

S. Zhou, *Lyotropic Chromonic Liquid Crystals*, Springer Theses,
DOI 10.1007/978-3-319-52806-9_6

scission energy $E = (7 - 13)\ k_B T$ and persistence length λ_p on the order of tens of nm, in agreement with estimations obtained by other researchers using different methods. The strong increase of K_1 at increased concentration or decreased temperature matches well with the fact that in the neighboring columnar phase, K_1 diverges.

2. In the next set of experiments, we study the effect of ionic additives on the viscoelastic properties of LCLC. We use the same material, Sunset Yellow and fix its concentration with respect to water, while adding different ionic additives (monovalent salt NaCl, divalent salt $MgSO_4$, pH agent NaOH) into the system at different concentrations. Using the same Frederiks transition technique, we measure the Frank elastic constants of each solution as a function of temperature. We also measure the rotation viscosity γ_1 by director relaxation in the magnetic field. We observe dramatic and versatile changes of the viscoelastic properties induced by the ionic additives. For example, adding monovalent salt NaCl decreases K_3 and K_2, shows little influence on K_1, and increases γ_1, while adding divalent salt $MgSO_4$ increases K_1, K_2 and γ_1 but decreases K_3. Increasing pH by adding NaOH decreases all K's and γ_1. These changes of viscoelastic properties induced by ionic additives are explained through the idea that ion concentration in the solution modulates the interaction between aggregates in different ways, changing two characteristic lengths, namely, the contour and persistence length. For example, a stronger Debye screening at higher salt concentration makes the aggregates longer (because of the increased scission energy) but at the same time more flexible. On the other hand, adding NaOH enhances disassociation of sodium ions, elevating the charge density on SSY aggregates. A stronger electrostatic repulsion of molecules within the aggregate decreases the average aggregation length.
3. Another important LCLC material is disodium cromoglycate, due to its optical transparency at visible wavelengths and biocompatibility. We extend our study of LCLC viscoelasticity to this material using a different technique: dynamic light scattering. We determined all three elastic constants of splay, twist, and bend, and also measured the viscosity coefficients associated with these deformations. Similar to the SSY case, DSCG exhibits significant anisotropy of the elastic constants ($K_1 \approx K_3 \approx 10\ K_2$) and strong temperature and concentration dependence of K_1. We also find that the anisotropy of viscosity coefficients is even larger: η_{bend} of DSCG is comparable to that of 5CB, but can be up to 4 orders of magnitudes smaller than $\eta_{splay} \approx \eta_{twist}$. K_1, η_{splay} and η_{twist} grow exponentially as temperature decreases or concentration increases. We explain our findings of temperature dependence of viscoelasticity with a model of semi-flexible aggregates whose length and flexibility are functions of T and c. The experimental study of DSCG shows that $\eta_{splay} \approx \eta_{twist} \propto L^2$ which correlates well with the model of semi-flexible chains and is consistent with the relationship $K_1 \propto L$. Weak temperature dependence found for other parameters (K_2, K_3 and η_{bend}) also agree with the theory. In addition, we detect unexpected

mode in the dynamic light scattering and we attribute it to the stacking fault of DSCG aggregates.

4. Taking advantage of its biocompatibility, we combined DSCG with motile bacteria *Bacillus subtilis* and created a new active nematic system, the living liquid crystals. In this system, independent of the nematic order, we continuously changed the activity from zero to high values by changing bacterial concentration and oxygen availability. The interaction between bacteria induced flow and the long-range nematic order of DSCG gives rise to a wealth of fascinating phenomena not observed in bacterial suspensions in isotropic fluids. (i) At the very low bacteria concentration, individual bacterium swims along the local director. Motion of 24 nm thick flagella disturbs the local nematic order and is thus visible under polarizing optical microscope. On the other hand, bacteria flow changes the nematic order by triggering nematic-isotropic transition at high enough temperature. (ii) At higher bacteria concentration, bacterial motion collectively creates bend deformation with a characteristic coherent length $\xi = \sqrt{\frac{Kh}{\alpha_0 lcU_0}}$, determined by the balance between the activity of bacteria and elastic energy of the distorted nematic director. (iii) At very high bacteria concentration ($\sim 0.2\%$ by volume), bend deformation becomes unstable; instead, topological defects are constantly created and annihilated. Note that 0.2% is only about 1/10 of the concentration for collective motion in isotropic media. Our work provides a platform where one can further explore the interaction of activity and ordered system, as well as provides design concepts to control and manipulate the dynamic behavior of soft active matter for potential biosensor and biomedical applications.